Development of Glass-based Sealants for the Joining of Oxygen Transport Membranes

Xinfang Li

JÜLICH
Forschungszentrum

Development of Glass-based Sealants for the Joining of Oxygen Transport Membranes

Xinfang Li

Abstract

In this thesis, different glass-based sealants were developed for joining oxygen transport membranes (OTM) to obtain matching the coefficient of thermal expansion (CTE) with membrane and support metals. The crystallization behavior of the $BaO–CaO–SiO_2–B_2O_3$ system glass (H) and $BaO–SrO–SiO_2–B_2O_3$ system glasses (BS) will be discussed. In addition, the glass-forming stability of glass matrices, filler type and amount effect on CTE, chemical compatibility, mechanical strength, shrinking behavior, viscous flow property, joining behavior, thermal cycling and long-term thermal stability were analyzed for various glass-based sealants. The feasibility of the fast joining process was also investigated to economize the energy costs of the heating process. $SrTi_{0.75}Fe_{0.25}O_{3-\delta}$ (STF25) was used as an OTM, and the sealing partners were ferritic steel Aluchrom, pre-oxidized Aluchrom and Crofer22APU.

$BaO–CaO–SiO_2–B_2O_3$ system glass H matrix was first investigated with respect to its glass-forming tendency, crystallization and CTE. The crystalline behavior of glass H as the sealant matrix was investigated and predicted by experimental X-ray diffraction (XRD) analysis and the simulation using the thermodynamic package FactSage. Glass H exhibits a relatively low CTE (9.6×10^{-6} K^{-1}) compared to STF25 and Aluchrom. Nine different filler materials were added to glass H in various amount for improving the CTE of glass-based composite sealants. Dilatometric tests were carried out to observe the influence of filler on thermal expansion. The viscous flow behavior of the composite sealant was investigated by hot stage microscopy (HSM) to determine the optimal joining temperature. The joining behavior of glass-based sealants for different thermal joining processes were analyzed via helium leakage testing, X-ray computed tomography (CT) inspection, scanning electron microscopy (SEM) analysis on cross-sections of the joints. The joints showed low helium leak rates smaller than 10^{-9} mbar·l·s^{-1} and good adherence of the glass sealants to the support metals and STF25. The mechanical shear strengths of sealants were measured by torsion testing on hourglass-shaped samples. A higher shear stress up to 62.2 MPa was found on composite joint which 40 wt.% Ag (HAg40) was added. HAg40 was able to withstand 20 times thermal cycles between room temperature and 800 °C and exhibited good thermal stability at 800 °C for up to 1500 h. These glass H-based sealants are promising candidates for OTMs.

Three new $BaO–SrO–SiO_2–B_2O_3$ (BS) glass sealants with different SrO contents (6-25 mol%) were developed for OTM joining applications. The strontium content was investigated in terms of its effect on the glass-forming tendency, thermal expansion, crystallization, shrinkage behavior, viscous flow, and joining behavior. The CTE value decreases with the increasing SrO content of the BS glasses. The glass with 15 mol% (BS15) SrO produced the best matching CTE (11.9×10^{-6} K^{-1}) with STF25 and Aluchrom. The crystallization behavior of the BS glasses was investigated by XRD. Sinking dilatometric measurements simulated the joining procedure and observed the shrinkage behavior of the BS glasses. The viscous flow behavior of the BS glasses was investigated via HSM. The optimal joining temperature of the BS15 glass was chosen close at half-ball temperature. The sandwiched sample sealed by the BS15 glass achieved good gas-tightness with a low helium leak rate of $< 10^{-9}$ mbar·l·s^{-1}.

Kurzfassung

In dieser Doktorarbeit wurden verschiedene glasbasierte Dichtungsmaterialien zum Fügen von Sauerstofftransportmembranen (OTM) entwickelt, die passende Wärmeausdehnungskoeffizienten (CTE) zu Membran- und Trägermetallen aufweisen. Das Kristallisationsverhalten des für die Dichtung der SOFC als Komposit verwendete $BaO–CaO–SiO_2–B_2O_3$-Matrixglas (H) und drei neu für die Anwendung bei der OTM entwickelte Glaslote des Systems $BaO–SrO–SiO_2–B_2O_3$ (BS) werden diskutiert. Neben der Glasbildungsstabilität von Matrixgläsern wurden Kompositwerkstoffe untersucht, wobei neben Füllstoffart und -menge und deren Einfluss auf den CTE auch die chemische Interaktion zwischen Füllstoffmaterial und Glasmatrix analysiert wurde. Des Weiteren wurde die mechanische Festigkeit, das Sinter- und viskose Fließverhalten von Glaspulverpresslingen, das Füge- und Dichtverhalten von Stahl-Lot-Stahl bzw. Keramik-Lot-Stahl Verbindungen untersucht. Für ausgewählte Lote wurden die thermische Zyklierfähigkeit und Langzeitstabilität getestet. In einer Machbarkeitsstudie wurden schnelle Fügeprozesse untersucht, um Energiekosten bei der Fertigung einzusparen. Als OTM wurde $SrTi_{0.75}Fe_{0.25}O_{3-\delta}$ (STF25) verwendet, als Gehäusepartner dienten der ferritische Stahl Aluchrom (im Anlieferungszustand und voroxidiert) und Crofer22APU.

Das Glas H des $BaO–CaO–SiO_2–B_2O_3$-Systems wurde zuerst auf Glasbildungs- und Kristallisationstendenz und thermische Dehnung analysiert. Das kristalline Verhalten von Glas H als Dichtungsmatrix wurde experimentell mit Röntgenbeugungsanalyse (XRD) untersucht und die Phasenbildung durch thermodynamische Simulation mit der Software FactSage vorhergesagt. Glas H weist im Vergleich zu STF25 und Aluchrom einen relativ niedrigen CTE ($9,6 \times 10^{-6}$ K^{-1}) auf. Daher wurden neuartige Kompositmaterialien mit Glas H als Matrix hergestellt. Neun verschiedene Füllstoffmaterialien wurden Glas H in verschiedenen Mengen hinzugefügt, um eine Verbesserung des CTE der Kompositlote zu erzielen. Das viskose Fließverhalten von Verbundwerkstoffen wurde mittels Erhitzungsmikroskopie untersucht, um die optimale Fügetemperatur zu ermitteln. Das Fügeverhalten der Kompositlote nach verschiedenen thermischen Fügeprozessen wurde mit Hilfe von Helium-Lecktests an Fügeverbindungen, mit Röntgen-Computertomographie (CT) und Rasterelektronenmikroskopie (SEM) an Querschnitten der Fügeverbindungen beobachtet. Die Verbindungen zeigten niedrige Helium-Leckraten von weniger als 10^{-9} mbar·l·s^{-1} und eine gute Haftung der Glasdichtungen an Trägermetallen und Membrankeramik STF25. Mechanische Scherfestigkeiten von Glas-Kompositloten wurden durch Torsionstest an den sanduhrförmigen Proben gemessen. Eine höhere Scherspannung bis zu 62,2 MPa wurde an Verbundwerkstoffen festgestellt, denen 40 Gew.-% Silber zur Glasmatrix H (HAg40) hinzugefügt wurden. HAg40 konnte 20 thermischen Zyklen widerstehen und hat bei 800 °C eine gute thermische Stabilität über einen Zeitraum von 1500 h gezeigt. Dieses Kompositlot auf Basis von Glas H- ist ein vielversprechender Kandidat als Dichtungsmaterial für OTM.

Es wurden drei neue $BaO–SrO–SiO_2–B_2O_3$ (BS)-Glasdichtstoffe mit unterschiedlichen SrO-Gehalten (6-25 Mol-%) entwickelt. Der Gehalt an Strontium wurde hinsichtlich seines Einflusses auf die Glasbildung, der thermischen Dehnung, die Kristallisation, das Schwindungsverhalten, das viskose Fließen und das Fügeverhalten untersucht. Das Glas mit 15 Mol-% (BS15) SrO erzeugte mit STF25 und Aluchrom den am besten passenden CTE von $11,9 \times 10^{-6}$/K. Die optimale Fügetemperatur des BS15-Glases wurde nahe der Halbkugeltemperatur gewählt. Eine Sandwich-Probe, mit BS15-Glas gelötet bei 1075 °C für 5 min, erreichte eine gute Gasdichtigkeit mit einer niedrigen Helium-Leckrate und ist ein weiterer interessanter Kandidat für die Abdichtung von OTM.

Content

1. Motivation and objective

Global warming is one of the greatest challenges faced by humans on the Earth. The NASA climate report [1] (Fig. 1-1) explains that the Earth's surface has been warming since the second industrial revolution and the temperature has risen by 1 °C above pre-industrial levels, as human activities have increased heat-trapping greenhouse gas levels in the Earth's atmosphere. Global warming poses many risks, such as rising sea levels, global climate change, more frequent and intense drought, floods, storms, and heat waves. The greenhouse gases emitted are mainly carbon dioxide (CO_2) from the combustion of fossil fuel and industrial processes. In order to mitigate the effects of climate change and implement the necessary energy transition, the European Commission defined ambitious targets for reducing net greenhouse gas emissions by at least 55% by 2030 [2] compared to 1990 levels. In this context, it is a priority to reduce CO_2 emissions, and the utilization of CO_2 while also improving energy efficiency for the protection of the environment. The entire industrial world will play an important role in such a transformation.
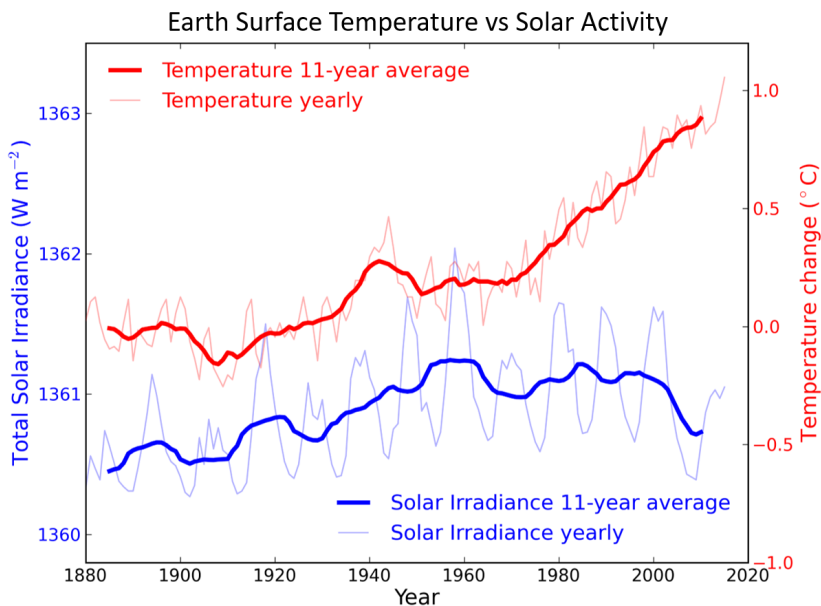
Fig. 1-1. Graph comparing global surface temperature changes (red line) and the sun's energy that has reached Earth (blue line) in watts (units of energy) per square meter since 1880. The lighter/thinner lines show the yearly levels, while the heavier/thicker lines show the 11-year average trends. Eleven-year averages are used to reduce the year-to-year natural noise in the data, making the underlying trends more obvious [1]

The use of oxygen transport membranes (OTMs) has thus emerged as the cost-efficient technologies to alleviate the environmental burden caused by the overall increase in the concentration of CO_2 in the atmosphere [3, 4]. OTMs have exhibited some promising applications [5] at high temperatures of over 700 °C for the reduction of CO_2 emissions and the utilization of CO_2. They can be used to purify oxygen for the more efficient combustion of fuel and capture of CO_2 on the exhaust side. They could also combine the separation process directly with chemical reactions by integrating with catalysts as OTM reactors [6, 7], for example, to produce syngas (CO, H_2) from methane [8] or methane/CO_2 mixture [9], and CO_2 decomposition [10].

In order to attach the membranes to an industrial process, OTM modules with multiple repeating units must be generated. Joining material is therefore needed to assemble membranes and other support components in order to keep the OTM modules gas-tight and perform the separation task [11]. The joining behavior of sealants with ceramic membranes and metal supports must be taken into consideration when building and long-term operating planar OTM modules. The sealing materials need to fulfill some requirements for high temperature OTM application. A hermetically tight and long-term thermal stable joint is necessary to separate gases from different sides of OTM module. The sealants should be able to withstand long-term operation temperatures (700–900 °C). The coefficient of thermal expansion (CTE) of the sealant needs to match with the OTM and the housing parts of the alloy around 12×10^{-6} K^{-1} [12, 13] in order to prevent non-uniform thermal stress distribution. The sealants should exhibit suitable viscous flow properties during the joining process. A key factor for successful joining is chemical stability at high temperatures in oxidizing and reducing atmospheres. Long-term stability and thermal cycling resistance are also necessary for a good sealant during OTM module operation.

At present, reactive air brazing (RAB) and glass-based joining are the most commonly investigated techniques for OTM stack joining. RAB technology can achieve the hermetic sealing of OTMs. The RAB process can be readily performed in air without the need for fluxing and the brazed joint shows good resistance in an oxidizing atmosphere at high temperatures [14]. However, RAB show detrimental reactions with the metal components. In addition, the CTE of Ag-based brazing solder (19.5×10^{-6} K^{-1} [15]) is much larger than that of OTMs and their counterparts. Large thermal stresses thus arise in the brazed joint.

Glass-based sealants are considered to be the most reliable joining method and have been widely used in OTM joining and other applications, such as SiC or solid oxide fuel cells (SOFC) [16-19]. Glass-based sealants used for OTM joining have very significant advantages. The viscosity and wettability of glass itself are conducive to joining performance, achieving a hermetic joint and good adhesion to OTM ceramics and metal substrates. The properties of glass-based sealants can be tailored by adjusting the composition of the glass matrix, filler type and its reinforced amount. Glasses offer heat resistance at operating temperature and chemical stability under oxidizing or reducing working conditions. The cost of glass is lower than the brazing alloys. Glass-based sealants are easy to manufacture and the fabrication and use of joints are very flexible for the application of OTM joining.

Glass "H" based on the BaO–CaO–SiO$_2$–B$_2$O$_3$ system with a small amount of Al$_2$O$_3$, ZnO$_2$, and V$_2$O$_5$ additive was investigated as a sealant matrix for joining OTMs due to its excellent viscosity, chemical compatibility, and joining properties demonstrated in SOFC applications at Forschungszentrum Jülich [20]. The thermal expansion of glass H is lower (9.6 × 10^{-6} K^{-1}) than that of the membrane material STF25 (12 × 10^{-6} K^{-1}) and the support substrate Aluchrom (12.6 × 10^{-6} K^{-1}). Thermal expansion mismatch can lead to thermal stresses, resulting in cracking and delamination of the samples, which in turn causes the module to leak gas. Adding filler materials of a higher CTE to the glass matrix is a feasible strategy for improving the CTE of glass H in order to obtain matching CTEs with membrane and support metals. Moreover, developing a new glass system with a high CTE to replace glass H is also a strategy for overcoming this problem.

The aim of this study is to develop suitable glass-based sealants for the joining application of OTMs. The thermal property and crystalline behavior of BaO–CaO–SiO$_2$–B$_2$O$_3$ system glass H were investigated at first. Nine different fillers (Ag, Ni, Ni-Cr (80-20), CGO, STF25, STF35, Fe30Cr5Al0.5Y, BaSiO$_3$, and Sr$_2$SiO$_4$) were then added to glass matrix H in various amounts to increase the CTEs of the glass-based sealants. Furthermore, new BaO–SrO–SiO$_2$–B$_2$O$_3$ system glass sealants with higher CTE values compared to glass H were fabricated for application in OTMs joining. In addition to the conventional joining process of glass H (850 °C, 10 h), several high-temperature joining processes, thermal cycling and long-term ageing were investigated for the glass-based sealants used for OTM. Experimental results were analyzed in terms of glass forming stability, chemical compatibility, thermal expansion, crystalline behavior, shrinkage and viscous performance with respect to the temperature, gas-tightness, and microstructural joining behavior of glass-based sealants.

2. Background

This section primarily focuses on reviewing the state of art, introducing relevant design concepts and explaining the theoretical background for better understanding of this work. In the first part, the functional principle of oxygen transport membranes and membrane materials are presented together with the stacked OTM module designs. The high temperature joining technologies of brazing and glass sealing are discussed in the next part, followed by a detailed description of glass sealant systems, the possibility of forming a composite by adding filler materials and a theoretical assessment of joining process treatment of glass-based sealants.

2.1 Oxygen transport membranes (OTMs)

2.1.1 Mechanism and application of OTMs

Oxygen transport membranes (OTMs) are mixed ionic–electronic conducting ceramics, which enable oxygen diffusion via oxygen vacancies in the perovskite crystal lattice at high temperatures (700–1000 °C) and permit the separation of oxygen from air with a partial pressure gradient as a driving force [21-23]. OTMs have various applications, for example the separation of pure oxygen from air [24], integration as membrane reactors for carbon capture, and the conversion of natural gas, oil, coal, or biogas into syngas [6] which is an important intermediate product for various chemical processes [8, 25]. Therefore, numerous studies have been devoted to the development of OTMs [3].

Fig. 2-1 shows the schematic of oxygen transport processes through an OTM. Oxygen permeates through the OTM via three main steps [26, 27]: 1) oxygen exchange at the gas–solid interface of the feed side with oxygen partial pressure (P_f); 2) bulk diffusion across grains and grain boundaries; and 3) oxygen exchange on the solid-gas interface of the permeation side with low oxygen partial pressure P_p. The driving force for oxygen exchange and diffusion is the oxygen chemical potential gradient on both sides of the membrane due to the difference in oxygen partial pressure, $P_f > P_p$.

The surface oxygen exchange processes can be written using the Kröger–Vink notations as follows [26, 28]:

For the feed side: $$\frac{1}{2}O_2 + V_O^{\cdot\cdot} \rightarrow O_O^\times + 2h^\cdot \tag{2.1}$$

For the permeation side: $$O_O^\times + 2h^\cdot \rightarrow \frac{1}{2}O_2 + V_O^{\cdot\cdot} \tag{2.2}$$
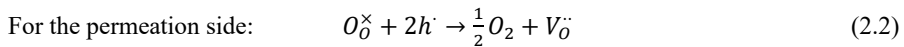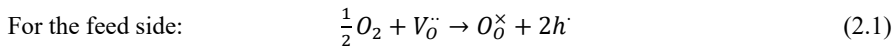
where the notations, $O_O^\times$, $V_O^{\cdot\cdot}$ and $h^\cdot$ represents an oxygen ion occupying an oxygen lattice site, an oxygen vacancy, and an electron hole, respectively. The superscripts $\times$ and $\cdot$ denote an electroneutral state and one positive effective charge, respectively. The holes and oxygen vacancies are considered as the charge carriers.
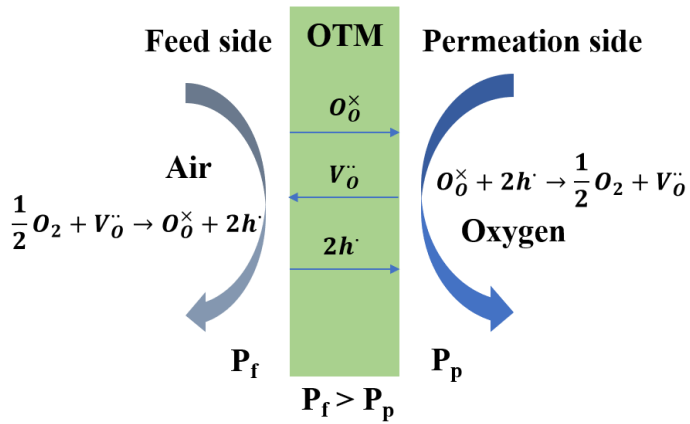
Fig. 2-1. Schematic of oxygen transport processes through an oxygen transport membrane.

The OTM is not only used for the purification of oxygen directly, but can also produce syngas through integration with the catalysts. The OTM reactor is a device that combines membrane separation processes directly with chemical reactions on one or both sides of a membrane for the production of syngas, the reduction of CO_2 emissions and the utilization of CO_2 [6]. OTM reactors have been investigated for different applications. Deibert et al. [6] summarized four different types of OTM reactors, as can be seen in Fig. 2-2. According to the different working principles to produce syngas, membrane reactions can be divided into three categories: partial oxidation, steam reforming, and dry reforming of methane [6, 29]. The main reactants are methane, oxygen, water, and CO_2.
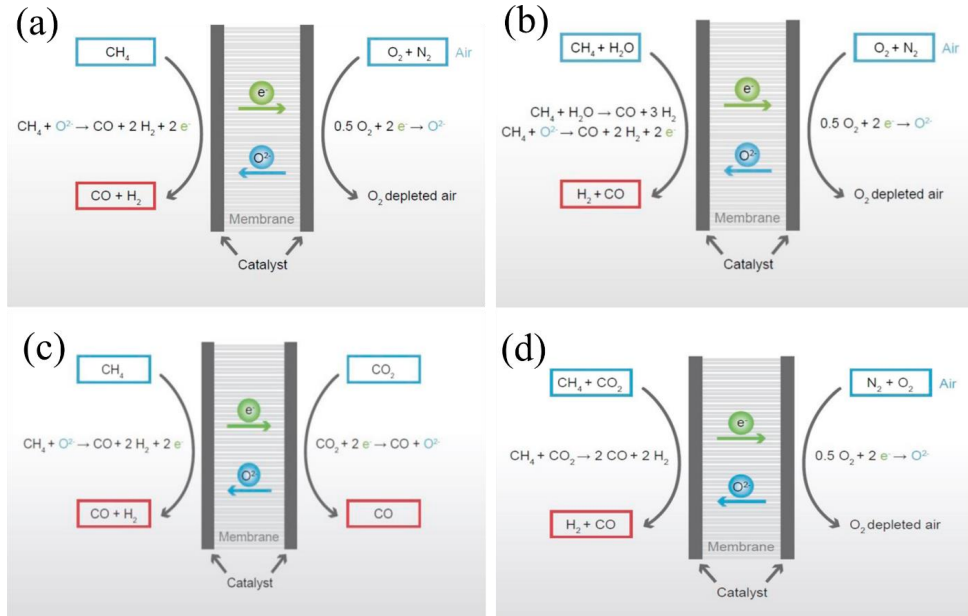
Fig. 2-2. Schematics of the working principles in four oxygen transport membrane reactors: (a) partial oxidation of methane, (b) autothermal reforming of methane, (c) and (d) two possible membrane configurations for the dry reforming of methane [6].

Since the reduction of CO_2 emissions and the utilization of CO_2 are currently important issues in energy and environmental work, OTM reactors are expected to be applied on a larger scale to improve environmental protection by carbon capture. At present, the technology is still limited by membrane materials, catalysts and sealing materials, and research on the topic of membrane reactor design is still in the laboratory stage.

2.1.2 Membrane materials

The most investigated oxygen transport membrane materials are the ABO_3 oxides with a perovskite structure, which offer the highest oxygen permeability [30]. The A-sites are occupied by alkaline-earth metals or the rare-earth elements of the La-series, whereas the B-sites are occupied by transition metals [31], such as $BaBiO_3$, $BaCeO_3$, $SrTiO_3$, $SrCeO_3$, $SrFeO_3$, $LaCrO_3$, $LaCoO_3$, and $LaFeO_3$. Oxygen diffusion or flux in classical perovskites of the pure ABO_3 formula is limited, which could be improved by increasing the number of defects or oxygen vacancies in the perovskite structure [30]. This can be achieved by partial substitution either of the original cation sites (A or B) with other cations (A´ or B´) of different sizes and valences, leading to a variant ABO_3 perovskite crystal structure of the formula $A_xA´_{1-x}B_yB´_{1-y}O_{3-\delta}$, where δ denotes the number of oxygen vacancies [31-33]. Among the various membranes, $Ba_{1-x}Sr_xCo_{1-y}Fe_yO_{3-\delta}$ (BSCF) and $La_{1-x}Sr_xCo_{1-y}Fe_yO_{3-\delta}$ (LSCF) appear to be the most promising materials with the highest reported

oxygen permeation rate [34-37]. Despite its good performance, BSCF has several shortcomings limiting its application [23]. $Ba_{0.5}Sr_{0.5}Co_{1-x}Fe_xO_{3-\delta}$ membranes (x = 0, 0.2, 0.4, 0.6, 0.8, and 1) tend to decay in the measured oxygen permeation flux due to their low thermochemical stability [34, 38]. Liu et al. [39] reported about phase decomposition in $SrTi_{0.75}Fe_{0.125}Co_{0.125}O_{3-\delta}$ (STC12.5F12.5), $SrTi_{0.75}Co_{0.25}O_{3-\delta}$ (STC25), and $SrTi_{0.65}Fe_{0.35}O_{3-\delta}$ (STF35) membranes at temperatures of 600 °C and 900 °C. In contrast, $SrTi_{0.75}Fe_{0.25}O_{3-\delta}$ (STF25) showed good phase stability, with no secondary phases detected after syngas annealing at temperatures of 600 °C and 900 °C [39]. Some studies [12, 40, 41] investigated the structure and functional properties of $SrTi_{1-x}Fe_xO_{3-\delta}$ (x = 0, 0.05, 0.1, 0.15, 0.25, 0.2, 0.3, 0.35, 0.5, 0.6, 0.75, and 1), and found that 25–35% Fe substituting Ti shows good stability and oxygen permeability which can be comparable to that of $La_{0.6}Sr_{0.4}Co_{0.2}Fe_{0.8}O_{3-\delta}$ [37].

2.1.3 Membrane module design

In order to attach the oxygen transport membranes to an industrial process, membranes must be assembled with other gas chamber separation housing materials (counterpart alloys) into stacked modules consisting of multiple repeating units joined hermetically by a sealant. Ferritic stainless steels can be used as a cost-efficient, machinable counterpart material to the OTM. Several configurations have been proposed and developed for OTM modules, in order to optimize the permeation rate of oxygen through the membrane and the conversion efficiency of the catalyst on the membrane surface as well as to lower the fabrication cost of the membrane module [9, 42-44]. Five different design configurations for OTM modules have been reported in the literatures, i.e. tubular design, honeycomb design, hollow fiber design, planar design and plate-and-tube design [23, 45]. Planar OTM is the most common, state-of-the-art membrane configuration, due to the high cost efficiency of easy-fabrication membrane process using tape casting technology. To upscale the technology for the OTM module, the joining behavior of the sealant with a ceramic membrane and metal, chemical, and mechanical compatibility with the support metal must be taken into consideration for the construction and long-term operation of the planar OTM module.

Schulze-Küppers et al. [11] designed a large scale planar OTM module stack using the asymmetric membrane $La_{0.6}Sr_{0.4}Co_{0.2}Fe_{0.8}O_{3-\delta}$ for direct integration in oxy-combustion processes, as illustrated in Fig. 2-3. According to finite element analysis and computational fluid dynamic analysis, the designed OTM stack achieves an O_2 concentration of 27% in the permeate gas and CO_2, O_2 recovery rate up to 86% from the feed gas at a feed pressure of 5 bar and an operation temperature of 850 °C.
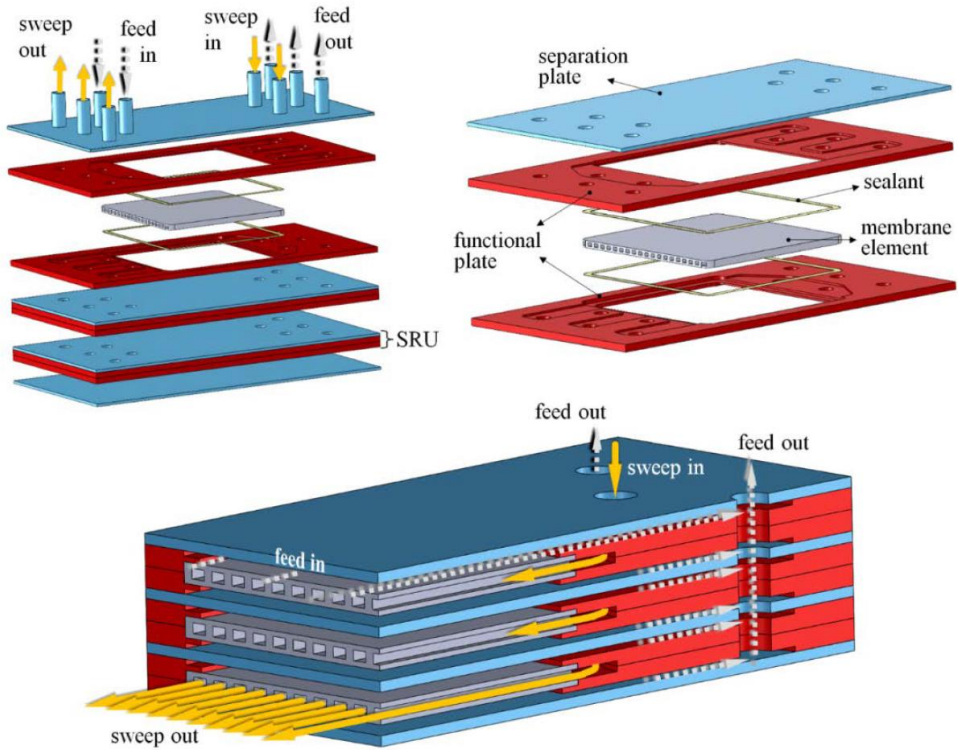
Fig. 2-3. Design concept for the operation of a planar membrane module stack in 4-end mode (top left), single reparation unit (SRU, top right), and quarter section with illustrated flow of deed and sweep gas [11].

Drago et al. [46] fabricated a membrane planar module prototype with $La_{0.6}Sr_{0.4}Co_{0.2}Fe_{0.8}O_{3-\delta}$ (LSCF) for oxygen separation, as seen in Fig. 2-4. The asymmetric membranes acting as separation layers showed a permeation of approx. 3 NmL/min/cm^2 at 900 °C in air/He gradient, with remarkable stability up to 720 h. LSCF membrane components were assembled in the metallic case made of Inconel 625 joined with a Ba-based borosilicate glass (GC2) sealant, resulting in a solid LSCF/GC2/Inconel 625 joint without any failure or detachment among the different materials.
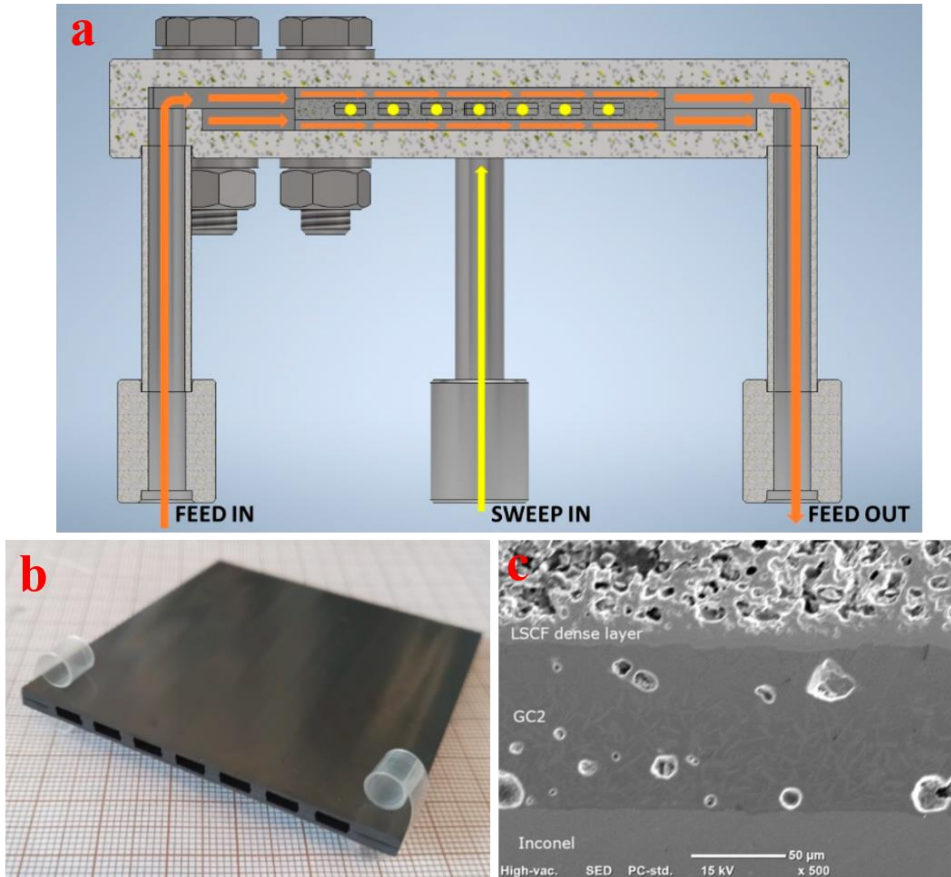
Fig. 2-4. (a) Section of a membrane module prototype, LSCF membrane component assembling in the metallic case with the aid of a Ba-based borosilicate glass (GC2) sealant; (b) final membrane component with dimensions of 60×60 mm; (c) SEM cross section of joint LSCF/GC2 sealant/Inconel [46]

2.2 High-temperature joining methods for OTM

At present, the oxygen transport membrane technology is still at a low readiness level, and one of the main obstacles to realizing the industrial-scale production of OTMs is the lack of low-cost and reliable high temperature joining materials. The operating conditions for OTMs are harsh and complex. Therefore, exploring and developing sealing materials with good compatibility, a suitable thermal expansion coefficient (around $12 \times 10^{-6}\,\mathrm{K}^{-1}$), and excellent joining performance at a low cost plays a very important role in the development of OTM technology.

2.2.1. Sealant requirements for OTM application

In order to attach the membranes to an industrial process, an upscaling of modules with multiple repeating units must be achieved. Joining materials are therefore needed to assemble membranes and other support materials to set up modules that can perform the gas separation task [11, 47]. The sealants should meet the following requirements:

(1) adhesion of the sealing material to OTM components between room temperature and operating temperatures up to 900 °C
(2) ability to provide a gas-tight seal at the OTM operating temperature,
(3) adapted coefficients of thermal expansion (CTE) around $12 \times 10^{-6}\,K^{-1}$ to minimize thermal stresses occurring with the components to be joined
(4) no adverse or harmful reactions between the sealing material(s) and the OTM components at joining temperature or operation temperature
(5) chemical and physical stability of the sealant at temperatures up to 900 °C in oxidizing and reducing atmospheres
(6) long-term operation resistance at temperatures higher than 750 °C and with a suitable tolerance for several thermal cycles

At present, reactive air brazing and glass-based joining are the most commonly investigated techniques for joining OTM module. These two joining technologies are explained in the following sections.

2.2.2 Brazing

Brazing is a technique widely used to join materials by means of an alloy that melts upon heating and wets the surface of the component, creating a bond upon cooling and solidification of the braze alloy. In this technique, the brazing alloy is heated to the melting temperature and then fills the gap between the two materials. Upon cooling, a solid joint is formed. Reactive air brazing (RAB) is a promising alternative technique that has been developed in the last 20 years for joining oxygen transport membranes and steel alloy counterparts at high temperatures [48]. RAB technology is ideal for joining OTMs, as the RAB process is readily performed in air without the need for fluxing, and the brazing joint shows good resistance in an oxidizing atmosphere at high temperatures [14]. The joining procedure is usually carried out at temperatures above 900 °C. Therefore, the joined components are suitable for high-temperature operation. In order to prevent oxidation in air, a noble metal, such as silver or gold, is used as the main component [49-51]. Typical RAB systems investigated include Ag, Ag-CuO, Ag-CuO-TiO$_2$, and Ag-V$_2$O$_5$ among which Ag-CuO is the most commonly investigated RAB braze system for OTM joining [52, 53].

RAB for ceramic OTM-to-metal joints at high temperature have been developed to bond membrane ceramics such as La$_{0.6}$Sr$_{0.4}$Co$_{0.2}$Fe$_{0.8}$O$_{3-\delta}$ (LSCF) [49], BaCo$_{0.4}$Fe$_{0.4}$Zr$_{0.2}$O$_{3-\delta}$ (BCFZ) [54], Ba$_{0.5}$Sr$_{0.5}$Co$_{0.8}$Fe$_{0.2}$O$_{3-\delta}$ (BSCF) [55, 56], Ce$_{0.9}$Gd$_{0.1}$O$_{2-\delta}$ − La$_{0.6}$Sr$_{0.4}$Co$_{0.2}$Fe$_{0.8}$O$_{3-\delta}$ (GDC–LSCF), Ce$_{0.9}$Gd$_{0.1}$O$_{2-\delta}$ − La$_{0.7}$Sr$_{0.3}$MnO$_{3\pm\delta}$ (GDC–LSM) [57], partially stabilized zirconia YSZ [58],

$BaCo_{0.7}Fe_{0.2}Nb_{0.1}O_{3-\delta}$ (BCFNO) [59], $Ce_{0.8}Gd_{0.2}O_{2-\delta} - NdBaCo_2O_{5+\delta}$ (CGO–NBCO) [60], and stainless alloys such as, AISI 314 [55], AISI 310S, Inconel 600 [61], Crofer 22 APU [62], Kanthal APMs, Haynes 214s and EN 1.4841, Fecralloy, X1CrTiLa22, X15CrNiSi25-20 [63], SUS 460 FC [57], Nicrofer® 3220H/Alloy 800 (1.4876) [49].

Kiebach et al [62]. adopted pure Ag brazing with ceramic membrane BSCF (10 %Ba, 10% Sr, 16% Co, 4% Fe, 60 % O) and Crofer 22 APU to overcome the adverse effect of Cu due to its high reactivity with BSCF. Fe oxide and chromia scale were formed during the brazing process at the interface between silver and alloy around 10–15 μm, indicating massive corrosion in this structurally important location. The Cr_2O_3 scale was dissolved in the Ag braze and the Cr reacts with the BSCF membrane tube with the formation of $BaCrO_4$, as seen in Fig. 2-5. The reactions between the braze and the membrane lead to cracks and mechanical instability. Zhang et al. [60] investigated RAB Ag–CuO alloy brazing with a dual-phase oxygen membrane $Ce_{0.8}Gd_{0.2}O_{2-\delta} - NdBaCo_2O_{5+\delta}$ (CGO–NBCO) and found that the wettability between the Ag–CuO solder and the CGO–NBCO oxygen membrane improved due to the interfacial reaction between the Cu oxides in the braze and the surface layers of the CGO–NBCO substrates forming compounds of Ba–Cu–O, Co–Cu–O and Nd–Ce–Cu–O oxides.
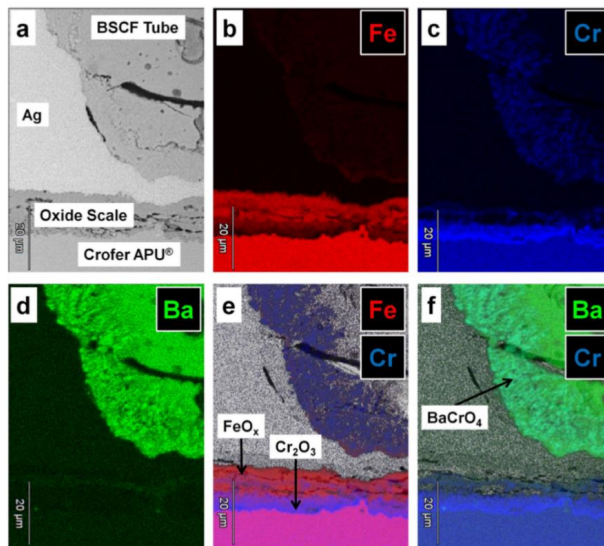
Fig. 2-5. SEM/EDX maps of BSCF/Ag/Crofer 22 APU assembly. (a) overview image; (b) Fe distribution; (c) Cr distribution; (d) Ba distribution; (e) overlapped EDX maps of Fe and Cr; (f) overlapped EDX maps of Ba and Cr [62]

Muhamad et al. [61] reported that the interfacial joining microstructure of brazing material Ag–10 wt.% CuO was evaluated for the RAB with dense $Ce_{0.9}Gd_{0.1}O_{2-\delta} - La_{0.7}Sr_{0.3}MnO_{3\pm\delta}$ (GDC–LSM) OTM ceramics and four types of metal alloy (Crofer 22 APU, Inconel 600, Fecralloy and

AISI 310S). All the four types of metal alloy/GDC–LSM joints showed tight joining at the filler/GDC–LSM interface without the formation of a reaction zone. However, an oxide layer around 12 ± 3 µm was formed at the brazing solder/metal alloy interface for all samples due to the oxidation of the metal alloy surface.

Shiru et al. [64] investigated the effect of the CuO composition in the Ag–CuO brazing system on joining behaviors between Ni/YSZ and the SS430 steel interconnect. The solder with 6 mol% CuO received the lowest gas leakage as low as 0.001 sccm cm^{-1}. When comparing SEM images of pure Ag and 6 mol% CuO (Fig. 2-6), it can be seen that pure Ag wets poorly on the SS430 interconnect surface; 6 mol% CuO braze forms a reaction zone over 10 µm, upon which Ag wets well, indicating that the hermeticity is improved significantly.
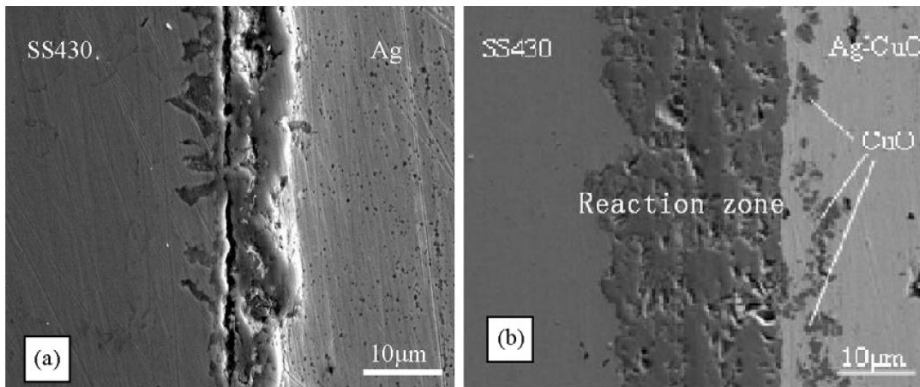
Fig. 2-6. SEM images of cross-sections of the SS430/Ag–CuO sealing interface: brazing in air with (a) pure Ag and (b) 6 mol% CuO [64]

Although RAB technology can achieve OTM hermetic sealing, three issues need to be considered. (1) When using Ag–CuO as a brazing material, CuO will react with the metal components in the stainless steel, thus forming a thick composite oxide layer. This interfacial reaction zone is highly brittle and a weak component in the joint. (2) Ag-based brazing will creep during high-temperature operation, which will reduce the overall strength of the joint. (3) The connection method using RAB is a rigid bond. The thermal expansion of Ag-based solder (19.5×10^{-6} K^{-1} [15]) is much larger than the CTEs of OTMs and counterpart alloys. As a consequence, large residual stresses arise in the brazing joint, leaving undetected problems for the stable, long-term operation or thermal cycling of the component.

2.2.3 Glass-based sealants joining

Glass-based sealants include the pure glass sealant and the filler-reinforced glass sealant, such as glass-ceramic and glass-metal. The glass-based sealant joining process is similar to the brazing method in some aspects. The joining processes take place by wetting the membrane ceramic and

counterpart alloy with the joining materials and diffusion processes occur at high temperatures, which means that glass-based joining and brazing both involve rigid bonding. In addition, their joining temperatures are lower than the melting point of the components to be joined. However, there is a crucial difference in their high-temperature behavior. The brazing alloy melts at brazing temperature to wet the components. While glass does not have a fixed melting point. The wetting behavior of glass-based sealants is achieved by the glass softening and viscous flow at temperatures above the glass transformation point (T_g). The viscosity of glass-based sealant is mainly influenced by the chemical composition of the glass, for the composite sealants also by the type and amount of filler used for reinforcement.

Glass is an inorganic, highly viscous liquid with an amorphous structure, which has been fast-cooled to a rigid condition without crystallizing. Compared to the metal periodic structure with a crystalline structure, glass exhibits a random and disordered network (also called amorphous structure) connected by [SiO_4] tetrahedron units, as seen in Fig. 2-7 [65].
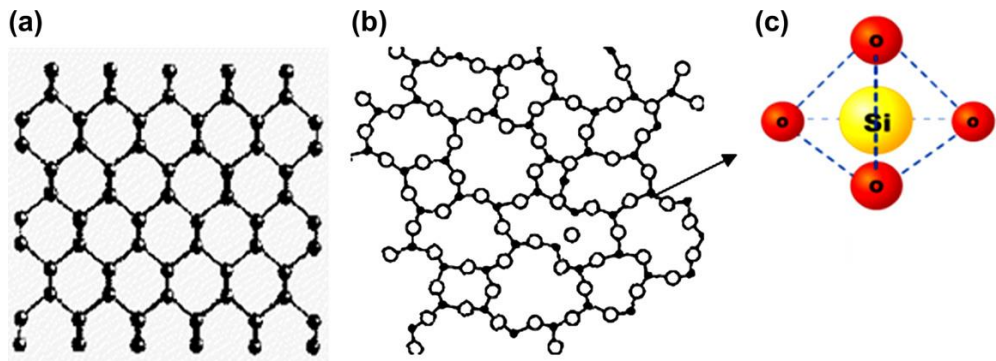
Fig. 2-7. Crystalline structures (a), amorphous randomized structures (b), and the molecular structure of silica-based glass (c) [65]

Glass viscosity is an important parameter for glass application processes, not only in terms of the joining process, but also for forming techniques such as blowing and enameling. Therefore, it is crucial to know the relationship between glass viscosity and temperature. For joining with a glass sealant, the viscosity of the material plays a major role in successful joining and operation. The joining temperature is commonly chosen to be higher than the operating temperature (around 800 °C) [66] for applications such as OTM and SOFC. At joining temperature, the viscosity of the glass sealant should be low enough to flow and fill the joining gap, enabling to wet the components to be joined. During long-term operation, the viscosity of the glass sealant should not be too low that it causes sealant to flow out of the joint gap, as the joint needs to maintain its gas-tightness and exhibit sufficient strength during operation. Fig. 2-8 shows the schematic cross sections of the joints being joined at different viscosities [67]. At sealing temperature, glass should not have too high a viscosity in order to prevent a seal that is too thick, and it should not have too low a viscosity to avoid bead drop [68].
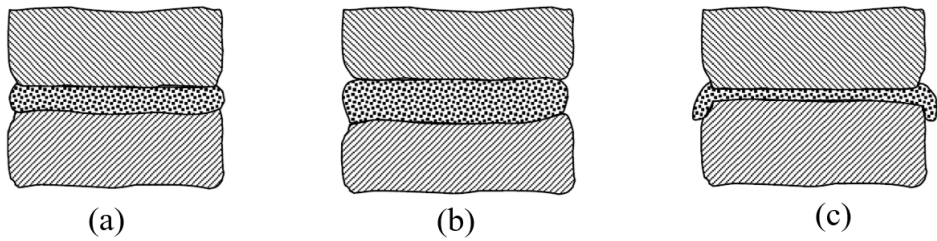
Fig. 2-8. Schematic illustrations of cross sections of joining geometry: (a) ideal joint, (b) too high viscosity (thick joining layer), (c) too low joining viscosity (thin joining layer and bead drop) [67]

Viscosity is directly linked to the chemical composition of a glass. Fig. 2-9 exhibits the relationship of viscosity versus temperature for fused silica and three silica glasses [69]. The viscosity of a glass has an exponential dependence on temperature. The specific standard viscous points [65, 70], listed in Table 2-1, are associated with the viscous flow of glass and are important for the fabrication, processing, and joining of glasses. At the same viscosity value, the required temperatures are different for various glasses. This means that the viscous property can be tailored by glass composition. For example, the addition of boron can decrease glass viscosity to some extent. The temperature range between the working point and the softening point is defined as the working range, where viscosity η is $10^{6.6}$–10^3 Pa·s. Most glass-forming operations are performed within the working range based on experience, which also provides a reference for joining glass and high-temperature operation. An appropriate joining viscosity of the glass sealant is important to achieve a successful joint. Eichler et al. reported that a glass viscosity of about 10^5 Pa·s at working range is sufficient for good joinability [71]. Greven et al. found that for glass H at 850 °C, the appropriate viscosity of sealants for the joining process should be lower than 10^6 Pa·s [66]. Reddy et al. investigated SrO-containing glasses and found that the suitable viscosity is ~10^6 dPa·s (=10^5 Pa·s) at 900 °C for joining SOFC metallic/ceramic components by glass/glass-ceramic sealing upon stack hermitization [72].

Various methods are used for measuring glass viscosity at different temperatures, such as hot stage microscopy [73], high temperature rotational viscometer [74], beam bending viscometry, parallel-plate viscometer [75], and glass fibre elongation viscometer [76]. Viscosity is a measure of the resistance of a liquid to shear deformation over time. η is the coefficient of viscosity, which is the inverse of fluidity [70]. The unit of viscosity is Pa·s in the international system of units (SI), where the shear stress is written in units of Pa. Another common unit for viscosity is Poise (P), which is obtained when shear stress is written in terms of dyn/cm^2. Poise is the original unit for viscosity and is still extensively applied in the glass industry. The conversion between the two units is simple, 1 Pa·s = 10 P.
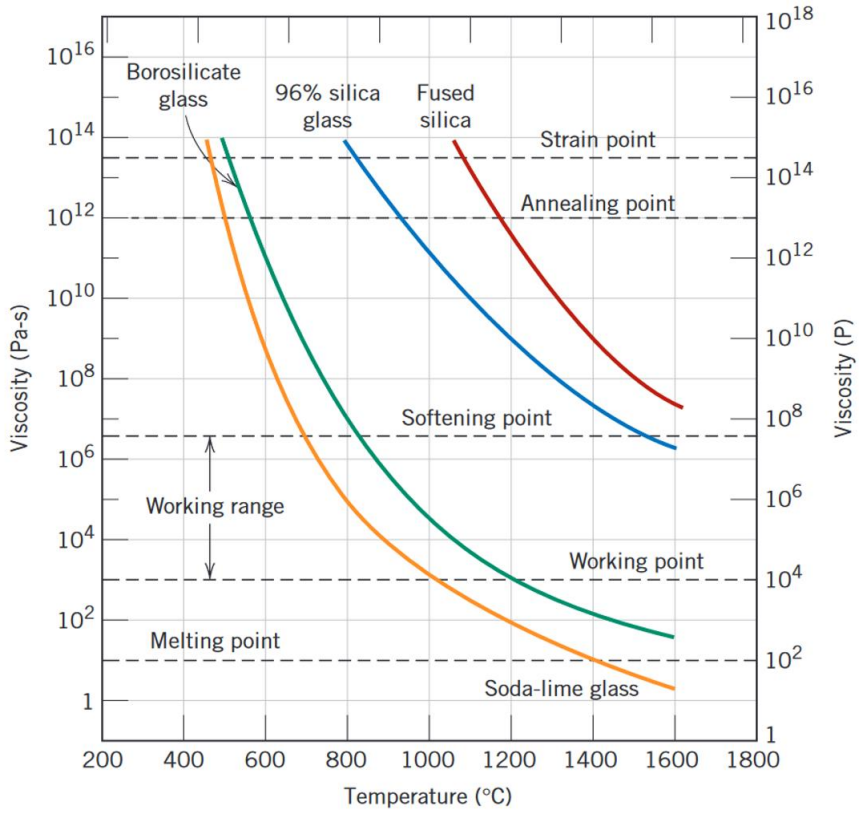
Fig. 2-9. The relationship of viscosity versus temperature for fused silica and three silica glasses [69]

Table 2-1. The standard points of glass [65].

Standard point name	Viscosity (η, Pa·s)	Temperature descriptions
Stain point	$10^{13.6}$	Internal stresses are relieved in hours
Annealing point	10^{13}	Internal stresses are relieved in minutes
Glass transition temperature	10^{11}-$10^{12.3}$	Temperature range in which glass transitions from super liquid rigid state to a more ductile state and with changing glass properties
Softening temperature	$10^{6.6}$	The viscosity is sufficiently low for glass to slump under its own weight. Glass is stiff close to below this temperature, but a little effort is required for yield and flow
Working point	10^{3}	The viscosity is sufficiently low for forming glass. Casting processes are possible
Melting point	10	At this point, the glass becomes fluid enough to be considered a liquid

1 Pa·s (SI) = 10 P (P: poise, viscosity unit).

Glass-based sealants used for OTM joining have very significant advantages:

(1) the viscosity and wettability of the glass itself are conducive to joining performance achieving a hermetic joint and good adhesion to ceramic and metal substrates.
(2) The properties of glass-based sealants, such as the coefficient of thermal expansion, viscosity, mechanical strength, glass transition point and softening point, can be tailored by adjusting the composition of glass matrix, filler type, and amount.
(3) Glass exhibits heat resistance at operating temperature and chemical stability under oxidizing or reducing conditions.
(4) The glassy phase can be minimized by thermal treatment for crystallization or the introduction of filler materials.
(5) The cost of glass is lower compared to brazing alloys and glass-based sealants are easy to manufacture. The application and use of joining materials are very flexible when assembling an OTM joint.

Due to these advantages, the glass-based sealing technique has been most frequently used for laboratory studies of ceramic oxygen transport membranes.

2.2.3.1 State-of-the-art glass-based sealants

Different glass sealant systems have been investigated for high-temperature applications. Alkaline-earth-containing (Ba, Sr, Ca, Mg) glass sealants exhibit suitable viscous flow behavior at joining temperature and during joining operation, with tunable CTEs reaching 12×10^{-6} K^{-1} to match with the components to be joined, and a self-healing feature, all of which makes it a more promising candidate for joining OTMs compared to alkali-containing glass sealants [77, 78].

During OTM joining and operation, the glass phase can be crystalized and converted into glass-ceramic or complete ceramic phase. Crystallization with a high CTE phase formed from the glass sealant can be beneficial for narrowing the CTE gap between the glass sealant and the OTM components. Table 2-2 provides a list of thermal expansion coefficients of some alkaline-earth silicate phases. The CTE increases with the increasing radii of the alkaline earth cation ($Mg^{2+}<Ca^{2+}<Sr^{2+}<Ba^{2+}$). Thermal expansion is mainly controlled by thermal vibrations as a consequence of increasing temperature, which is associated with cation radii and the crystal structure.

Table 2-2. Thermal expansion coefficients of alkaline earth silicate phases [68, 79-82]

Phase	CTE (10^{-6} K^{-1})	Phase	CTE (10^{-6} K^{-1})
$BaSiO_3$	16.9	Sr_2SiO_4	12.5
$BaSi_2O_5$	12.9	$CaSiO_3$	11.2
Ba_2SiO_4	15.6	Ca_2SiO_4	10.8
$Ba_2Si_3O_8$	13.2	Ca_3SiO_7	11.9
$Ba_5Si_8O_{21}$	14.5	$MgSiO_3$	11.0
$SrSiO_3$	11.2	Mg_2SiO_4	9.4

Glass-ceramic materials within the $BaO–Al_2O_3–SiO_2$ (BAS) system with various CoO, CaO and B_2O_3 additives and ratios were studied as potential OTM sealants [83]. The B_2O_3-rich glass "BABS" (25 wt.% BaO, 10 wt.% Al_2O_3, 30 wt.% B_2O_3, 35 wt.% SiO_2) shows good sealing capability when being joined with the BSCF membrane at 950 °C. Although the BABS glass obtained the maximum CTE value of around 6.15×10^{-6} K^{-1} in other glass-ceramics, the expansion of the sealant is much lower than the CTE of the BSCF membrane (16.2×10^{-6} K^{-1}) [84]. Moreover, a disadvantage of B_2O_3-containing glasses is that they have been reported to be significantly volatile [85, 86]. It can be assumed that the addition of small B^{3+} ions to silica glass causes the cleavage of some of the oxygen bridges between Si^{4+} ions, which in turn causes glass structure to become weakened. Singh et al. [87] suggest that the addition of B_2O_3 should be in the range 5–15 mol%.

Vivet et al. [88] investigated and compared the effects of the sealing materials of Duran-based glass and gold ring joining with $La_{0.8}Sr_{0.2}Fe_{0.7}Ga_{0.3}O_{3-\delta}$ perovskite membranes and alumina on oxygen semi-permeation measurements. Duran glass is based on the $SiO_2-B_2O_3-Na_2O-Al_2O_3$ system. The setup of the oxygen semi-permeation measurement device is shown in Fig. 2-10. Contaminated surface zones appear when the membrane setup joined by a glass sealant is exposed to an oxygen partial pressure gradient, which assumes that boron and silicon originating from the alkali glass can easily become volatilize under reducing and oxidizing conditions. Gold is the best sealing material, as it does not cause the surface of the membrane to become contaminated. Hatcher et al. [89] reported that the viscosity of the borosilicate glass sealant ($50SiO_2\cdot25B_2O_3\cdot25Na_2O$, mol%) at a joining temperature of 700 °C (also flow point) is around $\log \eta = 3.4$ (dPa·s). This alkaline glass composition turned out to be not suitable for OTM sealing due to the low viscosity of the glass sealant at typical operating temperatures of 800 °C, causing the glass sealant to flow out of the joint gap.
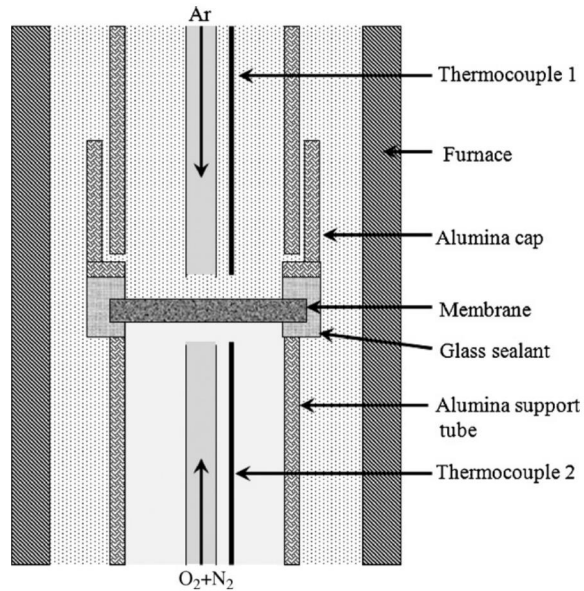
Fig. 2-10. Schematic diagram of the oxygen permeation flux measurements device [88]

Both OTMs and SOFCs use functional perovskite structural ceramics and the problems they face during the joining process are roughly similar. The research and development of stacked OTM modules is still in its infancy [11], while SOFC development has made a lot of progress in the past 30 years [77, 90]. We can therefore learn from SOFC sealing glasses in the development of OTM-joining glass-based sealants.

Kerstan et al. [91] investigated the effect of different BaO/ZnO ratios and thermal treatments on BaO/ZnO/SiO$_2$ system glasses. The CTEs of the crystallized samples are larger than those of the corresponding glasses. The CTEs of the glasses are in a range of 7.2–9.1 × 10^{-6} K^{-1} and increase with increasing BaO concentration. The thermal expansion coefficients of the crystallized sample are in a range of 12–14 × 10^{-6} K^{-1}. In BaO-rich glasses, BaSi$_2$O$_5$ and BaZn$_2$Si$_2$O$_7$ with high CTEs predominantly crystallize. In contrast, the glasses with lower BaO concentrations tend to form undesired cristobalite.

Pablos-Marstin et al. analyzed the BaO/SrO–MgO/ZnO–B$_2$O$_3$–SiO$_2$ system. These glasses have thermal expansion coefficients between 8.5 and 9.8 × 10^{-6} K^{-1}. In particular, the 10B(Sr) composition shows the better stability of the joints, with the formation of a continuous, clean interface with no cracks or gaps. After 50 thermal cycles of the Crofer 22 H/10B(Sr)/8YSZ joints, the interfaces exhibit excellent adhesion, with no cracks or significant diffusion of elements between the seal and the steel or the electrolyte [92], as seen in Fig. 2-11.
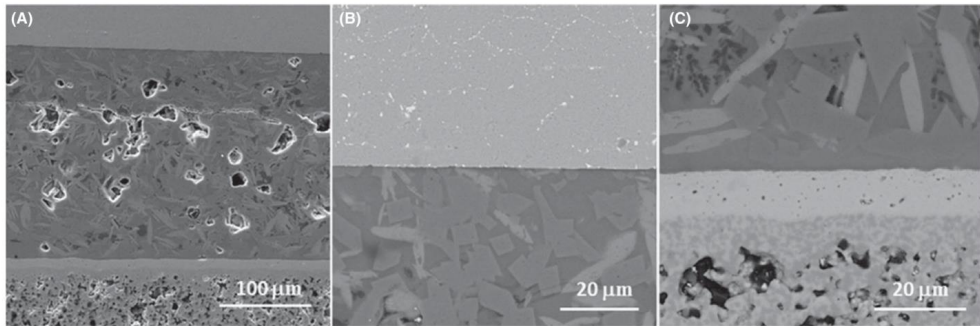
Fig. 2-11. Joint of Crofer 22 H/glass-ceramic/8YSZ sealed by10B(Sr) composition sealant at 850 °C for 10 h and thermally cycled (50 cycles). (A) General view. (B) Interface steel/sealant. (C) Interface sealant/8YSZ [92]

The thermal expansion value of the glass-ceramic sealant depends on the glass network stability and crystalline phases formed during joining and operation. The incorporation of oxide modifiers creates network discontinuity points, leading to a reduction in network cohesion and causing the glass network stability to be affected by temperature. The cohesion of the glass network is influenced by the intensity of the bonds between oxygen and cation modifiers, which is directly linked to the field intensities of the cations. When the field intensity declines, it diminishes the intensity of the bonds between oxygen and cations, leading to a less stable of the glass network and a higher CTE of the glass. The field intensity decreases according to Zn^{2+}> Mg^{2+}> Ca^{2+}> Sr^{2+}> Ba^{2+} [92].

At Forschungszentrum Jülich, glass sealants of the BaO–CaO–Al$_2$O$_3$–SiO$_2$–B$_2$O$_3$ system (named glass "H") with small amounts of ZnO$_2$ and V$_2$O$_5$ additive have been used for solid oxide fuel cell

(SOFC) stack assembly over the last 20 years. The thermal expansion of glass H has been measured at around 9.6×10^{-6} K^{-1}. The CTE of the aged glass H is 8.1×10^{-6} K^{-1} [93]. Brendt et al. [94] investigated the crystallization behavior of glass H after heating at 850 °C for different periods of time from 1 hour to 100 hours. $Ba_2Si_3O_8$ precipitated from glass H as the first phase occurring after a short dwell time of 1 h at 850 °C. In addition, small amounts of Hexacelsian are detected by means of HT-XRD measurements. Celsian and Walstromite are formed in glass H after 5 h and 10 h. After 100 h, more phases were precipitated, barium vanadate, barium calcium borosilicate, calcium zinc silicate and Itsiite. $BaAl_2Si_2O_8$ has two common phases: a monoclinic Celsian low temperature phase with a CTE of around 3×10^{-6} K^{-1} [95] and a Hexacelsian high-temperature phase with a CTE of 7.5×10^{-6} K^{-1} [82]. Some studies [77, 96, 97] have also demonstrated that $BaAl_2Si_2O_8$ phases easily crystallize in a barium–calcium aluminosilicate glass system during the heating process. None of the barium feldspar phases are able to reach CTE values higher than glass H. The low CTE phase formed in glass H during crystallization is the reason that the aged sample of glass H had a declined CTE.

Glass H has a lower CTE compared to components (12×10^{-6} K^{-1}) such as SOFC and OTM. Thermal expansion mismatch can lead to thermal stresses and cracking or delamination of the samples and causes the module to leak gas. Adding filler materials of a higher thermal expansion coefficient to the glass matrix is a feasible strategy for improving the CTE of glass H in order to obtain matching thermal expansion coefficients with membrane and support metals. Gross-Barsnick et al. [20] added 20 wt.% of YSZ powder, 13 wt.% modified YSZ fibres or 20 wt.% silver powder to glass H and studied the sealants joined with Crofer 22 APU for SOFC application. The glass composite sealant with 20 wt.% Ag particles obtained a decent CTE value of around 11.5×10^{-6} K^{-1} [93]. And glass H + 20 wt.% Ag exhibited the highest tensile strength and good joining properties at 850 °C for 10 h. Greven et al. [93] used 10-20 wt.% Ni, Ni-Cr, and CGO ($Ce_{0.8}Gd_{0.2}O_2$), respectively, as reinforcements for glass H to improve the thermal expansion and mechanical properties of the sealant. The CTE of the composite sealants improved with an increasing the filler amount. The composite prepared by a combination of glass matrix and 20 wt.% Ni powder received the highest CTE around 10.8×10^{-6} K^{-1} as sintered and 9.8×10^{-6} K^{-1} as aged. Glass composites with 20 wt.% Ni and 20 wt.% Ag exhibit the best shear strength when joined with Crofer 22 APU.

Blum et al. [98] reported on the long-term operation of solid oxide fuel cells sealed by a glass H + YSZ powder-reinforced glass ceramic sealant. The SOFC stack sealed by glass ceramic sealant can withstand operation at 700 °C for up to 36,000 h and operate steadily at 800 °C for 15,144 h, as seen in the cross sections of the stacks in Fig. 2-12. A thin reaction scale of less than 1 mm formed between the steel surface and the glass sealant. No evident degradation of the glass sealant or influence on the stack operation time was observed.
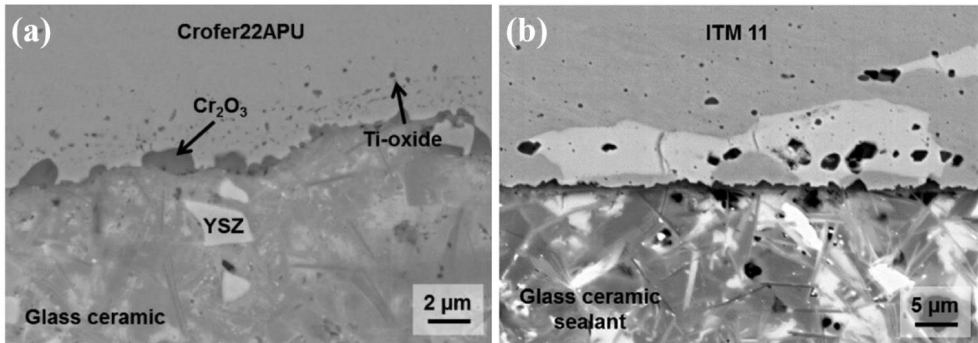
Fig. 2-12. SEM images of cross sections: (a) the F1004-21 stack after 36,000 h of steady operation at 700 °C: interface of glass sealant to Crofer 22 APU in the middle of a joint, (b) the F1002-132 stacks operated at 800 °C after 15,144 h of steady operation [98]

Recently, a self-healing feature of some glass systems has been the subject of increased attention, as they have the ability to heal cracks or defects in material at high temperatures [99]. Gross-Barsnick et al. [100] demonstrated the possibility of repairing leaking glass-ceramic composite seals prepared on the basis of a composite H-F reinforced with yttrium-stabilized zirconia fibers (YSZ) in the glass matrix of the BaO–CaO–SiO$_2$ (glass H) system. The well-joined samples at 850 °C for 100 h were then forcibly broken and repaired by joining at different temperatures varying between the onset and peak temperatures of the melting of the glass ceramic ascertained using differential scanning calorimetry (DSC). The optimal thermal treatment parameters with respect to gas-tightness and porosity were found after repair joining at 930 °C for 10 h. Peng et al. [101] reported that glass sealants with a composition (mol%) of 38.3% SiO$_2$, 27.4% B$_2$O$_3$, 31.3% BaO, 0.6% La$_2$O$_3$, 1.6% ZrO$_2$, and 0.8% Y$_2$O$_3$ exhibited a "self-healing" behavior. The cracks in the bulk of the glass and at the glass/SS410 interface can heal at operating temperature (700 °C) as long as the annealing time is long enough. Zhang et al. [102] observed that borate-containing crystalline species formed from the sealing glass exhibited excellent self-healing property at the operational temperatures of SOFCs, as shown in Fig. 2-13. Singh [99] reported that the stability of the glass seals with self-healing feature under different testing conditions was demonstrated by leak-tight responses even after as many as 300 thermal cycles between room temperature and 800 °C. In addition to maintaining stability, the glass seals retained their ability to self-heal even after very long exposure times of more than 3000 h at higher temperatures.
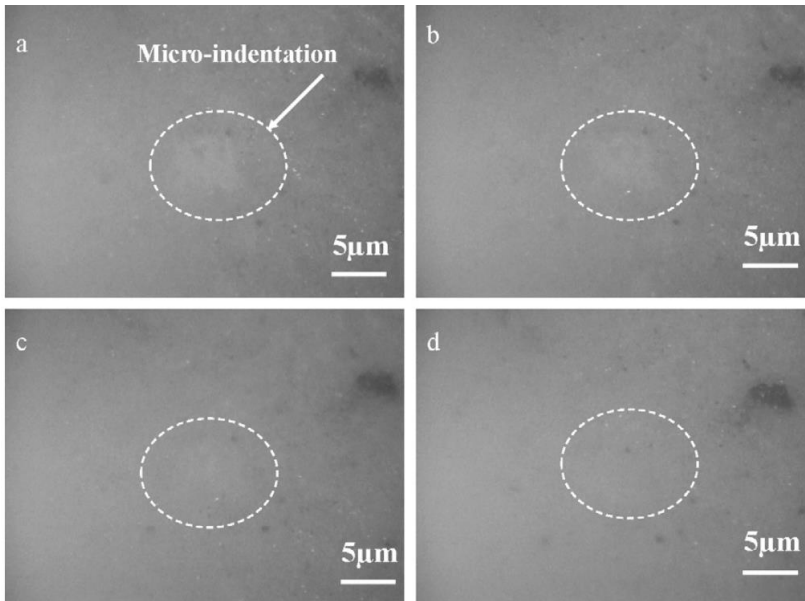
Fig. 2-13. In situ optical images of the calcium borate glass after crystallization at 850 °C in air for one week: in situ observation at (a) room temperature, (b) 700 °C, (c) 800 °C, and (d) 840 °C [102]

Laser technology has been investigated as a possible means of improving the glass joining process, and the possibility of its use on SOFCs has been explored [92, 103-105]. Compared with the above-mentioned furnace joining process, the laser technique offers some advantages, such as the application of precise and focused energy (without the need of heating the entire system) due to the high-power density of the laser; a huge reduction in the time required for the joining process–from hours to minutes [105]; and the avoidance of glass crystallization due to the rapid joining process. Faidel from Forschungszentrum Jülich performed a fundamental investigation into the laser joining of the glass sealant [103, 104, 106, 107]. The laser joining process was optimized by investigating different laser types (CO_2 laser, diode laser, Nd:YAG laser), laser power and processing speed. Rodríguez-López et al. [105] studied the laser cladding of glass-ceramic sealants on Crofer 22 APU. The good adhesion of the GC/Crofer 22 APU joints was observed after laser joining, as seen in Fig. 2-14.

Fig. 2-14. (a) Samples obtained by laser cladding and (b) detail of the thickness [105]

However, there are also a number of disadvantages associated with laser joining for glass sealants compared to the furnace process:

(1) Bubbles and cracks are easily formed during the joining process and laser joining is easy to cause over burning.

(2) Laser welding is more suitable for single-layer surface welding, especially as the joining glass bead is uneven and not flat. It is not suitable for complex multi-layer internal joining. It requires a special moving device, which increases the difficulty of feasibility. In the case of vertical welding, the glass liquid can easily flow out, causing severe welding failures.

(3) Local heating using a laser beam can cause the concentration of local thermal stress, which means there is a huge thermal stress difference between the heated part and non-heated part. This can cause a distortion of the alloy sheets and the cracking of the glass sealant and OTM ceramic due to rapid heating and cooling. There is also the lack of a mechanism to reduce thermal stresses.

(4) The absorption of laser light on the different materials is different. For example, steel exhibits a poor absorption when using a CO_2 laser and mostly obtains energy mostly from the laser by heat transference, while radiation is almost completely absorbed by the glass, causing a poor adhesion [103]. The Nd:YAG laser can heat up the alloy, but subsequently leads to oxidation problems.

(5) The reflection of laser and heat radiation could cause damage to the operator's eyes and skin.

(6) The cost of the laser and its associated systems (accurate temperature pyrometer, auxiliary moving devices, monitoring equipment) is high and the one-time investment is large.

Furnace joining does not involve the above-listed problems and can improve the efficiency of the joining process by pre-assembling multi-layer stacks with green sealant foils produced by using screen printing, tape casting, or syringe dispensing as application methods.

The softening temperature of the glass sealant is typically above the operation temperature of the OTM and SOFC. When heated, it undergoes a viscous flow, and a rigid sealed connection is formed after cooling. There are four aspects that need to be considered in the selection of glass-based sealants:

(1) The operating temperature of the membrane stack should preferably be higher than the T_g of the glass joining material, ensuring that the stress inside the glass can be released through plastic deformation during operation.

(2) Matching the sealant CTE to the OTM components minimizes thermal stress. The glass sealant has a high brittle feature, and if there is thermal stress caused by a CTE mismatch between the sealing material and the OTM components, then it will lay hidden dangers for the long-term stable operation of the OTM.

(3) The reaction between the glass and the OTM components should be minimized. For example, in the process of sealing and subsequent operation, the glass sealant with alkaline-earth ions of more than 40 mol% easily reacts with the metal material to produce a reaction product such as $BaCrO_4$ with a large CTE (23.6×10^{-6} K^{-1}) [108], which is harmful to the performance of the joint.

(4) In addition to interfacial reactions leading to inappropriate phase formation, a similar problem can occur for glass sealant crystallization. The formation of harmful phases, such as low CTE phase $BaAl_2Si_2O_8$ should be avoided.

(5) The oxidation of metal filler or severe interaction between the glass matrix and the filler material should be avoided.

3. Experimental

Oxygen transport membrane STF25 was used in this study. STF25 wafers with a diameter of 16 mm were fabricated by Institute of Energy and Climate Research – Materials Synthesis and Processing (Forschungszentrum Jülich GmbH, IEK-1). The STF25 membranes were pressed and sintered at 1400 °C for 5 h. Three different metal counterparts were used in this study: VDM® Aluchrom Y Hf (1.4767), pre-oxidized Aluchrom (1350 °C, 5 h) and VDM® Crofer22APU. Aluchrom and Crofer22APU were purchased from VDM Metals GmbH. The chemical compositions of Aluchrom and Crofer22APU are shown in Table 3-1.

Table 3-1. Chemical composition of Aluchrom and Crofer22APU

	Composition wt.%			
	Fe	Cr	Al	Additions
Aluchrom	72.8	20.5	6.0	C, Ni, Mn, Si, Zn, Y, Hf, N
Crofer22APU	76.4	22.0	0.3	C, Ti, Mn, Si, Cu, P, La, S

3.1 Glass powder preparation

3.1.1 Ba-Ca glass H

Glass "H" based on the $BaO–CaO–SiO_2–B_2O_3$ system was used as sealant matrix for joining OTM, because of its excellent viscosity, chemical compatibility, and joining properties demonstrated in SOFC applications from Central Institute of Engineering and Technology (ZEA–1) of Jülich Forschungszentrum [20]. Gross-Barsnick et al. [109] developed this glass and it was produced by Heraeus R&D (Germany) now. The glass frits were ground into a median particle size of 12 μm powder checked by Low angle laser scattering method (LA-950). Inductively coupled plasma emission spectroscopy (ICP-OES, ICAP™ 7600) was employed for analyzing the chemical composition of glass H powder. Two parallel digestions of approx. 50 mg per glass sample were carried out in an Au crucible with 500 mg sodium hydroxide at approx. 600 °C for 30 min. The melt was dissolved in water and after the transfer 25 mL 5% HCl was added and a total volume of 50 mL. The digestion solutions were semi-quantitatively analyzed for 26 elements (Al, B, Ba, Ca, Co, Cr, Cu, Fe, Hf, K, La, Li, Mg, Mn, Mo, Ni, P, S, Si, Sr, Ti, V, Y, Zn and Zr). All determinable and desired elements have been quantified and are analyzed. The chemical composition result of main components of glass H is shown in Table 3-2.

Table 3-2. Glass H chemical composition analyzing by ICP-OES

Composition	BaO	SiO_2	CaO	B_2O_3	Additions
mol%	28.5	44.5	9.7	9.9	ZnO, Al_2O_3, V_2O_5
wt.%	48.2	29.8	6.1	7.6	

3.1.2 Ba-Sr system glasses BS

The BS glasses with composition of $BaO–SrO–SiO_2–B_2O_3$ were prepared by the melt-quenching method and designated as glass BS6, BS15 and BS25. They were prepared according to stoichiometric ratio given in Table 3-3 by mixing batch of raw materials ($BaCO_3$, $SrCO_3$, SiO_2 and H_3BO_3) which were purchased from Merck KGaA (Germany) and had a grade of purity higher than 99%. Each batch (100 g) was heated in a platinum crucible at 1500 °C for 3 h with a heating rate 15 °C/min in an electrically heated chamber furnace (Carbolite 1700, England) and poured into ice water to form glass. The glass frits were washed in acetone and dried at 60 °C. They were grinded in a planetary ball mill to a median particle size of 10-13 μm tested via laser particle size analyzer (LA-950). The chemical compositions of BS glasses were analyzed by ICP-OES after alkaline solving and diluting. The results are shown in Table 3-3. For SrO and SiO_2 2% molar divergence was found in BS25 glass compared with nominal composition and as-analyzed composition, which may be caused from preparation process.

Table 3-3. Chemical composition of BS glasses (in mol%)

Composition	Nominal composition, mol%				As-analyzed composition, mol%			
	BaO	SrO	SiO_2	B_2O_3	BaO	SrO	SiO_2	B_2O_3
BS6	30	6	54	10	30.1	6.0	53.9	10.0
BS15	30	15	45	10	30.0	14.7	44.9	10.4
BS25	25	25	40	10	24.5	22.8	42.5	10.2

3.2 Filler materials

For the glass-based composites, different filler materials were added into glass H matrix to improve the joining properties with the membrane STF25 and the substrate Aluchrom. The filler materials included in this study were ceramic and metal powders. The intention for choosing the fillers were enhancing the property of thermal expansion and chemical compatibility as well as to improve the joining behavior of the glass-based sealants. Three different perovskite ceramics (STF25, STF35 and CGO) used for oxygen transport membranes with higher CTEs were mixed with glass H (listed in Table 3-4), all of which were in-house synthesized powders from IEK–1. The ceramic filler powder of $BaSiO_3$ with CTE around 16.9×10^{-6} K^{-1} was in-house synthesized [110] in ZEA-1 and has a mean particle size around 4.4 µm. Another ceramic filler Sr_2SiO_4 was produced by mixing stoichiometric raw materials ($SrCO_3$ and SiO_2) and then sintering at 1350 °C for 30 h. The raw materials were purchased from Merck KGaA (Germany) and had a grade of purity higher than 99 %. The mean particle size of Sr_2SiO_4 was about 12.1 µm. In addition, Ag, Ni, NiCr (80-20) and Fe30Cr5Al0.5Y metal powders were chosen as filler materials and added to glass H. The Fe30Cr5Al0.5Y powder has a similar composition to the sealing partner Aluchrom. An overview of basic information is listed in Table 3-5.

Table 3-4. Different ceramic materials used as fillers

Ceramics	Abbrev.	Particle size [µm]	CTE [$\times 10^{-6}$ K^{-1}] (20–800°C)
$SrTi_{0.75}Fe_{0.25}O_{3-\delta}$	STF25	2.4	10.4-14.0
$SrTi_{0.65}Fe_{0.35}O_{3-\delta}$	STF35	1.1	10.3-12.9
$Ce_{0.8}Gd_{0.2}O_2$	CGO	0.6	10-12 [111]
$BaSiO_3$	--	4.4	16.9 [80]
Sr_2SiO_4	--	12.1	12.5 [80]

Table 3-5. Different metal powders used as fillers

Metals	Abbrev.	Particle size [μm]	CTE [×10^{-6} K^{-1}] (20–800 °C)	Supplier
Ag	Ag	14.7	19.5 [15]	Alfa Aesar
Ni	N	11.7	13.3	Riedel-de-Haen
Ni-Cr (80-20)	NC	11.8	17.3	Höganäs
Fe30Cr5Al0.5Y	FE	--	12.6	Praxair

All in all 18 glass-based composites were prepared by mixing matrix glass H with different filler powders in varying amounts: Ag (20 wt.%, 30 wt.%, 40 wt.%), Ni (20 wt.%, 30 wt.%), Ni-Cr (20 wt.%, 30 wt.%), CGO (20 wt.%), STF25 (10 wt.%), STF35 (10 wt.%), Fe30Cr5Al0.5Y (20 wt.%), BaSiO$_3$ (10 wt.%, 20 wt.%, 30 wt.%) and Sr$_2$SiO$_4$ (10 wt.%, 20 wt.%, 30 wt.%, 40 wt.%). The abbreviations of the above glass-based composites are listed in Table 3-6. For better homogenization, the mixtures were blended in a mechanical shaker (Willy A. Bachofen AG Maschinenfabrik, T2C) for 30 min.

Table 3-6. Abbreviations of glass-based composites

Abbrev	Glass H	Fillers
HAg20	80 wt.%	Ag 20 wt.%
HAg30	70 wt.%	Ag 30 wt.%
HAg40	60 wt.%	Ag 40 wt.%
HN20	80 wt.%	Ni 20 wt.%
HN30	70 wt.%	Ni 30 wt.%
HNC20	80 wt.%	Ni-Cr (80-20) 20 wt.%
HNC30	70 wt.%	Ni-Cr (80-20) 30 wt.%
HFE20	80 wt.%	Fe30Cr5Al0.5Y 20 wt.%
HCGO20	80 wt.%	$Ce_{0.8}Gd_{0.2}O_2$ 20 wt.%
H10STF25	90 wt.%	$SrTi_{0.75}Fe_{0.25}O_{3-\delta}$ 10 wt.%
H10STF35	90 wt.%	$SrTi_{0.65}Fe_{0.35}O_{3-\delta}$ 10 wt.%
HBS10	90 wt.%	$BaSiO_3$ 10 wt.%
HBS20	80 wt.%	$BaSiO_3$ 20 wt.%
HBS30	70 wt.%	$BaSiO_3$ 30 wt.%
HS2S10	90 wt.%	Sr_2SiO_4 10 wt.%
HS2S20	80 wt.%	Sr_2SiO_4 20 wt.%
HS2S30	70 wt.%	Sr_2SiO_4 30 wt.%
HS2S40	60 wt.%	Sr_2SiO_4 40 wt.%

3.3 Chemical compatibility of filler materials with glass H matrix

The compatibility tests were performed for the composites mixed with perovskite ceramics (STF25, STF35, and CGO) and metals fillers (Ag, Ni, Ni-Cr, and FE). After thoroughly machine blending, the mixtures were subsequently pressed into pellets with a diameter of 10 mm and sintered at 850 °C for 10 h with a heating rate of 2 °C/min. Scanning electron microscopy (SEM, Zeiss Sigma VP) and energy dispersive spectroscopy (EDS, Oxford) analyses were carried out on cross-sections to investigate the compatibility of reinforcement fillers (perovskite ceramics and metals) and the glass H matrix. Besides, thermogravimetry (TG) analyses of the STF powders and mixed samples with glass H were performed up to 1300 °C with heating rate 15 °C/min and employed by a commercial instrument Linseis (STA PT 1600) in alumina crucibles under air atmosphere.

3.4 Thermal analysis

Thermal analysis is a technique that analyzes the relationship between thermodynamic or physical parameters versus temperature. It is mainly used to determine the thermal energy, thermal stability, thermal decomposition and phase transition processes of materials. Differential scanning calorimetry (DSC) measurement was carried out for glass H and BS glasses. A commercial DSC instrument Linseis (STA PT 1600) was employed with a heating rate of 15 °C/min up to 1300 °C in an alumina crucible under air atmosphere. The measurement of the phase transition temperatures was carried out with an accuracy $\pm$ 2 °C. Glass transition temperature (T_g), onset crystallization (T_r), crystallization peak temperature (T_p), and onset melting temperature (T_m) were determined. The glass-forming tendency and the thermal stability against crystallization of glass were evaluated via DSC data using Hrubý's equation [112] (3.1), which is based on the relative onset temperatures, T_g, T_r and T_m:

$$K_{gl} = \frac{T_r - T_g}{T_m - T_r}$$
(3.1)

where $0.1 \leq K_{gl} \leq 1$. If $K_{gl} = 0.1$, the preparation of glass is very difficult and requires additional technical help [113]. For a K_{gl} close to 0.5, glass can be prepared simply by free cooling the melt in air. For $K_{gl} = 1$, glass is a high molecular polymer [112].

3.5 Crystallization analysis

3.5.1 X-ray diffraction

X-ray powder diffraction (XRD) uses X-rays to irradiate polycrystalline samples to obtain X-ray diffraction patterns. The measured diffraction pattern exhibits peak positions and intensities that characterize the phases in the sample. That could be explain by the Bragg equation (3.2)

$$n\lambda = 2d_{hkl} \sin\theta$$
(3.2)

where n is the order of diffraction, λ is the wavelength of radiation, d_{hkl} is the spacing between lattice planes with Miller indices hkl, and θ is the reflection angle. Bragg's law is schematically demonstrated in Fig. 3-1 [114].
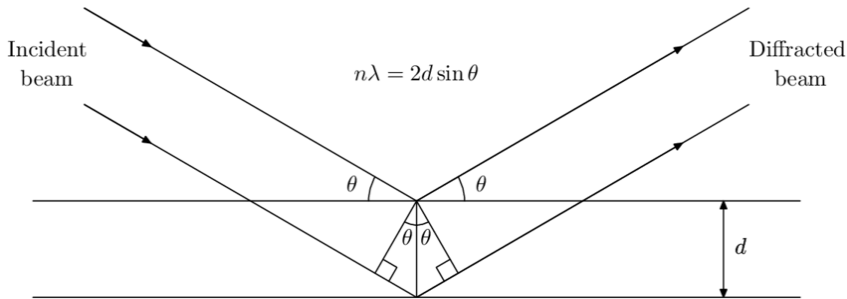
Fig. 3-1. Schematic illustration of Bragg's Law [114]

There are enormous functions by means of XRD, such as, the qualitative and quantitative analysis of the phase, the determination of the lattice parameters, the analysis of the crystal structure, the determination of the structure and the grain size.

To investigate the phases formation at OTM application temperatures, Glass H and BS glasses were heated at different heating processes on a platinum foil. After grinding in an agate mortar X-ray powder diffractometer (XRD, D4 Endeavor, Bruker AXS GmbH) was used to test powder samples after heat treatment.

3.5.2 FactSage simulation

The FactSage computer package consists of a series of thermochemical information, calculation and manipulation modules that enable one to access and manipulate compound and solution databases [115, 116]. By this commercial software FactSage it is possible to simulate and predict the potential phases formed in glass sealant depending on temperature under equilibrium conditions. FactSage has been often used for simulating crystalline phases equilibrium versus temperature in industrial wastes, such as slags and fly ash [117-119]. In this study, FactSage 8.1 software was applied with inner FTox databases. Gibbs energy was minimized in the system. All possible reactions and phase equilibria were considered. The equilibria state (phase composition) was calculated depending on temperature at constant and pressure p = 1 bar.

3.6 Dilatometric measurement

Thermal expansion is extremely important when considering which materials will be used in systems that experience fluctuations in temperature. Thermodilatometry is a technique used to monitor the changes in dimensions of area, shape, length or volume against time and temperature. A principal utilization for a dilatometer is the calculation of thermal expansion of a substance [120].

The linear thermal expansion coefficient (CTE or α) can be calculated according to the following equation (3.3)

$$\alpha = \frac{1}{L_0} \times \frac{\Delta L}{\Delta T}$$ (3.3)

where ΔL is the length change during temperature change ΔT, and L_0 is the initial length of the sample. The volumetric thermal expansion coefficient (β) commonly is three times the coefficient of linear thermal expansion (α) from experimental data of isotropic solid materials. From an atomic perspective, the CTE reflects an increase in the average distance between atoms with increasing temperature.

In this study, linear dilatometric measurements were performed with a dual rod Linseis L75 dilatometer (Germany) at a heating rate of 3 °C/min. Each measurement was carried out three times with the specimen being used only once to prevent possible microstructural modifications, as the procedure would inherently imply an additional thermal effect.

For glass-based composites samples and glass H, the dilatometer rods were pressed under a load of 2.5 tons and sintered at 850 °C for 10 h on a platinum foil. Afterwards they were then cut into 25 mm long bars. Some of the sintered bars were annealed at 800 °C for 1000 h before carrying out dilatometer measurement with same heating rate.

The preparation of dilatometric samples of BS glasses is similar to glass H composites except the heating processes. The thermal treatment of BS glasses was sintering at 900 °C for 1 h with the same heating rate 2 °C/min. Some of the sintered BS bars were annealed at 850 °C for 50 h additionally.

In order to find out which crystal phases were formed after long-term annealing, microstructures analyses for the polished cross-sections of the annealed dilatometer samples were carried out via a scanning electron microscope (SEM, Zeiss Sigma VP) and energy dispersive X-ray analysis spectroscopy (EDS X-Max[N], Oxford).

3.7 Sinking dilatometer

Sinking dilatometric measurements were carried out in a commercial apparatus Netzsch 402 ES with an espacially designed adapter applying a load of 261 g at a heating rate of 2 °C/min. The shrinkage behavior of a glass sealant layer is measured by the sensor on the surface of the 2nd steel disk (Fig. 3-1) with the resolution of about ± 1 μm [121]. The temperature-time-pressure-dependent glass sealant shrinkage behavior was examined using this measurement and the joining process of an OTM stack can be simulated realistically [122]. For preparing shrinkage samples, the glass pastes were made by mixing an organic binder solution with glass powders. The pastes were applied on the Crofer 22 APU® wafers (Ø 18 mm, 0.5 mm), then put into a drying chamber at 60 °C for 3 h. The green layer after drying has a thickness around 200 μm.
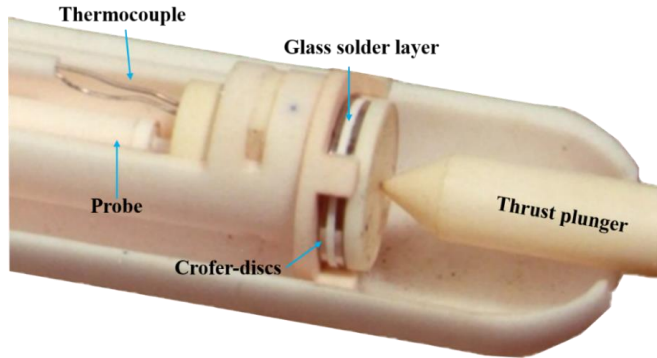
Fig. 3-2. Probe head of the sinking dilatometer

3.8 Hot stage microscopy (HSM) for investigating viscous behavior

Suitable creep deformation and viscous flowing behavior are essential for glass-based sealants using in OTM stack. If the viscosity is too high, the sealant will not creep or flow enough to achieve gastight structures and it also will not be able to dissipate thermal expansion mismatch stresses [47]. If the viscosity is too low, the sealant will flow out from the joining gap, which would contaminate other components in the stack and cause gas leakage. From the common science, glass viscosity is dropped with the temperature rise. Besides, sealant viscosity also varies with glass composition and filler content. It is important to find the optimum joining temperature for each different glass sealant in order to achieve suitable viscous flow and gas-tight joints.

Hot stage microscope (HSM) is a useful apparatus to measure sintering of pressed powder pellets between glass deformation range to glass flowing range (i.e. shrinkage point to melting point) by monitoring the change of geometric shape. Pascual et al. [73] proposed a method for obtaining viscosity-temperature data for glasses on the basis of the characteristic points obtained by hot stage microscopy in the range $3 < \log(\eta) < 10$ (viscosity η in dPa·s). The fixed viscosity points attained by HSM are listed in Table 3-7.

Table 3-7. Fixed viscosity points [73]

Characteristic fixed points	Viscosity $\log(\eta)$ / dPa·s
First shrinkage	9.1 ± 0.1
Maximum shrinkage	7.8 ± 0.1
Deformation	6.3 ± 0.1
Sphere	5.4 ± 0.1
Half ball	4.1 ± 0.1
Flow	3.4 ± 0.1

Thermo optical measuring instrument TOMMIplus is a larger dimensioned hot stage microscope to measure creep deformation and viscous behavior at elevated temperatures, which is suitable for large sized sample up to a few centimeters. TOMMIplus is developed by Fraunhofer Institute for silicate research (ISC, Germany). The specimen is backlit illuminated inside the furnace and projects a silhouette that is captured by a CCD (charge-coupled device) camera and recorded by the computer for image analysis.

In this study, seven candidate glass-based sealants: HAg40, HNC30, HBS30, HS2S20, BS6, BS15 and BS25 were investigated by HSM (TOMMIplus) to monitor the creep deformation and viscous melting behavior as function of temperature. The pellets (Ø 10 mm) for TOMMIplus specimens were pressed from the sealant powders with a pellet weight of 1.5 g each. The measurements were conducted at a fast heating rate 15 °C/min from room temperature to 500 °C and a 5 °C/min rate to 1100 °C.

3.9 Glass-based sealant green foil preparation for joining application

Two methods are available in ZEA-1 of Forschungszentrum Jülich to prepare glass-based sealant green foils for OTM stack joining application: robot syringe dispensing and screen printing. The robot syringe dispensing method has relatively high flexibility concerning application geometry at low material consumption and is suitable for the exploration of optimum glass-based sealant and joining processes. For some glass-based sealants with high CTE and good joining behavior, such as HAg40 and HNC30, screen printing was used to prepare green foils in large amount.

3.9.1 Robot syringe dispenser

For the application of BS glass to a sealing geometry, a paste was prepared by adding BS15 glass powder (82 wt.%) and an 18 wt.% binder solution consisting of ethyl cellulose and α-terpineol with blending them thoroughly by mechanical stirring. Then the paste was blended using an ultrasonic finger (Branson 900B) to avoid agglomeration. The paste was subsequently applied via a syringe-controlled dispenser by Nordson EFD dispensing robots (DR-2503N) on the steel or polyester film surface at a constant temperature 24 °C. The pastes were dried at 60 °C in a ventilated heating chamber overnight. Foils were achieved and ready for next assembling process. Fig. 3-3 shows the foil preparation process by syringe dispensing.
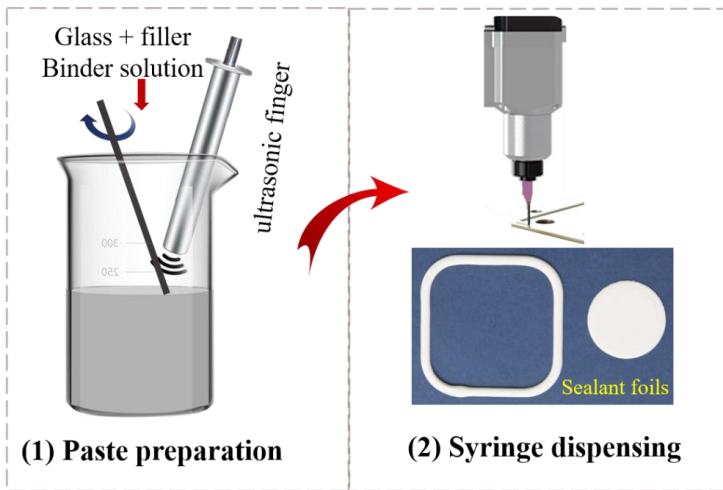
Fig. 3-3. Schematic diagram of robot syringe dispensing process, (1) paste preparation, (2) syringe dispensing and sealant foils

3.9.2 Screen printing

Sealant green foils were prepared by screen printing technique and followed by a drying process. Fig 3-4 shows the foil preparation process. First, a paste was prepared by adding a glass composite powder mixture (77 wt.%) and counterweighted organic solvents in sequence, the composition as seen table 3-8. A planetary centrifugal mixer (THINKY, ARV-930TWIN) was employed to help to the paste uniform mixing and dispersion as well as deaeration at the same time. The viscosity of the paste for screen printing was evaluated by a Rheometer (BrookFIELO, RS3CPS) at a standard temperature 29.7 °C. The optimal viscosity for the screen printing pastes was found around 30-50 Pa.s depending on the glass composites. The viscosity of HAg40 paste was tested 45.7 Pa.s at room temperature. The viscosity of HNC30 paste was detected 31.8 Pa.s. An electric flat screen-printing machine (ESC–AT 60 P, Germany) was employed subsequently. The paste of the glass

composite sealant to be screen printed is pressed through the screen by means of a squeegee. After leveling on the polyester film surface, the printed wet paste foils were dried in a ventilated heating chamber at 60 °C for 2 h in the air atmosphere. The green foils can be stamped or cut easily into suitable geometry for later joining application. The thickness of glass sealant green foil is around 0.5 mm.

Table 3-8. Composition of screen-printing paste

Component	Amount in g	Amount in wt.%
Glass composite powder	154	77
Binder solution BM23-2 (88% Terpineol + 12% Mowital)	39.78	19.89
Disperbyk-110	1.78	0.89
Poly (ethylene glycol) bis (2-ethylhexanoate)	4.44	2.22
sum	200	100
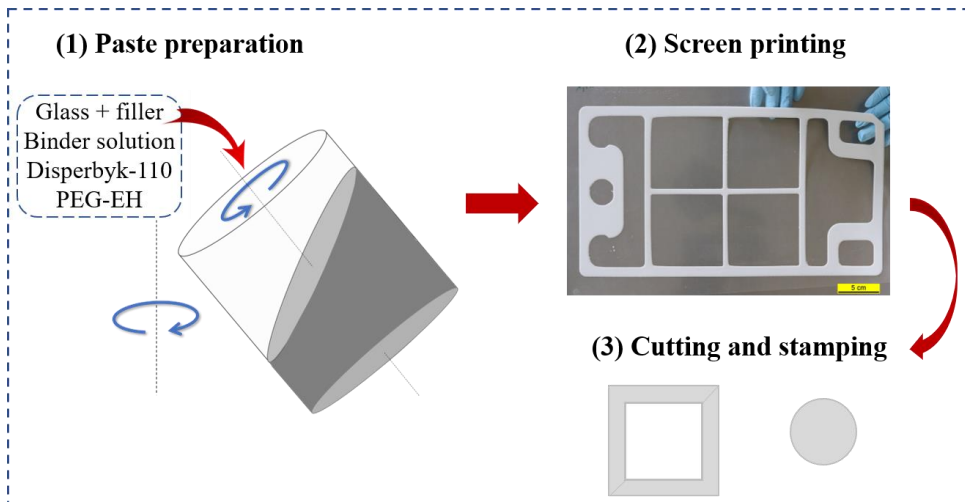
Fig. 3-4. Schematic diagram of screen-printing process, (1) paste preparation, (2) screen-printed sealant green foil, (3) cutting and stamping suitable shapes for next assembling process

3.10 Joining tests and analyses

In order to investigate joining performance of glass-based sealants HAg40 and HNC30, two setups were designed as seen in the schematic illustration of Fig. 3-5. Sealant green foils were assembled in the middle between metal plates and membrane STF25. Then the sealing process was performed by heating to a temperature of 350 °C and dwelling for 30 min for binder burn-out with a subsequent increase in temperature to 850 °C for 10 h in air. The heating rate for the joints is slow and around 2 °C/min, in order avoid the differences of temperature that could provoke stresses and possible curvatures or cracks in the materials.

The gas tightness setup to investigate the sealing behavior is presented in Fig. 3-5 (a). The gas-tightness test was performed on two steel plates with a size of 48 × 48 mm², one of which had a drilled hole with a 10 mm diameter in a sandwiched structure. The sealant paste was applied in the middle layer of the sandwich on the outer circumference of one steel plate and heating was carried out with a dead load of 800 g on the top steel plate. Using two steel plate joining with glass sealant to evaluate glass sealing behavior, one can avoid the disturbance from other factors, such as, the leakage caused by cracking of STF25 during the heating process, intrinsic permeability as property of STF25 itself and the interfacial reaction between membrane and glass sealant. Three steel variants were used in this gas-tightness study: as-delivered Aluchrom, pre-oxidized Aluchrom and Crofer 22 APU. The pre-oxidation was carried out by heating to 1250 °C and subsequent dwelling for 5 h before cooling to room temperature. Three or four small yttria-stabilized ZrO_2 (YSZ, KERAFOL® – Keramische Folien GmbH) spacers with a thickness of 0.15 µm were placed between the hole of the plate and the sealant foil in order to keep a distance between two plates. The gas tightness of the sandwiched samples was evaluated by helium leak testing (UL 200, Inficon). The leaking samples were inspected by red ink penetration and optical microscopy.

In addition, the sealant foils were placed between the steel plate and the membrane STF25 wafer (Ø 16 mm) as seen Fig 3-5 (b). The setup was placed into a muffle furnace for the joining process described above and under a dead load of 400 g. The steel plates used for the asymmetric sealing test with STF25 were as-delivered Aluchrom and pre-oxidized Aluchrom. The joining performance of the sealants with the STF25 and the steel was evaluated by performing microstructural analysis on the cross-sections of the samples with a scanning electron microscope (Zeiss Sigma VP) together with an energy dispersive X-ray spectrometer (Oxford).
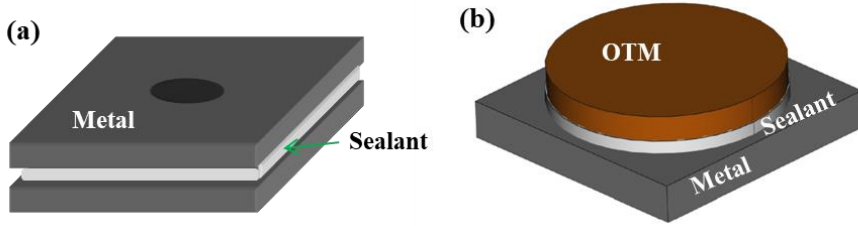
Fig. 3-5. Schematic illustrations of joining geometries: (a) sealant sealing metal plates for gas-tightness testing, (b) sealant assembled with OTM and metallic support

3.11 Mechanical test

Shear stress is an important parameter to evaluate the performance of a glass-based sealant in OTM module operation conditions. An in-house torsion set-up [123, 124] has been developed at Institute of Energy and Climate Research, Microstructure and Properties of Materials (IEK-2), Forschungszentrum Jülich. The torsion tests were performed for HAg40 and HNC30 sealants at room temperature.

In the torsion test, the jointed specimens were fixed by two opposite loading arms, then twisted with a speed of 4 °/min until fracture occurred. The maximum torque can reach to 220 N·m. The shear stress (τ) can be calculated using equation (3.4) and (3.5) [125]:

$$\tau = \frac{T}{J} x \tag{3.4}$$

$$J = \frac{\pi}{2}(R_o^4 - R_i^4) \tag{3.5}$$

where T is the applied torque, J is the sectional polar moment of inertia, χ is the radial coordinate, R_o is the outer radius, and R_i is the inner radius of joining part area.

Hourglass shaped samples were prepared for torsion tests, as seen Fig 3-6. A ferritic steel Crofer22H® (VDM) was machined into miniaturized Hourglass shaped sample and head to head joined by two different composite sealants (HAg40 and HNC30). Table 3-9 lists the composition of Crofer22H®. It has good creep strength because of Laves phase precipitates. The sealant foils were prepared by screen printing method, then stamped into a ring with 25 mm out diameter and 18 mm inner diameter. The joining area is a ring with 25 mm outer diameter and 18 mm inner diameter. Crofer22H® one side was drilled through the whole thickness with a 5.5 mm hole in order to reduce the joined surface to an annular shape. The assembled samples were joined after binder burnout at 850 °C for 10 h in a furnace (Nabertherm) under a deadload 3900 ± 100 g, in order to get a thin connection layer around 0.2 mm. Five samples for every sealant were prepared identically for the strength measurement at room temperature. The fractured specimens were embedded in

Epoxy resin, then subsequently diamond-cut for a detailed cross-sectional analysis by means of scanning electron microscope (SEM).
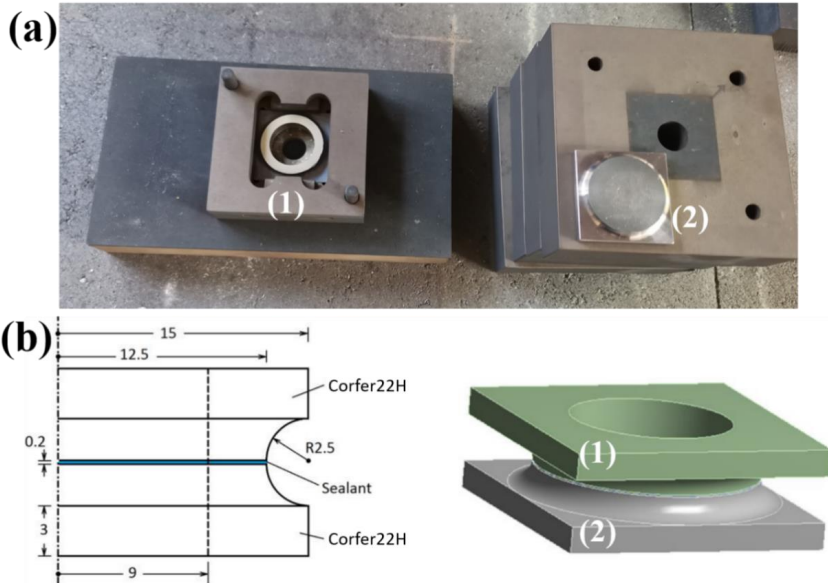
Fig. 3-6. (a) Assembling of hourglass shaped torsion specimen process, sealant was placed in the middle of two Crofer22H plates for further joining at 850 °C for 10 h under a deadload 3900 ± 100 g; (b) schematic of the hourglass shaped specimens [125] after joining, the dimensions are in mm. (1) is Crofer22H plate with an inner hole of Ø 18 mm and green foil of sealant applied to it (2) is opposite Crofer22H plate without hole.

Table 3-9. Chemical composition of Crofer22H®

	Composition wt.%						
	Fe	Cr	Nb	Si	W	Mn	Additions
Crofer22H	73.8	22.0	0.6	0.4	2.0	0.4	C, Ti, Ni, La, Cu, P, N, S

3.12 Thermal cycling

Thermal cycle testing is performed on sealants to determine the resistance of alternating exposure between OTM operation high temperature and room temperatures. Upon several heating and cooling cycles, thermal stresses are generated, mainly due to the difference in coefficient of thermal expansion (CTE) between the OTM stack components and imperfection at the interface regions or inside of the sealant. The level of thermal stresses accumulating during thermal cycles could be severe enough to cause sealant joint cracking, open pores, warpage, damage to leads hermetic seal failures.

The glass composites of HAg40 and HNC30 were selected for a thermal cycling study (2-50 cycles) under 800 °C since adequate CTE and their joints with OTM stack components exhibited excellent joining characteristics after 850 °C 10 h joining. Two type setups were prepared as seen schematic illustration Fig. 3-5. One is sealant joining with metal plates for gas-tightness testing. Another one is sealant assembled with OTM and Aluchrom. The sealants green foils were prepared by screen printing. After thermal cycling, the gas leakage and the cross-sections of the joints were investigated.

Thermal cycling tests were carried out in a muffle furnace with static air from room temperature to 800 °C and dwelling one hour then cooling down to room temperature for different cycling times. The temperature of 800 °C was chosen as typical OTM operation temperature. The heating and cooling rate are 2 °C/min in order to avoid thermal shocking to provoke stresses and possible curvatures or cracks in the materials. Gas tightness joints were taken out from the furnace to record Helium leakage rate after 2 times cycling, 5 times cycling, 10 times cycling, 20 times cycling, up to 50 times cycling. Assembled joints with Aluchrom and STF25 after cycling two and five times were evaluated by performing microstructural analysis on the cross-sections of the samples with a scanning electron microscope (Zeiss Sigma VP) together with an energy dispersive X-ray spectrometer (Oxford).

3.13 Long-term thermal stability

Thermal stability of glass-based sealants must be considered for OTM long time operation. Glass-based sealants HAg40 and HNC30 were used in this experiment. The sealants foils were prepared by screen printing and later cutting methods. After joining process at 850 °C for 10 h, the gas tightness setups (Aluchrom/sealant/Aluchrom) were exposed at a furnace under 800 °C for 500 h, 1000 h, and 1500 h in static air, simulating long thermal treatment. The heating and cooling rate are 2 °C/min. Helium leakage tests were carried out at room temperature for every as-joined sample and after long term thermal treatment sample. Leakage rate was recorded, and the less gas-tight sample was inspected by red ink penetration and optical microscopy.

3.14 Fast joining process investigation

In order to save energy and time during joining process, fast joining processes were investigated. According to previous studies on the glass composites HAg40 and HNC30, good joining behaviors were achieved at 850 °C for 10 hours. The glass sealant green foils were prepared in large amount by screen printing for fast joining process investigation. Thermal parameters for fast joining processes (temperature and dwell time) were determined according HSM results in analogy to brazing processes. For HNC30 sealant, the half ball temperature is at 920 °C, and four joining processes were adopted, (1) 880 °C 15 min + 920 °C 5 min, (2) 920 °C 5 min, (3) 900 °C 15 min, (4) 880 °C 30 min. For HAg40 sealant, the half ball temperature is at 935 °C, and four joining processes were tried, (1) 935 °C 5 min, (2) 920 °C 15 min, (3) 900 °C 30 min, (4) 880 °C 30 min. The slow heating and cooling rate are both adopted at 2 °C/min to avoid thermal differences that provoke stress, curvature, even cracks.

In order to investigate the feasibility of fast joining process for the glass composite sealant, a gas tightness test was performed on the double layered Aluchrom plates, and an assembling test was carried out on the STF25 membrane and Aluchrom. The setups were placed into a muffle furnace for the joining process described as above under a dead load. The gas tightness of the sandwiched samples was evaluated by helium leakage detection (UL 200, Inficon). The analysis of x-ray computed tomography (CT) was employed to non-destructively check the inner microstructural conditions of glass sealant between support metals and STF25. The CT instrument used in this study has been developed in the research center of Jülich [126] with a resolution of 100 µm and accuracy about 1 µm, as seen Fig. 3-7. CT is suitable for high resolution detection without destruction. The joining performance of the sealants with the STF25 and the steel was evaluated by performing microstructural analysis on the cross-sections of the samples with a scanning electron microscope (Zeiss Sigma VP) together with an energy dispersive x-ray spectrometer (Oxford).

Fig. 3-7. Open X-ray computed tomography system at ZEA-1

3.15 Other glass-based sealants joining process

HBS30

According to the shrinkage performance of HBS30 from hot stage microscopy, the joining behaviours were analysed under three different heating processes 850 °C 10 h, 920 °C 15 min and 960 °C 5 min. The gas tightness of the sandwiched samples was evaluated by helium leakage detection. In addition, the sealant HBS30 was joined with steel plate and the membrane STF25 wafer and measured by CT and SEM analysis.

HS2S20

According to the shrinkage performance of HS2S20 from HSM, the joining behaviors were examined under different heating processes (1) 850 °C 10 h, with deadload 800 g, (2) 850 °C 10 h, with deadload 1200 g, (3) 920 °C 15 min, with deadload 800 g and (4) 960 °C 10 min with dead load 520 g. Gas tightness and microstructure of the joints were examined.

BS15

In order to investigate the joinability of BS15 glass, a gas tightness test was performed on the double-layered steel plates and a joining test was carried out on the STF25 membrane and steel plate. The joining process was performed by heating to a temperature 1075 °C with a dwell time 5 min in air. Four small ZrO_2 spacers with 0.15 µm thickness were placed between the hole of the plate and sealant foil in order to keep a minimal distance for gas tightness setup. Heating process was carried out with a dead load of 800 g on the top steel plate of the sandwiched setup. The deadload of joint with STF25 used is 60 g. Gas leakage rate and microstructure of the BS15 joint were investigated.

4. Results and discussion

4.1 Glass matrix H: investigation of thermal properties and crystallization

4.1.1 General effects of glass crystallization on the joining behavior

Oxygen transport membrane (OTM) technology is prospected for CO_2 capture from exhaust gas [127] or producing synthesis gas from carbon fuels [8], which is a good strategy to lighten the environmental stress from greenhouse gases [3]. For instance, $SrTi_{0.75}Fe_{0.25}O_{3-\delta}$ (STF25) perovskite membrane was developed since 2009 [40, 128, 129] and is considered to be a promising candidate for OTM application due to favorable oxygen semi-permeation, excellent mechanical properties and high chemical stability at working environment [22, 41, 128, 130]. In OTM module stack, gastight sealants with suitable thermal expansion must be applied to join membranes and counterparts together in order to prevent gas mixing during high temperature working, which is also a key challenge in the module design.

Glass sealants have been developed and studied extensively as they are promising joining material with tailorable composition and thermal properties [16, 131, 132]. Besides, glass sealant commonly wouldn't be affected by the oxidation or reduction working environment and has a good heat resistance during operation over 700 °C [98, 133]. The joining process happened during glass viscous flow and wetting ceramic membrane and metal counterparts, above glass softening point. Moreover, there is possible to increase the formation of crystalline phases and reduce the glassy phase by a suitable thermal treatment for glass sealant in order to tailor the glass creep behavior. Whereas, for multi-element complex glass systems, the glass crystallization during heating is difficult to control, and the crystalline phases may affect the sealing performance. The thermal expansion behavior of a glass-ceramic sealing material partially depends on the thermal expansion of the crystalline phases, precipitated from the glass. The low thermal expansion and the change of thermal properties caused by the crystallization of the glass would lead to cracking and even gas-leakage during joining or OTM operation process above 800 °C [62]. So, to know the crystalline behavior of glass sealant is important and worthy at the high temperature joining and operation period. The thermochemical software package FactSage includes the largest set of evaluated and optimized thermodynamic databases for inorganic systems in the world [115]. It is possible to simulate and predict the potential phases formed in glass sealant depending on temperature under equilibrium conditions by this commercial software FactSage. FactSage has been quite often used for simulating crystalline phases equilibrium versus temperature in industrial wastes, such as slags and fly ash [117-119]. No studies have been done to simulate the crystallization behavior for glass sealant. Computational modelling of glass sealant crystallization behavior is of wide interest for property optimization.

Barium calcium silicate glass "H" was investigated as a sealant matrix for joining OTMs because of its excellent viscosity, chemical compatibility, and joining properties demonstrated in solid oxide fuel cell (SOFC) applications [20]. Brendt et al. [94] reported the crystallization behavior of

glass H only below 850 °C at time being for SOFC. The observation or simulation of crystallization behavior of glass H at other temperatures has not been studied.

In this study, thermal stability, thermal expansion and crystalline behavior on the barium-calcium-silicate (BCS) system glass matrix H were investigated by Differential Scanning Calorimetry (DSC), dilatometer and X-ray powder diffractometer (XRD) respectively, and FactSage was introduced to plot the phase equilibrium and predict crystalline phases versus temperature for the composition of the glass H.

4.1.2 Thermal analysis and thermal stability calculation

The DSC plot of glass matrix H at a heating rate of 15 °C/min is shown in Fig. 4-1. Glass transition temperature (T_g) of glass H is at 621 °C. As can be seen, it shows an intense exothermal peak between 735 °C (T_r) to 764 °C (T_p) which related to precipitation of crystalline phases. Onset meting temperature (T_m) is around 968 °C. But there is no significant melting endothermic peak (T_{mp}) at the testing temperature range up to 1300 °C. The glass-forming tendency and the thermal stability against crystallization on heating this glass was estimated by the Hruby's methods [112] and DSC data. The parameter K_{gl} of glass H was calculated to be 0.49 according to equation (e.1). $K_{gl} = 0.5$ means glass is easily prepared merely by free cooling of the melt in air [112]. The higher is the value of K_{gl} for a certain glass, the higher is its glass forming tendency and thermal stability against crystallization [134, 135]. This indicated that the glass H has a good glass-forming tendency and great stability against crystallization.
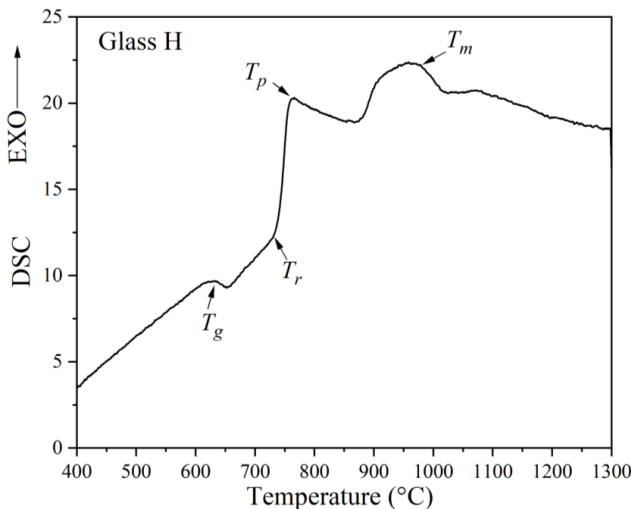
Fig. 4-1. (a) DSC thermograms of glass H at a heating rate of 15 °C/min

4.1.3 Thermal expansion behavior of glass H

The thermal expansion behaviors of the sintered rod glass H and the annealed glass H specimen are shown in Fig. 4-2. According to the results, there is a noticeable glass transition temperature not only shown in the dilatometer curve of glass H but also shown in the sample after 1000 h annealing under 800 °C. The glass transition temperature obtained from dilatometer plots coincides with the DSC result. Result indicates that the residual glass phase is still existing after long term aging for glass H. To verify these findings, cross-sections of the end parts of dilatometer rods were prepared and analyzed by SEM. Microstructures of glass H and the annealed glass H sample are presented in Fig. 4-3. There are some crystalline phases formed and residual glass phase is in large amount in the as-sintered glass H. Whereas, after 1000 h annealing, the glass phase is consumed in large amount as crystals have grown and the number of crystals increased. It implies that small amount of the residual glass phase is left. Amorphous material is located at the grain boundaries of the highly crystallized glass sealant, which also verifies that glass H possesses a good thermal stability against crystallization. The existence of residual glass is important for ensuring that the seal is suitable in terms of viscosity, rigidity, and appropriate gas-tightness during its high-temperature application, such as OTM. The dilatometric softening temperature (T_s) of glass H is above 900 °C, which is in agreement with the literature [109]. The thermal expansion coefficient (CTE) value of glass H is 8.5-10.8 × 10^{-6} K^{-1} (200–900 °C). The CTE value of the annealed samples decreased comparing to the as sintered glass H. The sample after annealing has a CTE 8.0-9.6 × 10^{-6} K^{-1} (200–900 °C). Both of them are a bit lower than the desired CTE (12 × 10^{-6} K^{-1}) of OTM components, i.e., STF25 and Aluchrom. These findings suggest that a strategy is necessary to release thermal stresses caused by CTE mismatch if glass H is used as sealant for the OTM module. Therefore, filler reinforced composites on basis of glass H will be investigated in detail in the following.
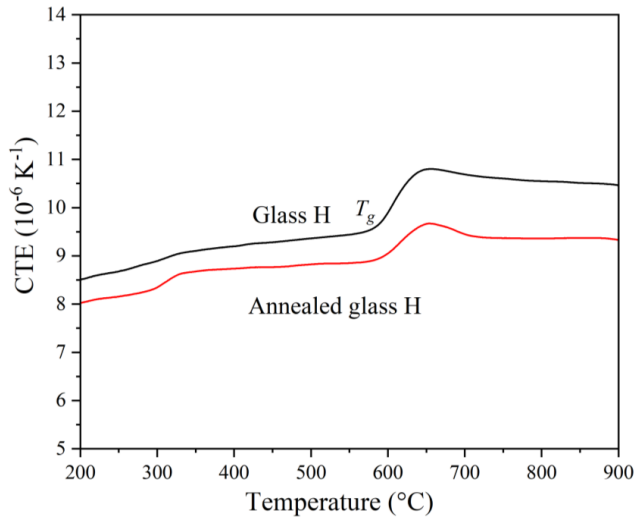
Fig. 4-2. Dilatometer plots of the sintered glass H rod (850 °C, 10 h) and glass H aged sample (850 °C, 10 h + 800 °C, 1000 h)
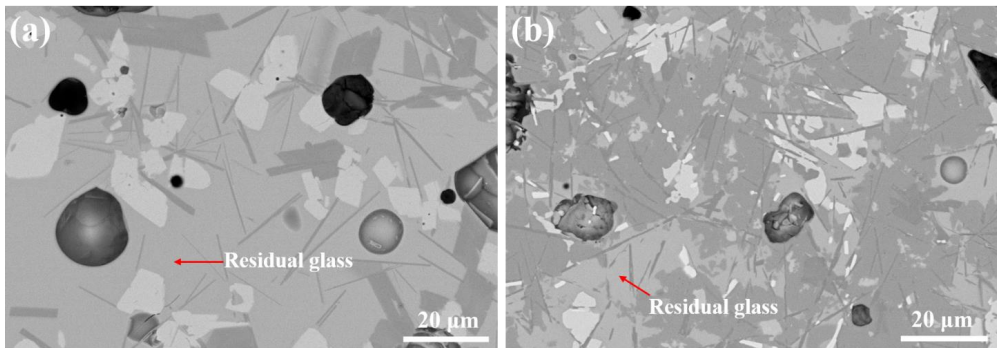
Fig. 4-3. SEM micrographs of dilatometer samples, (a) glass H sintered at 850 °C for 10 h, (b) the annealed glass H sample sintered at 850 °C for 10 h then aged at 800 °C for 1000 h.

4.1.4 Crystallization behavior of glass H

In order to investigate the crystallization behavior of glass H and to explain why CTE values of the aged glass H decreased after annealing, the XRD analysis was performed for the different heat-treated samples supported by simulations of thermodynamically stable phases using FactSage.

XRD patterns of the annealed glass H samples at 6 different heat-treatment processes were shown in Fig. 4-4, (a) 764 °C (T_p) for 20 h, (b) 800 °C for 20 h, (c) 850 °C for 10 h, (d) 920 °C for 20 h, (e) 850 °C for 10 h plus 800 °C for 1000 h. XRD analyses show a significant amorphous broad diffuse hump in all short-term (10-20 hours) annealed samples. The only crystalline phase

precipitated after heating at the crystallization peak temperature (T_p) 764 °C for 20 hours is barium silicate ($Ba_5Si_8O_{21}$), as seen in Fig. 4-4 (a). At temperature of 800 °C and above additionally hexagonal barium aluminosilicate phase $BaAl_2Si_2O_8$ (also called Hexacelsian, high temperature phase) is present, Fig. 4-4 (b-d). The amorphous fraction of these sample remains high, i.e. 93-98 wt.%, listed in Table 4-1.

After long term annealing, i.e. 1000 h, the sample is highly crystalline, as seen in Fig. 4-4 (e). The amount of residual glass phase is reduced dramatically to 7.1 wt.%, which is in good agreement with SEM results (Fig. 4-3 b). XRD analyses of long-term annealed samples reveal the presence of gehenite phase $Ca_2Al_2SiO_7$, barium zinc silicate $BaZnSiO_4$ and Itsiite phase, $Ba_2CaB_2Si_4O_{14}$, in addition to the still remaining phases barium silicate $Ba_5Si_8O_{21}$ and Hexacelsian $BaAl_2Si_2O_8$. Including Itsiite the Rietveld refinement provides a satisfying fit. Quantification results indicate an increase of $Ca_2Al_2SiO_7$ and $Ba_5Si_8O_{21}$ on the cost of $Ba_2CaSi_4B_2O_{14}$, table 4-1. However, it should be noted that the fit for such complex phase mixtures with high number of parameters the numerical fit of the measured data in general becomes more uncertain compared to less complex systems. In the particular case of 1000 h annealing, the thermal displacement parameter of the $BaZnSiO_4$ for instance appears problematic and reaches its limit of certainty. Although the statistical quality of the fits is acceptable, the quantification of the individual phases has some uncertainty. Nevertheless, the qualitative phase composition identified in the samples is fully conclusive.

Itsiite, dibarium calcium bis (heptaoxoborodisilicate) is a new mineral phase which was found in 2014 by Kampf and Joy [136]. In the following, this phase could be confirmed after crystallization of similar glass composition [94]. The formation of major phase Itsiite $Ba_2CaB_2Si_4O_{14}$ in glass H is benefit for reduction of boron volatility and provides potential self-healing mechanisms according to some similar research for borate-containing crystalline phases in glass sealants [102, 137] could be possible. This leads to the great improvement of thermal stability of resulting glass-ceramic sealant. However, there is no investigation of thermal expansion coefficient of Itsiite published up to now.

The CTE of other phases detected by XRD, barium silicate $Ba_5Si_8O_{21}$, Hexacelsian $BaAl_2Si_2O_8$, calcium aluminosilicate $Ca_2Al_2SiO_7$ and barium zinc silicate $BaZnSiO_4$ are about $14.5 \times 10^{-6}\,K^{-1}$ [138], $7.5 \times 10^{-6}\,K^{-1}$ [82], $7.9 \times 10^{-6}\,K^{-1}$ [139], and $10.4 \times 10^{-6}\,K^{-1}$ [140], respectively. Barium silicates are desirable phases in crystallized glass H based sealant due to their relatively high CTE values. However, low CTE phases Hexacelsian $BaAl_2Si_2O_8$ and calcium aluminosilicate $Ca_2Al_2SiO_7$ are also formed in glass H, which is the main reason that CTE values of the aged glass H sample decreased after 1000 h annealing. In some case, the Al_2O_3 concentration in the glass composition should not be too high, because under OTM working conditions the formation of unfavorable phases, $BaAl_2Si_2O_8$, $Ca_2Al_2SiO_7$, is possible. All studied barium silicates [138] exhibit CTEs in a range suitable for components of sealing materials in high temperature oxygen transport membranes, which could provide an additional idea for designing the optimum glass-ceramic sealants for OTM application.
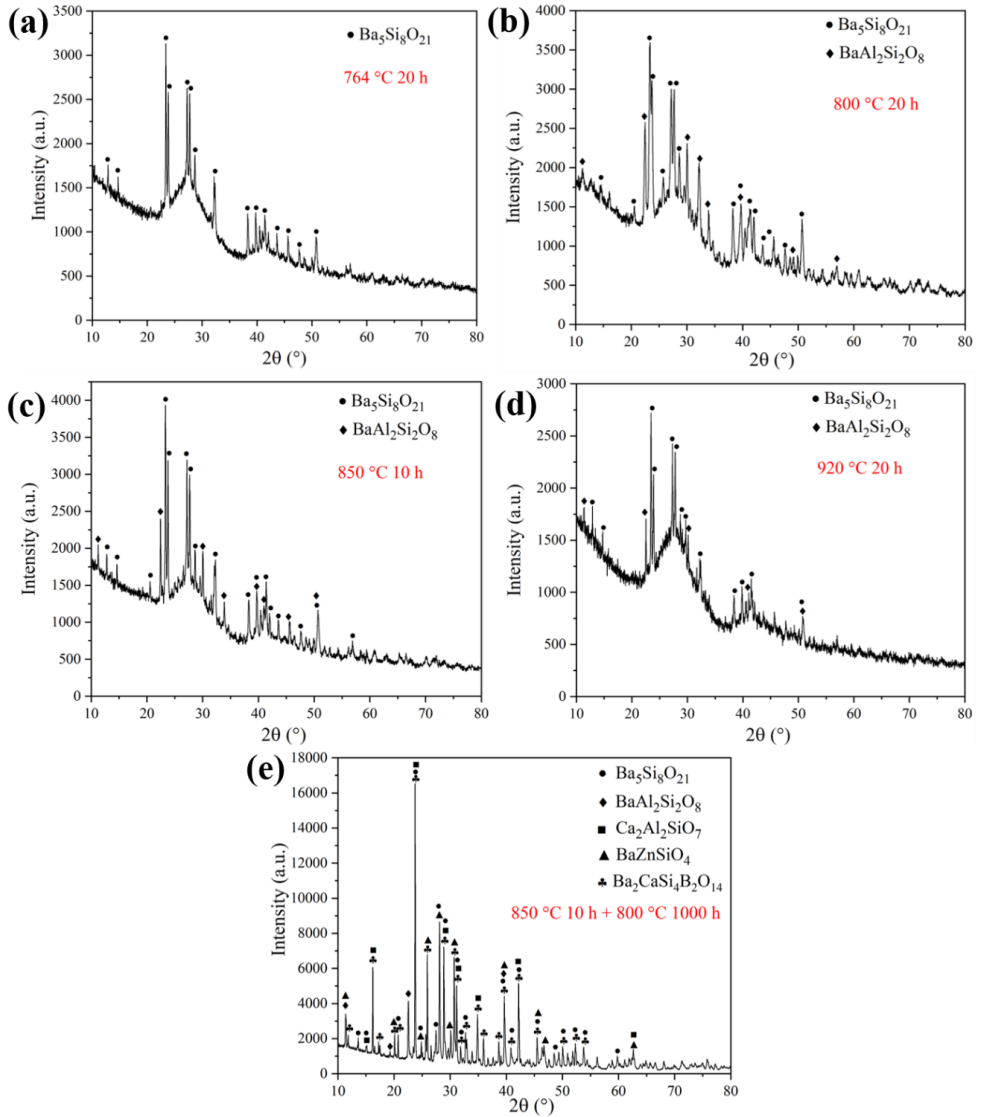
Fig. 4-4. Glass H after different heat-treatments for crystallization analysis, (a) XRD pattern of glass H after heating at 764 °C for 20 hours, (b) XRD pattern of glass H after heating at 800 °C for 20 hours, (c) XRD pattern of glass H after heating at 850 °C for 10 hours, (d) XRD pattern of glass H after heating at 920 °C for 20 hours, (e) XRD pattern of glass H after heat-treatment at 850 °C for 10 hours followed by 800 °C for 1000 hours, with same heating and cooling rate of 2 °C/min.

Table 4-1. Quantification of XRD results using Rietveld refinement

Samples	wt.% $Ba_5Si_8O_{21}$	wt.% $BaAl_2Si_2O_8$	wt.% $Ca_2Al_2SiO_7$	wt.% $BaZnSiO_4$	wt.% $Ba_2CaSi_4B_2O_{14}$	wt.% Amorphous
764 °C 20 h	2.3	-	-	-	-	97.7
800 °C 20 h	5.2	1.7	-	-	-	93.1
850 °C 10 h	3.1	0.8	-	-	-	96.1
920 °C 20 h	1.7	0.4	-	-	-	97.9
850 °C 10 h + 800 °C 1000 h	37	10.1	16.0	4.4	25.4	7.1

Thermodynamically stable phases were calculated by considering all possible reactions and phase equilibria by means of FactSage 8.1 (database FToxid for condensed phases and FactPS for the gas phase) as function of temperature at constant pressure 1 bar. The Gibbs energy is minimized in the simulation system. The chemical composition of glass H given in Table 3-2 was used as input for the calculations. Gas doesn't affect the equilibrium results as no stable gas phase was found below 1300 °C from the calculation. Figure 4-5 shows the amount of the stable phases with respect to temperature for the composition of glass H. The oxide liquid phase (slag) is calculated to form two separated liquids with the different compositions (immiscibility gap). These phases are called Slag#1 and Slag#2. Whereas, no slag phase separation was observed below 880 °C. Slag#2 shows a minor amount less than 1.8 wt.% (1.8 mol%) in glass H. $Ba_5Si_8O_{21}$ (CTE: 14.5×10^{-6} K^{-1} [79]) is the major phase from beginning of crystallization, which is in agreement with XRD analysis. $Ba_2Si_3O_8$ (CTE: 13.2×10^{-6} K^{-1} [79]) is possibly precipitated when heating above 890 °C, which shows a low fraction less than 7.8 wt.% (1.4 mol%). $BaSi_2O_5$ (12.9×10^{-6} K^{-1} [79]) was predicted to be existing below 740 °C (around T_r) with small amount at equilibria state without consideration of formation time. The FactSage calculations predict the existence of boron-containing $Ba_2CaB_6O_{12}$ below 890 °C. At higher temperature the major part of born is dissolved in the slag phases and the amount of gas is negligible by calculations. However, this phase does not fit to the XRD results. $Ba_2CaSi_4B_2O_{14}$ is precipitated after long term annealing, perhaps because the real heat treatment processes are difference with an ideal equilibrium state with minimum Gibbs energy, and Itsiite phase is not available in the database Ftox. Feld#1 means feldspar phase $BaAl_2Si_2O_8$ (7.5×10^{-6} K^{-1} [82]), which has a fraction less than 11 wt.% in weight (2.6 mol% per mole) formed below 800 °C according to the FactSage simulation. WOLLA refers to Wollastonite that is the solid solution mainly based on $CaSiO_3$ (CTE: 11.2×10^{-6} K^{-1} [81]) which mole fraction is calculated to be less than 7.1 wt.% (5.5 mol%). Mel-A is the abbreviation of Melilite solution $(Ca, Ba)_2(Zn, Al, B)(Al, B, Si)_2O_7$, which is supposed to be $Ca_2ZnSi_2O_7$ (CTE: 10.4×10^{-6} K^{-1} [81]) in the FactSage calculation, up to 6.3 wt.% (1.8 mol%). The phase Melilite-A was predicted to be stable 770-830 °C. $Ca_2Al_2SiO_7$ is formed in glass H from XRD detections, however, according to the present

calculations, this compound was only found 0.8 mol% in Mel-A phase by calculation due to incompleteness of the model for Melilite phase. Zn_2SiO_4 (CTE: 2.8×10^{-6} K^{-1} [81]) shows a low amount ≤ 5.3 wt.% (2.1 mol%) from beginning crystallization temperature to 1120 °C. Whereas, the compound $BaZnSiO_4$ cannot be found by FactSage calculations comparing with XRD results, since $BaO–ZnO–SiO_2$ is not available in the used database FTox. Two calcium vanadates were predicted and shows their amount less than 0.5 mol% (V_2O_5 addition amount). $Ca_2V_2O_7$ is a low-temperature phase which converts to $Ca_3V_2O_8$ phase around 770 °C. Due to the limitation of precision, XRD didn't detect any vanadate phase in the heat-treated samples.

In summary, the XRD results can be explained by FactSage results. Three main phases ($Ba_5Si_8O_{21}$, $BaAl_2Si_2O_8$ and $Ca_2Al_2SiO_7$) detected by XRD were precisely predicted by FactSage. Besides, crystalline behavior trend of glass H versus temperature could be predicted. FactSage simulations may provide a visual guidance for the development of new glass sealants, reduce the blindness of experiment and also give useful information for further study for the improvement for Glass H properties.
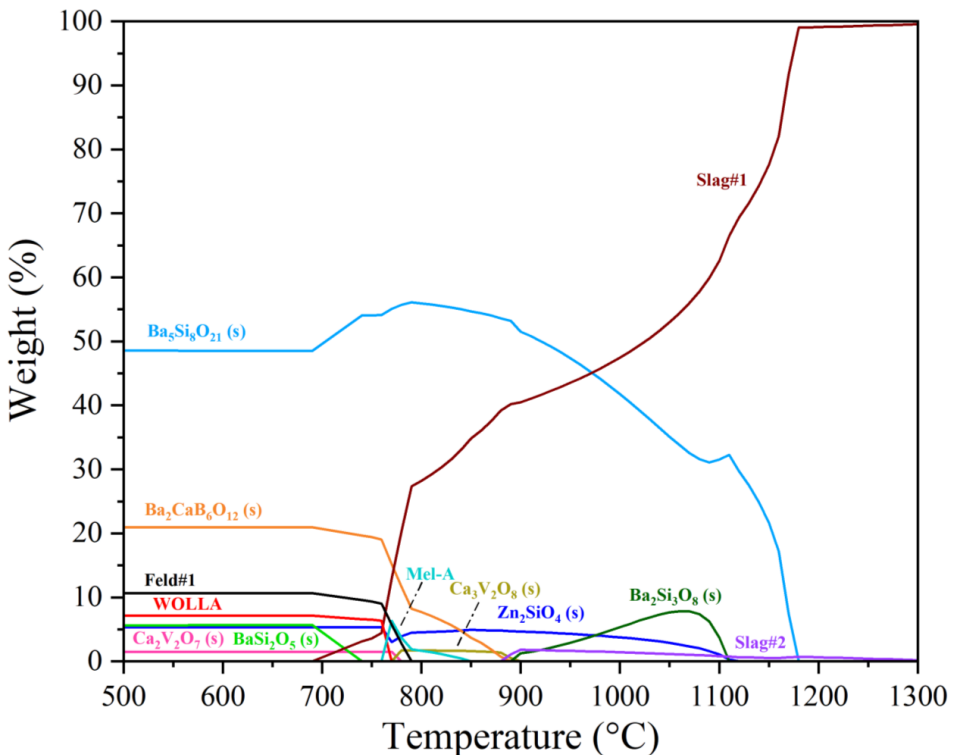
Fig. 4-5. Stable phases versus temperature by FactSage simulation for glass H

4.1.5 Summary of studies on glass matrix H

The parameter K_{gl} of glass H was calculated to be 0.49. Glass H has a good glass glass-forming tendency and great stability against crystallization. The dilatometry results show CTE of the sintered glass H between 8.5–$10.8 \times 10^{-6}\,K^{-1}$. The CTE of annealed samples decreased in comparison to the as sintered glass H. XRD results and FactSage simulation imply that low CTE phases hexacelsian $BaAl_2Si_2O_8$ and calcium aluminosilicate $Ca_2Al_2SiO_7$ formed in glass H is the main reason to cause decline of CTE. Boron-containing phases formed in glass H. Boron is dissolved in the slag and crystal phases, and the amount of gas is negligible by calculations. FactSage calculation is in high agreement with XRD analysis and FactSage simulations provides a visual guidance for the development of glass sealants.

4.2 Metal fillers and several membrane powders reinforced glass composite sealants

4.2.1 Fundamental idea of analyzed composite mixtures

Glass sealants are excellent candidates for high-temperature sealing and are widely used in the joining of solid oxide fuel cells (SOFCs). Glass "H" based on the $BaO–CaO–SiO_2$ system was investigated as a sealant matrix for joining OTMs because of its excellent viscosity, chemical compatibility, and joining properties demonstrated in SOFC applications [20]. The thermal expansion of glass H is lower (9.6×10^{-6} K^{-1}) compared to the membrane material STF25 (12×10^{-6} K^{-1}) and the support substrate Aluchrom (12.6×10^{-6} K^{-1}). Thermal expansion mismatch can lead to thermal stresses, and cracking and delamination of the samples and causes the module to leak gas. Adding filler materials of a higher thermal expansion coefficient to the glass matrix is a feasible strategy for improving the CTE of glass H in order to obtain matching thermal expansion coefficients with membrane and support metals. Gross et al. [20] studied 20 wt.% silver particles added to glass H and their sealant joined with Crofer22 APU for SOFC application, which exhibited good tensile strength and joining properties. Greven et al. [93] used 10-20 wt.% Ni, Ni-Cr, and CGO ($Ce_{0.8}Gd_{0.2}O_2$), respectively, as reinforcements for glass H to improve the mechanical properties. Schulze-Küppers et al. [12] investigated the perovskite STF-X series ($SrTi_{1-x}Fe_xO_{3-\delta}$), which can be used as an oxygen transport membrane. When STF fillers added to the glass H matrix, good compatibility with the other components of the OTM stack and suitable thermal expansion can be expected to this composite sealant. The CTE increases with the content of Fe, for example STF35 has a higher CTE (50–800°C) value of 13×10^{-6} K^{-1}, compared to that of STF25 (12×10^{-6} K^{-1}).

In this study, various filler materials with high CTE values, such as Ag, Ni, Ni-Cr (80-20), CGO, STF25, STF35, and Fe30Cr5Al0.5Y were added to glass H as the matrix of the composite material. These materials were chosen either for their plasticity, for example ductile metal particles such as Ag, Ni, and Ni-Cr (80-20), or for their compatibility with the other components of the OTM stack, such as perovskite OTM ceramic powders STF25, STF35, and CGO, or Fe30Cr5Al0.5Y with a similar composition to that of the sealing partner Aluchrom. Initial investigations into the compatibility of the glass H matrix mixed with various filler materials were carried out by sintering at the typical sealing temperature of 850 °C and SEM analysis on cross-sections. The thermal expansion properties of appropriate samples were measured using a dilatometer apparatus. The CTEs of as-sintered samples after sintering at 850 °C for 10 h were compared to samples after additional annealing at 800 °C for a 1000 h mimicking operation. In addition, the microstructures of annealed samples were investigated by scanning electron microscopy (SEM) and energy dispersive X-ray analysis spectroscopy (EDS). Finally, the composite mixture was blended with an organic binder solution to a sealant paste for application on the substrate by an x-y-dispensing robot. The gas tightness of the joined samples was examined by helium leak testing. The sealing performance of composites was evaluated by microstructural analysis with SEM together EDS on cross-sections of the samples.

4.2.2 Chemical compatibility

To test the chemical compatibility of different fillers (Ag, Ni, NiCr, FE, STF25, STF35, and CGO) with the glass matrix H, pellets of the composites were pressed and sintered at 850°C (an overview image of the obtained samples is presented in Fig. 4-6). The surfaces with the added Ag powder pellets were smooth after sintering at 850 °C. The HAg20 pellet exhibited viscous flow leading to a hemispherical-type sample, whereas increasing of Ag filler amount resulted in a hindered viscous flow during high-temperature sintering and the cylindrical contour of the pressed pellet remained unchanged. For composites with added Ni filler (20 wt.%, 30 wt.%), the pellets did not exhibit any viscous flowing compared with the Ag filler, and the diameter of the pellet with 20 wt.% Ni appeared to be smaller than the pellet with 30 wt.%. For composites mixed with the Ni-Cr (80-20) alloy powder, the HNC20 and HNC30 pellets exhibited viscous flow with a decreasing tendency, whereas cracks were observed on the surface of the HNC20 sample. Composite HNC30 had a glossy surface and no visible cracks. The HCGO20 pellet with 20 wt.% of CGO filler had a smooth and glossy surface after sintering. The metal powder Fe30Cr5Al0.5Y has a similar composition to the counterpart Aluchrom, which was purchased from Praxair company (product number: FE151). The sample HFE20 mixed with 20 wt.% Fe30Cr5Al0.5Y powder had a decent shrinkage in height and formed a foamy, open porous structure, which means it not suitable as a sealant filler for OTM application. The sample mixed with 20 wt.% Fe30Cr5Al0.5Y powder had a decent shrinkage in height but with a foamy, open porous structure, which means it not suitable as a sealant filler for OTM application, therefore, it was not investigated further. Adding 10 wt.% STF25 and STF35 to glass H led to numerous large pores and a sponge-like structure in the H10STF25 and H10STF35 samples after sintering.

Fig. 4-6. Composite pellets sintered at 850 °C for chemical compatibility investigation

Fig. 4-7 shows SEM micrographs of HAg20, HAg30, HAg40, HN20 and HN30 composites as sintered. In Fig. 4-7 (a-f), a homogeneous distribution of the Ag filler particles was observed in all HAg composites. The porosities of these composites were low due to the compaction of the Ag and glass during the viscous sintering process. EDS analysis was performed on the magnified SEM images. The glass matrix was partly crystallized during sintering as expected and several crystal phases formed from the glass H. The gray needle-like phase is a Ba/Al/Si feldspar, while binary Ba/Si phases can be seen as light gray blocks and darker blocks exhibit ternary silicate phases consisting of Ca/Ba/Si. The light-gray elliptical sphere is a silver filler. All three composite compositions with Ag qualify as a sealing material and, which is why dilatometer tests were carried out (cf. section 4.2.3).

HN20 and HN30 exhibit more and larger pores compared to the HAg composites, as can be seen in the magnified SEM images in Fig. 4-7 (g - j). The pores of HN20 are round, whereas the pores of HN30 are irregular in shape. With a decreasing amount of glass phase, the glass is insufficient to cover all Ni particles and prevent oxidization. Consequently, the open surface of the Ni grains increased, which raised the likelihood of Ni grain oxidation during sintering, and NiO oxidation forms in HN30 (NiO: 13.5×10^{-6} K^{-1} [141]) as shown in Fig. 5-2 (j). The composite with lower percentage of Ni (HN20) did not exhibit significant oxidation of the Ni particles (Fig. 4-7 h), but cracks grew along the $BaO \cdot Al_2O_3 \cdot 2SiO_2$ acicular phase which was formed from glass H during sintering. This phase has a lower CTE of around $2.3\text{-}7.8 \times 10^{-6}$ /K compared to the one of the glass H matrix (9.6×10^{-6} K^{-1} [109]). No crack was formed in the Ni 30 wt.% sample, whereas some crystal phases were formed from HN30, such as the Ba-Zn-silicate phase, the barium feldspar phase, and Ba/V/Si. No joining tests were performed for HN20 and HN30 due to the cracks/porosity of the seals and the oxidation phenomena, respectively.

Fig. 4-8 shows SEM micrographs of the HNC20, HNC30, HCGO20, H10STF25, and H10STF35 composites as sintered. A large number of irregular pores occurred in the HNC20 composite (Fig. 4-8 a). EDS mapping analysis revealed that Ni-Cr particles were oxidized after sintering, as shown in Fig. 4-9, and the oxidized coating layer is Cr_2O_3, which has an average CTE value of 6.5×10^{-6} K^{-1} [142]. Composite HNC30 has a lower porosity and homogeneous filler distribution microstructure compared with HNC20, as shown in Fig. 4-8 (c-d). HNC30 is considered to be an adequate joining material for OTM applications. For the HCGO20 composite, numerous large pores were observed compared to HAg20 (Fig 4-8 e), with the pores being evenly distributed in the composite. No interaction between the CGO filler and glass H was observed. However, some agglomerations of the CGO particles were found (Fig. 4-8 f).

For composites with added 10 wt.% STF25 and STF35, numerous large pores and a sponge-like structure formed after sintering at 850 °C, as shown in Fig. 4-8 (g-j), which evidently disqualify these composites due to possible gas leakage as well as the expectation of low strength of the joint. Here STF25 and STF35 powders were products after calcination at 1100 °C for 5 hours, whereas STF25 wafers used for joining with Aluchrom were pressed from the calcined powders and then sintered at 1400 °C for 5 hours in a second thermal treatment. The specific surface area of dense

wafer and powder is different. Generally speaking, powder has a larger specific surface area to get larger volume ratio connected glass. STF ceramic powders release probably oxygen during heating, as seen from the thermogravimetric analysis in Fig. 4-10. The glass matrix is softened and has a certain viscous fluidity at heating, which wraps the ceramic STF particles, and the released oxygen cannot escape, which causes the expansion of the pellet. The main reasons of the porous, spongy structure of the STF mixed composite samples are from STF particle large specific surface and oxygen release during heating. Anyway, it's already evident that STF25 and STF35 are not suitable filler material to optimize glass H sealant. Some agglomerations formed in the H10STF25 sample. A thin interdiffusion layer was found between the STF25 and the glass matrix, which formed a possible interdiffusion layer with Ba/Sr/Ti/Si elements as analyzed by EDS software TruMap (developed by Oxford) as seen in Fig. 4-11. No pores formed near this interdiffusion layer. Such limited interaction is appreciable for sealing because a strong connection might be realized without destroying the membrane sample. The interdiffusion with OTM wafer is discussed more in detail in joining behavior part of section 4.2.5.

In summary, six composites, i.e., HAg20, HAg30, HAg40, HN30, HNC30, and HCGO20, showed moderate porosity and good chemical compatibility with glass H and were therefore chosen for further investigation.
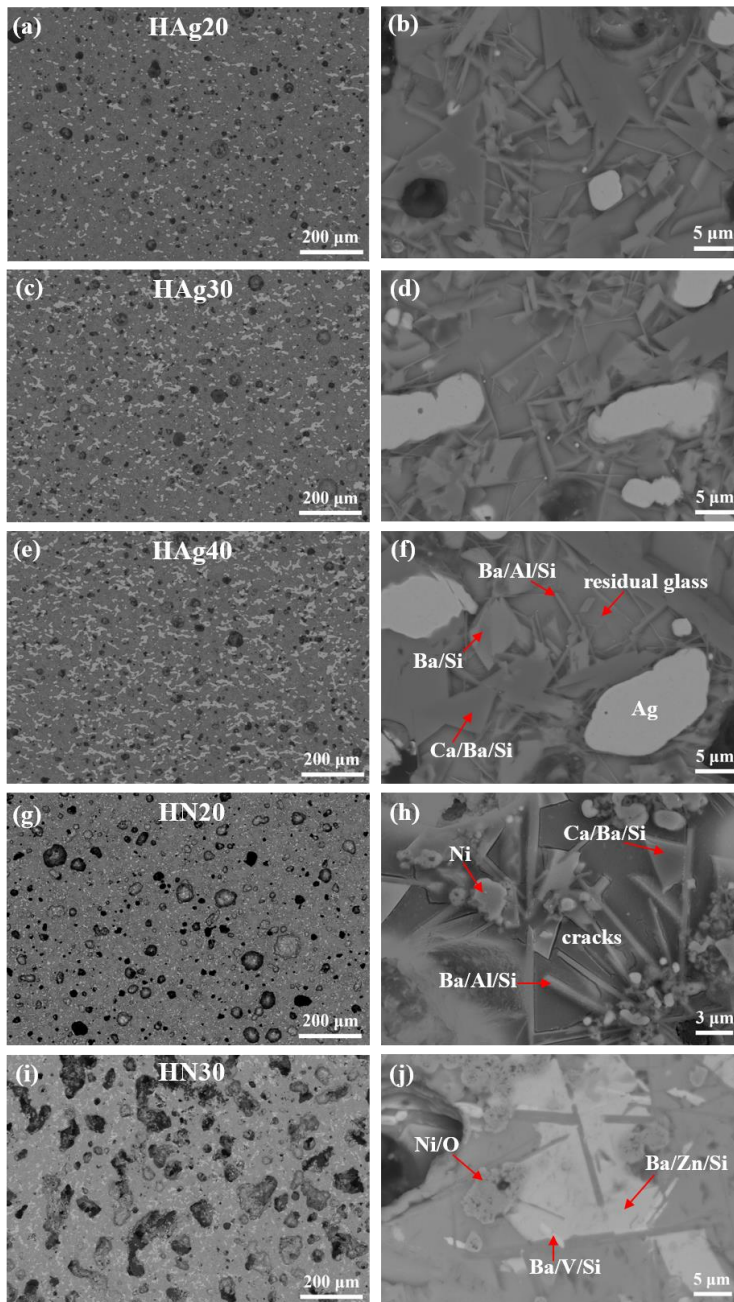
Fig. 4-7. SEM micrographs of composites as joined: (a, b) HAg20, (c, d) HAg30, (e, f) HAg40, (g, h) HN20, (I, j) HN30; overview on the left and magnification on the right
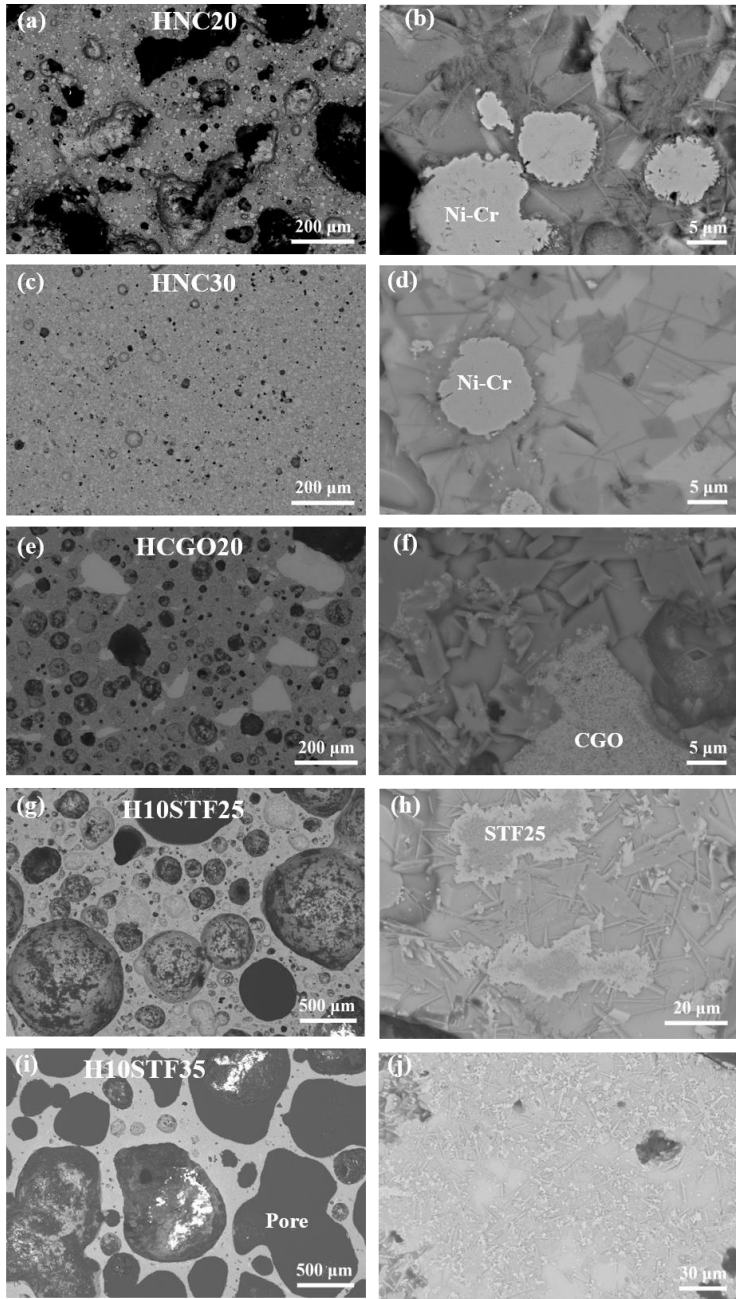
Fig. 4-8. SEM micrographs of composites as joined: (a, b) HNC20, (c, d) HNC30, (e, f) HCGO20, (g, h) H10STF25, (i, j) H10STF35; overview on the left and magnification on the right
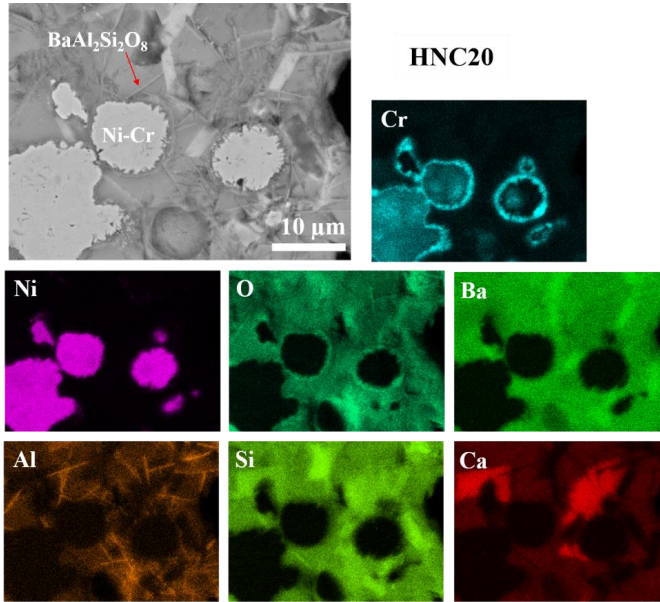
Fig. 4-9. SEM-EDS maps of the HNC20 sample
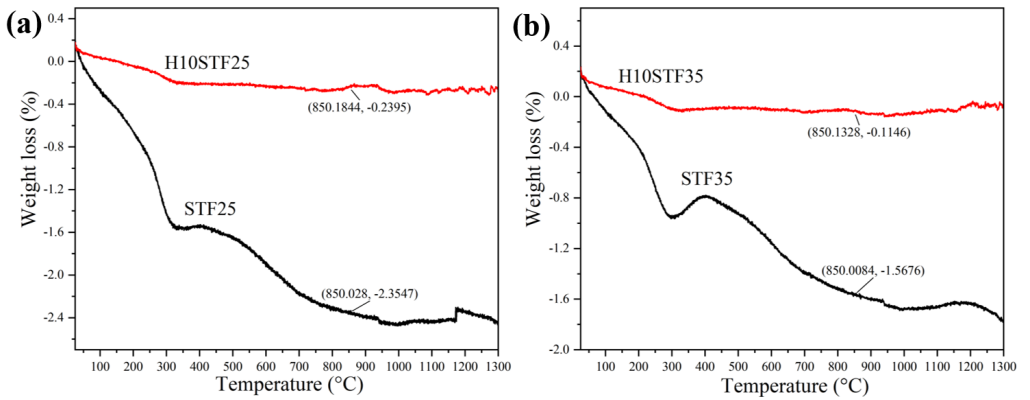
Fig. 4-10. Weight loss curves of STF fillers and mixed with glass H
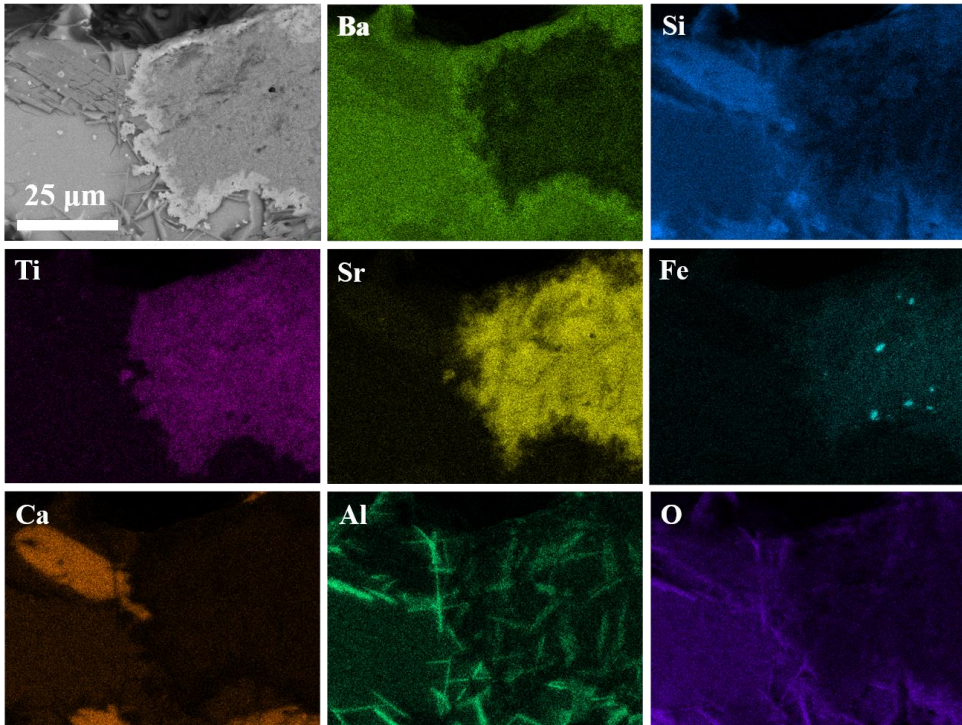
Fig. 4-11. SEM-EDS maps of the H10STF25

4.2.3 Thermal expansion

Dilatometer measurements were carried out for the STF25 membrane, Aluchrom, and the HAg20, HAg30, HAg40, HN30, HNC30 and HCGO20 composites. The dilatometer bars of composites were pressed and sintered at 850 °C for 10 h. Some of the bars were additionally annealed at 800 °C for 1000 h. The thermal dilatometric results of the sintered and annealed composites are presented in Fig. 4-12. The CTE curves of the sintered composites with Ag fillers (Fig. 4-12 a) have shown a transformation temperature (T_g) of 565 °C for the residual glass phase of the material. Depending on the different filler materials and filler amounts, the T_g value shifted from 565 °C to 630 °C in the CTE curves, as seen in Table 4-2. The aged samples of the composites exhibited highly ceramic behavior of the material. There is no noticeable T_g point in the dilatometer curves of the annealed samples HAg20A, HAg30A, HAg40A, HN30A, and HNC30A. Only for the annealed sample HCGO20A, one can see that there is a slightly obvious glass transition zone between 530 °C and 630 °C in the dilatometer curve of Fig. 4-12 (c) and T_g is measured around 590 °C. For this sample, the residual glass phase still exists and can be assumed to be at the grain boundaries of the crystallized glass-ceramic sealants. Whereas after a long term of ageing, the amount of the residual

glass phase is very low for all the other samples. The analysis by SEM-EDS have shown that differentiation of the residual glass phase and crystals becomes impossible.

The CTE values of the annealed samples decreased after 1000 h annealing compared to the as-sintered samples. This finding probably is due to a phase formed with lower CTE compared to the glass H. In addition, CTE curves of the samples with different Ag amounts before annealing were similar, whereas after annealing the CTE improved with increasing Ag content, as shown in Fig. 4-12 (a). The addition of 40 wt.% Ag resulted in the highest CTE values of up to $12.4 \times 10^{-6}\,\text{K}^{-1}$ as-sintered sample and $10.3 \times 10^{-6}\,\text{K}^{-1}$ after annealing, respectively, measured in a temperature range between 200 °C and 850 °C (see Table 5-1). Fig. 4-12 (b) shows CTE plots of composites with Ni, Ni-Cr (80-20), and CGO fillers. The highest CTE is the composite with 30 wt.% Ni, which is up to $12.9 \times 10^{-6}\,\text{K}^{-1}$ in the sintered sample and $10.4 \times 10^{-6}\,\text{K}^{-1}$ after annealing. The 30 wt.% Ni-Cr composite has a mean CTE value of around $10.5 \times 10^{-6}\,\text{K}^{-1}$ in the sintered sample and $9.6 \times 10^{-6}\,\text{K}^{-1}$ after annealing. The lowest CTE value is the composite with 20 wt.% CGO.
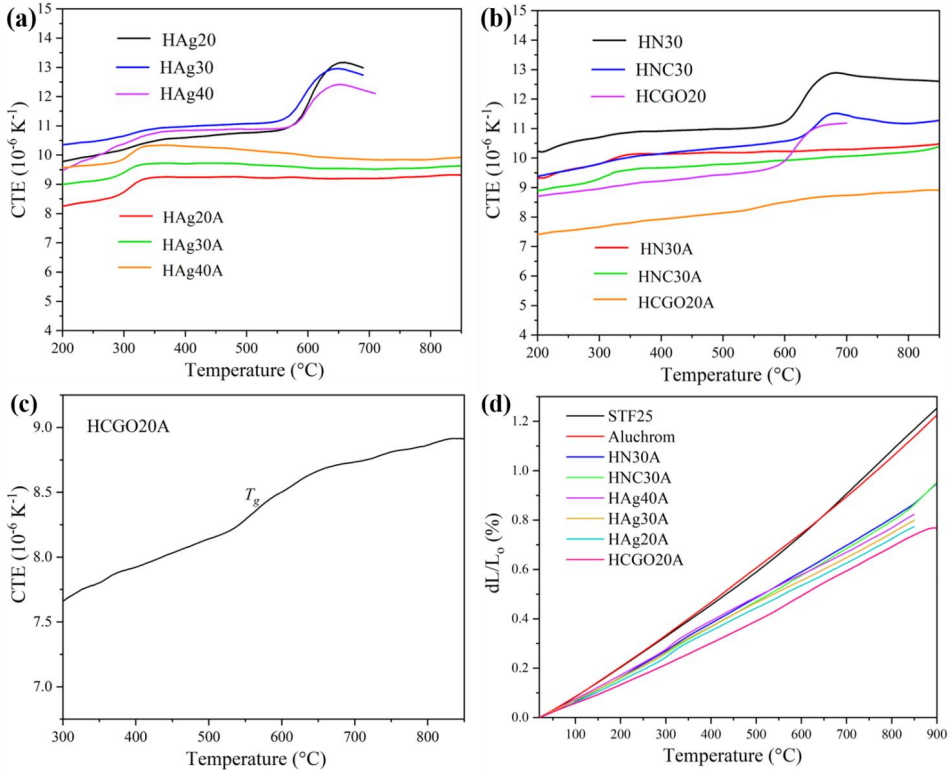
Fig. 4-12. CTE curves for composites samples sintered and annealed: (a) samples with different Ag amounts, (b) compared with different fillers Ni, Ni-Cr (80-20), and CGO samples. (c) CTE curve of annealing sample HCGO20A. (d) Elongation curves after annealing composite samples compared with STF25 and Aluchrom

Table 4-2. Thermal expansion coefficient (as-sintered and long term-annealed) of the composites

| Composite | T_g (°C) | CTE [×10⁻⁶ K⁻¹] (200 – 850°C) | |
		Sintered: 850 °C – 10h	Annealed: 850 °C – 10h → 800 °C – 1000h
HAg20	565	9.8 – 13.2	8.3 – 9.2
HAg30	565	10.4 – 12.9	9.0 – 9.7
HAg40	565	9.6 – 12.4	9.6 – 10.3
HN30	600	10.2 – 12.9	9.4 – 10.4
HNC30	630	9.4 – 11.5	8.9 – 10.3
HCGO20	590	8.7 – 11.2	7.4 – 8.9

In addition, the thermal expansion behaviors of the oxygen transport membrane material STF25 and the steel housing material Aluchrom were also measured between 200 °C and 850 °C (Figure 4-12 d). With increasing temperature, the elongation of these samples also increases. The dL_{rel} curves of STF25 and Aluchrom are very similar as intended, which explains why Aluchrom was chosen as the joining partner for the OTM module design. The CTE values range from 10.7 to 13.3 × 10⁻⁶ K⁻¹ and from 11.5 to 13.7 × 10⁻⁶ K⁻¹ for STF25 and Aluchrom, respectively (Table 5-1). The sealant candidate materials with an expansion behavior closest to STF25 and Aluchrom are HN30A, HNC30A, and HAg40A from the elongation curves.

In order to investigate the reason why CTE values decreased after annealing, SEM and EDS analyses were performed to verify which low CTE phases were formed. Fig. 4-13 shows a series of micrographs and EDS analyses for HAg20A, HAg40A, HN30A, and HNC30A. The needle-like phase barium feldspar ($BaO \cdot Al_2O_3 \cdot 2SiO_2$) can be found in the higher magnification images of all three compositions. It can be assumed that the volume and quantity of this crystal increase to the equilibrium state of the glass composites system after heat treatment. $BaAl_2Si_2O_8$ has two common phases: a monoclinic Celsian low temperature phase with a CTE of around 3 × 10⁻⁶ K⁻¹ [95] and a Hexacelsian high-temperature phase with a CTE of 7.5 × 10⁻⁶ K⁻¹ [82]. Brendt [94] reported that these two phases formed from glass H after heat treatment at 850 °C analysed by XRD. Some studies [77, 96, 97] also demonstrated that $BaAl_2Si_2O_8$ phases easily crystallize out in barium–calcium aluminosilicate system glasses during heating process. Neither of the barium feldspar phases is able to reach CTE value higher than the matrix glass H. The light-gray block phase should include Ba/Zn/Si elements via EDS analysis which is formed from glass H, and a possible phase composition might be $Ba_2ZnSi_2O_7$ by EDS analysis. Kerstan et al. [140] carried out dilatometer

measurements on the BZS phases and reported a CTE of 10.4×10^{-6} K^{-1} for the Ba$_2$ZnSi$_2$O$_7$ phase. HN30A still had many large pores after 1000 h annealing, and the Ni particles were oxidized (Fig. 4-13 e, f). Therefore, the material was disregarded from further joining tests. Ni-Cr grains were also oxidized and can be seen in the high magnification image of HNC30A (Fig. 4-13 h). Cr$_2$O$_3$ has a relatively low CTE of 6.4×10^{-6} K^{-1} [142]. Nevertheless, the microstructure of HNC30A has a low porosity and exhibited a homogeneous filler distribution. The decrease in CTE of the annealed samples is attributed to the formation of low CTE phases, such as, barium feldspar and the CrO phase. The effect of decreasing CTE values after long term annealing can be explained by the increase of low CTE phases with the annealing time.

To minimize mechanical stress from thermal mismatch, the CTE of the composite sealants should be similar to that of the materials to be sealed. Considering the thermal expansion behavior and post-test SEM-EDS analyses of the composites, HAg40 and HNC30 were chosen for sealing tests.
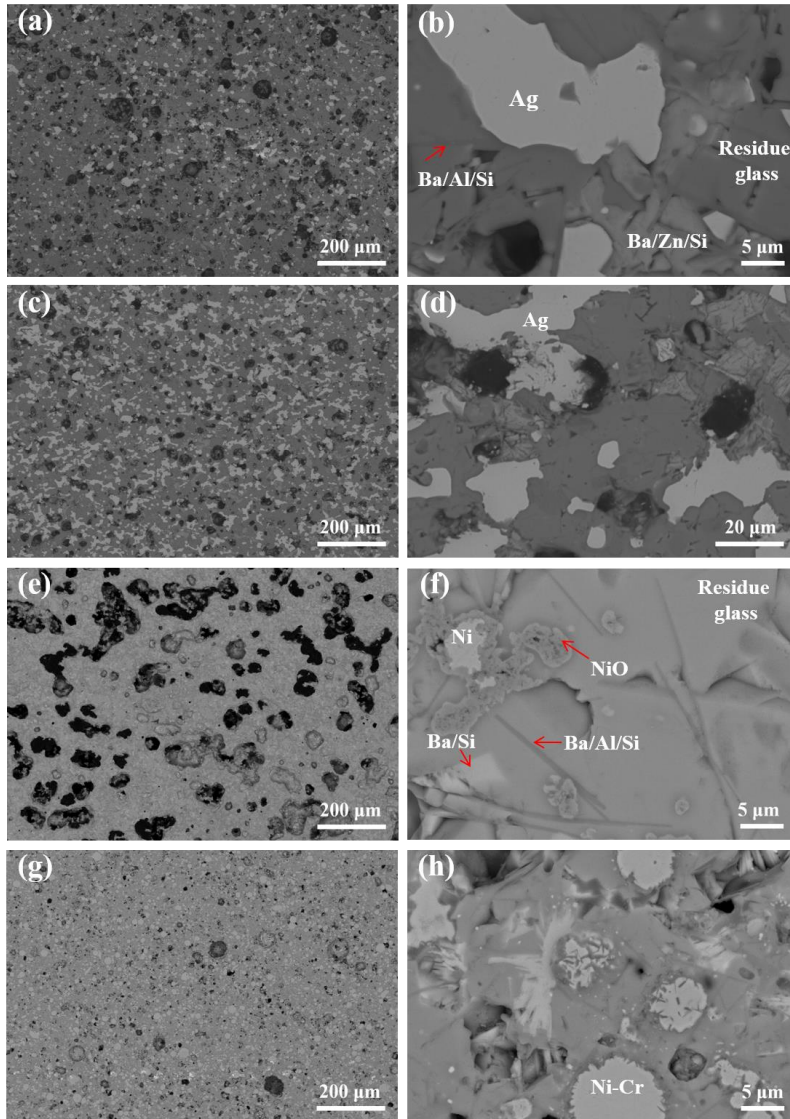
Fig. 4-13. SEM-EDS analyses for annealing composites (a, b) HAg20A, (c, d) HAg40A, (e, f) HN30A, (g, h) HNC30A; overview on the left and magnification on the right

4.2.4 Shrinkage behavior of metal filler reinforced sealants

Sinking dilatometric measurements simulated the stack joining conditions and observed the shrinkage behavior of HAg40 and HNC30 glass-based sealants in between two steel plates under a constant pressure of 10 KPa. Fig. 4-14 shows the shrinking behavior for two sealant HAg40 and HNC30. Onset shrinking temperature (T_a), end shrinking temperature (T_b) and maximum shrinkage rate of the two sealants were listed in Table 4-3. HAg40 glass-based sealant got a sharp shrinkage process from T_a 643 °C to T_b 747 °C. Below 643 °C, HAg40 only had slightly shrinkage less than 3%. Then the shrinkage curve of HAg40 kept constant after T_b until the end of measurement. HAg40 exhibited the relatively high shrinkage rate around 40% comparing with HNC30 33%. Gross. et.al. reported pure glass H showed a 39% shrinkage rate and glass H reinforced with 13% ZrO_2 received 43% shrinkage rate [109].
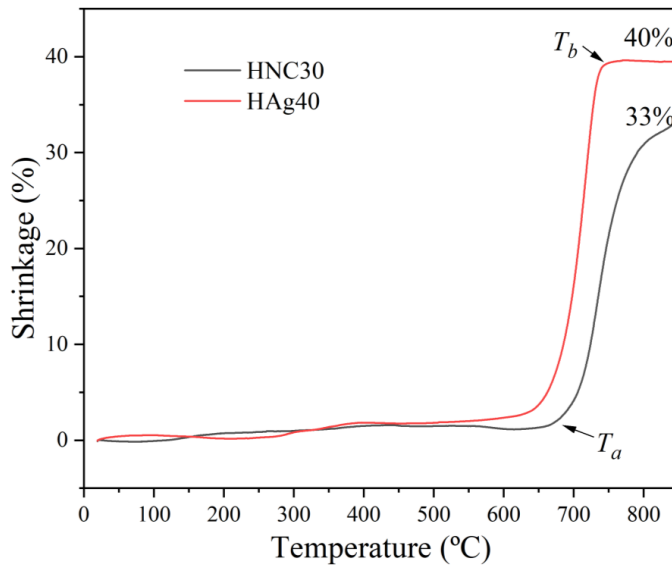
Fig. 4-14. Sinking dilatometer of HAg40 and HNC30

Table 4-3. Onset shrinking temperature T_a, shrinking end temperature T_b and shrinkage rate at 850 °C

Sample	T_a (°C)	T_b (°C)	Shrinkage 850 °C
HAg40	643	747	40%
HNC30	670	808	33%

4.2.5 Joining behavior of metal filler reinforced sealants joining at 850 °C

4.2.5.1 Gas tightness

As reported above, HAg40 and HNC30 were selected for sealing tests. Two types of sample designs were prepared to investigate sealing behavior. One sandwiched type used two square steel plates joined together by glass-composite sealants for a gas-tightness test. The steel parts used in this study were as-delivered Aluchrom and pre-oxidized Aluchrom. Another sandwiched type was designed with a STF25/glass-composite sealant/steel plate in asymmetric geometry. Aluchrom and pre-oxidized Aluchrom were again chosen as the counterpart.

The gas-tightness values for the sandwiched samples sealed by HAg40 and HNC30 are summarized in Table 4-4. The samples sealed with the HAg40 glass composite showed low helium leakage values that were lower than the detection limit of 10^{-9} mbar·l·s^{-1}. The sandwiched structures sealed with HNC30 and as-received Aluchrom heated at 850 °C for 10 h also showed excellent gas tightness, i.e., leakage smaller than 10^{-9} mbar·l·s^{-1}. Only two sandwiched samples of HNC30 with pre-oxidized Aluchrom have shown slightly higher leakage rate values of the magnitude 10^{-7} mbar·l·s^{-1} and 2.5×10^{-6} mbar·l·s^{-1}. According to the indications of Mahapatra et al., the sealant material with a gas leakage rate of lower than 10^{-7} mbar·l·s^{-1} would fulfill the requirements for the high temperature operation of the OTM module [143]. Pre-oxidation heat treatment of Aluchrom at 1250 °C for 5 h did not generate much of a beneficial effect on the gas-tightness test sealed by the HNC30 sealant. In order to explore the reasons for the decreased gas tightness, an ink penetration test was performed for pre-Aluchrom/HNC30/pre-Aluchrom samples; the results of the broken samples are presented in Fig. 4-15. No penetration of the red ink into the sealed part was observed, which means that no defect was detected in the sealant. Moreover, no delamination of the metal/sealant interface was visible. The HNC30 sealant has good adherence to pre-Aluchrom. The relatively rough surface of pre-oxidized Aluchrom is one possible reason for the slightly decreased gas tightness.

Table 4-4. Gas tightness tests for sandwich samples sealed with HAg40 and HNC30

Sealant	Substrate	Gas tightness mbar·l·s^{-1}	Sealant	Substrate	Gas tightness mbar·l·s^{-1}
HAg40	Aluchrom	$<10^{-9}$	HNC30	Aluchrom	$<10^{-9}$
HAg40	Pre-oxidized Aluchrom	$<10^{-9}$	HNC30	Pre-oxidized Aluchrom	$10^{-7}/2.5\times10^{-6}$
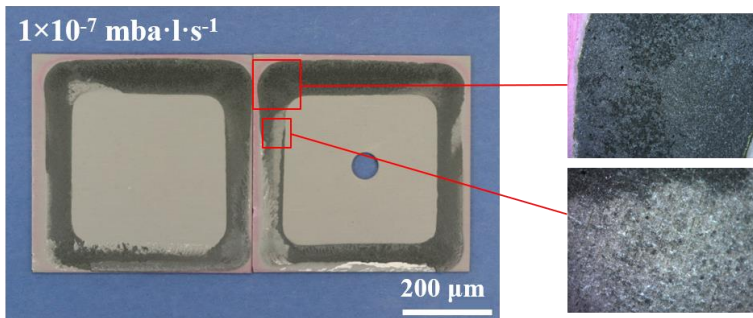
Fig. 4-15. Ink penetration test for sandwich sample (pre-oxidized Aluchrom plates sealed with HNC30); overview on the left and magnification on the right

4.2.5.2 Microstructure of assembled joints

SEM images of the cross-sections of the sealed membrane STF25 and metal substrates (Aluchrom and pre-oxidized Aluchrom) using HAg40 and HNC30 are shown in Fig. 4-16 and Fig. 4-17, respectively. In average, the obtained sealant layer of HAg40 had a thickness of 330 μm. The average thickness of the dispensed green layer of HAg40 was 0.8 mm, resulting in a shrinkage of 59%. The HNC30 sealant had a thickness of 400 μm from the green layer being 0.9 mm thick, resulting in a similar shrinkage of 56%. The organic binder in the sealant foil was decomposed from the sealants layer and the sealants were well compacted during sintering. The porosity of the HAg40 and HNC30 sealants was low and evenly distributed, i.e. no pore agglomeration occurred, which would otherwise lead to a high risk of leakage and mechanical failure. The metallic filler particles Ag and Ni-Cr were both evenly distributed in the HAg40 and HNC30 sealants, respectively. The two sealants exhibited good adhesion to the STF25 membrane as well as to the Aluchrom plate and pre-oxidized Aluchrom. No crack formation or delamination was observed at either of the joint parts or sealants.

With a higher magnification of the SEM, it was possible to analyze the microstructure of the glass sealant and joints more in detail, revealing that there was a continuous chemical bonding layer between the glass H matrix and the STF25 membrane (Fig. 4-16 b, e) with a thickness of 0.4-0.8 µm, and a transitional zone thin boundary layer appearing in light gray. The transitional layer alters the interface bonding characteristics of the membrane and the glass sealant. Inter-diffusion at the interface of the sealing glass and the interconnected ceramic membrane STF25 could not be avoidable during sintering or application and their atoms formed covalent bonds, which prevented delamination in the transitional zone, rather than weak bonding via van der Waals forces. Therefore, a certain diffusion distance is desirable. The diffusion between glass H and STF25 did not cause any pores, delamination, or cracks. Some studies [144] also demonstrated that the formation of a thin interaction layer between the ceramic and glass causes a strong chemical bond by forming an intermediate compound, indicating that it further increases the joining strength between the glass composite sealants and the STF25 membrane. Further measurements such as wavelength-dispersive X-ray spectroscopy (WDS) mapping or atom probe tomography (APT) analysis needs to be carried out to investigate the transitional zone more in detail.

Interfaces between the metal substrates and the glass composite sealants HAg40 and HNC30 are shown in Fig. 4-16 (c, f) and Fig. 4-17 (b, d), respectively. Comparing them, it is clear that the surface roughness of the pre-oxidized Aluchrom is much higher and the thickness of the scale is much thicker. Both samples display good adherence between the glass sealant and support metals. For the Aluchrom plate, a continuous thin oxidation layer with a thickness of around 0.25 µm connecting the glass composite seal and Aluchrom alloy was detected after the sealing process from the SEM images (Fig. 4-16 c, Fig. 4-17 b). From the HNC30 sealant to the Aluchrom line scan in Fig. 4-18 (a), Ba and Si lines declined sharply at the interface, whereas the Fe and Cr lines increased sharply. The Al and O elements lines stood out, but due to the narrow thickness of the interface it is still hard to conclude whether it is pure alumina or some other elements diffused into it. The thin scale layer improves the wetting and bonding of glass on Aluchrom steel. The oxidation layer of pre-oxidized Aluchrom (1250 °C, 5 h) had a thickness of around 2 µm, as can be seen in Fig. 4-16 (f) and Fig. 4-17 (d), which is shown to be pure Al_2O_3 according to the line scan in Fig. 4-18 (b) and is in good agreement with the literature [145]. The needle-like $BaAl_2Si_2O_8$ phase growing close to the Al_2O_3 scale reveals strong chemical bonds formed between the Al_2O_3 scale and the glass-composites. Some studies also demonstrated that an Al_2O_3 coating on ferritic steel improves the interfacial bonding with glass [19, 144]. The oxidation layer of Aluchrom is required to increase the chemical stability of the module parts under the atmospheric operation conditions.

In summary, the joining performance of pre-oxidized Aluchrom joined with both glass sealants is very promising. The oxide scale Al_2O_3 of Aluchrom formed ionic bonds with the glass sealant during sintering, which is expected to enhance the strength of the joints in a future OTM module. However, the resulting seal will only be reliable in the long-term operation if the oxide layer is well bonded to the metal substrate. If the Al_2O_3 scale is too thick, this will cause Al depletion in the Aluchrom part [146] and might result in failure. Future studies therefore need to investigate the impact of the oxide scale on the oxidized Aluchrom used for the OTM more in detail.
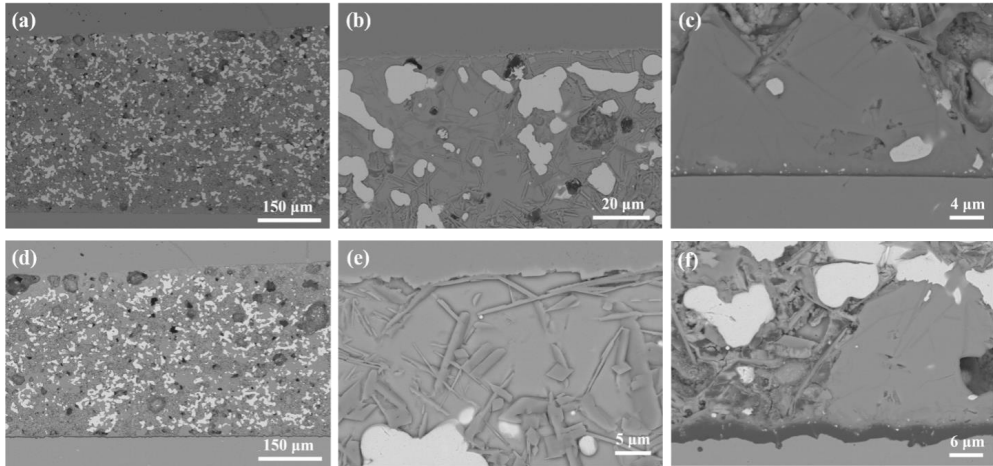
Fig. 4-16. Joints STF25/HAg40/Aluchrom (a-c) and STF25/HAg40/pre-Aluchrom (d-e); both joints sealed at 850 °C with a 400 g dead load
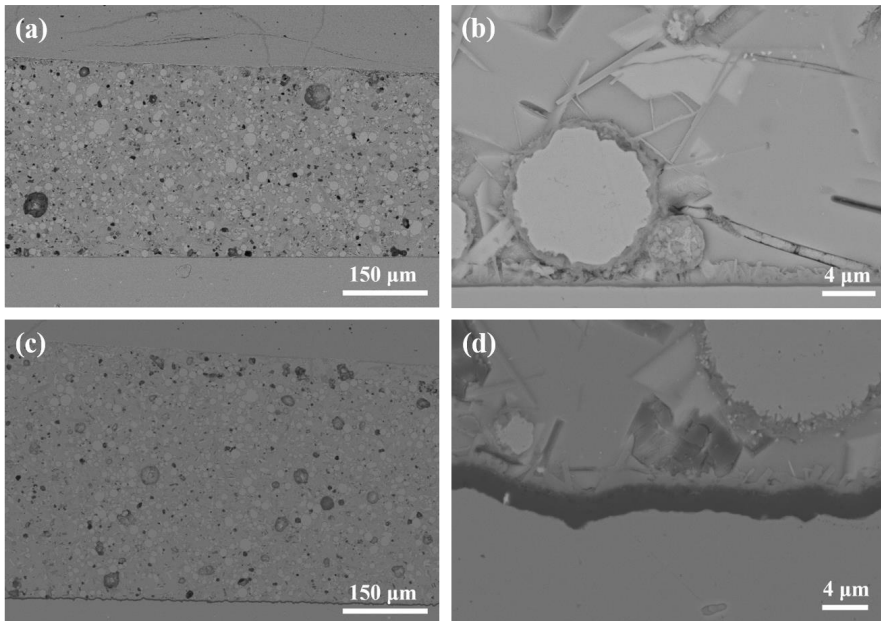
Fig. 4-17. Joints STF25/HNC30/Aluchrom (a-b) and STF25/HNC30/pre-Aluchrom (c-d); both joints sealed at 850 °C with a 400 g dead load
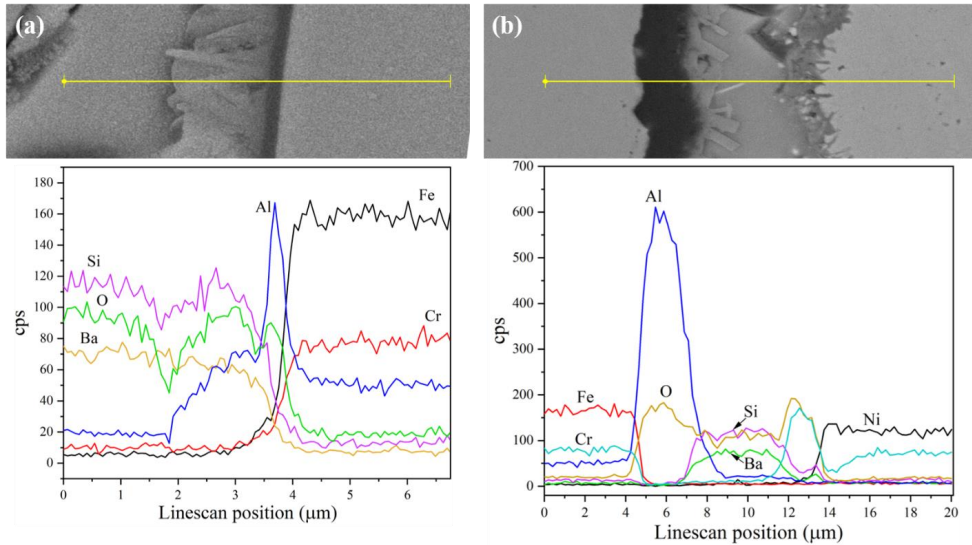
Fig. 4-18. Line scans through the interface between HNC30 and Aluchrom (a), HNC30 and pre-Aluchrom (b)

4.2.6 Mechanical strength measurement of metal filler reinforced sealants

Mechanical shear strengths of two sealants HAg40 and HNC30 were measured by torsion test on the hourglass-shaped samples at room temperature. Stress values were then calculated on the basis of equations (3.4) and (3.5). The torsion specimens were joined at 850 °C for 10 h. The average shear stress of HAg40 was tested to 62.2 ± 2.8 MPa. Whereas HNC30 exhibited a lower median shear stress around 28.8 ± 1.6 MPa comparing with HAg40 specimen. Hasanabad et. al. reported the composite sealant glass H reinforced with 13 wt.% yttrium stabilized zirconium oxide (YSZ) fibers achieved average shear strength around 58.0 MPa [125] in same testing machine. Comparing to the YSZ reinforced glass composite, HAg40 sealant shows a better mechanical strength. Fig. 4-19 shows the broken surfaces of the components after torsion tests. Fracture occurred between the steel and the glass sealants, leaving a shining metal surface. On the other hand, glass sealants protected the metal Crofer22H from oxidation, if compared to the area not covered by glass sealant. HAg40 sealant shows a dense structure. The residues of HNC30 sealant are formed in a porous, sponge-like structure, especially near outer part of the sealant ring, which was assumed to be caused by oxidization of the filler Ni-Cr.
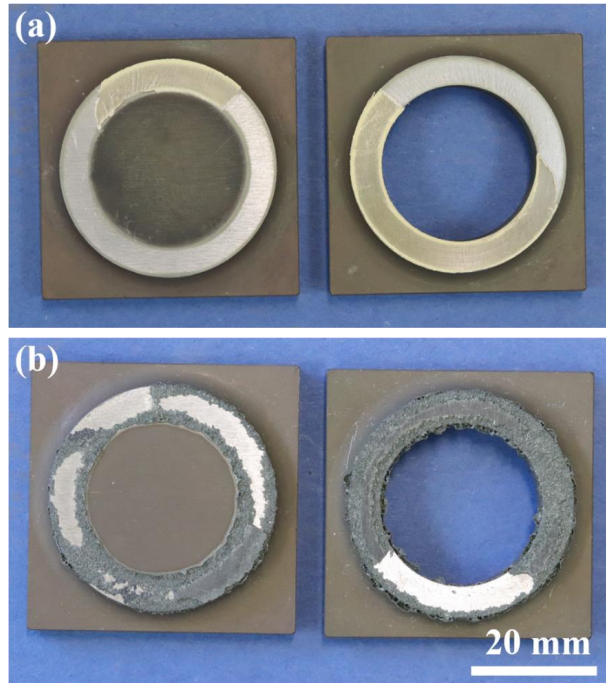
Fig. 4-19. Photograph of fracture surfaces after torsion tests at room temperature for HAg40 (a) and HNC30 (b) glass composite sealants

In order to investigate the microstructure of the sealants, SEM and EDS analyses were performed for HAg40 and HNC30 sealed torsion samples. Fig. 4-20 shows SEM images of cross sections of HAg40 (a, b) and HNC30 (c-e) samples after torsion tests. HAg40 exhibited homogenous and less porous structure. HAg40 sealant was squeezed out small amount under heavy dead load (around 4 Kg). There is no crack or delamination in the interface between Crofer22H and the two sealants, HAg40 and HNC30. Some filler Ni-Cr particles are oxidized after 850 °C joining and surrounded by an oxide layer visibly from Fig. 4-20 (e). From the line scanning in Fig. 4-21 one can see the oxidized coating layer should be Cr_2O_3. No oxidation could be observed for Ag filler from line scanning shown in Fig. 4-22 (a). A black thin chromium oxide layer is formed on the surface of Crofer22H, which is thermodynamically very stable. The white dots are the laves phase already reported by Bongiorno et al. [147]. Laves phases are gathered at grain boundaries of Crofer22H and consist of Nb/Si as visible in line scanning of Fig. 4-22 (b).
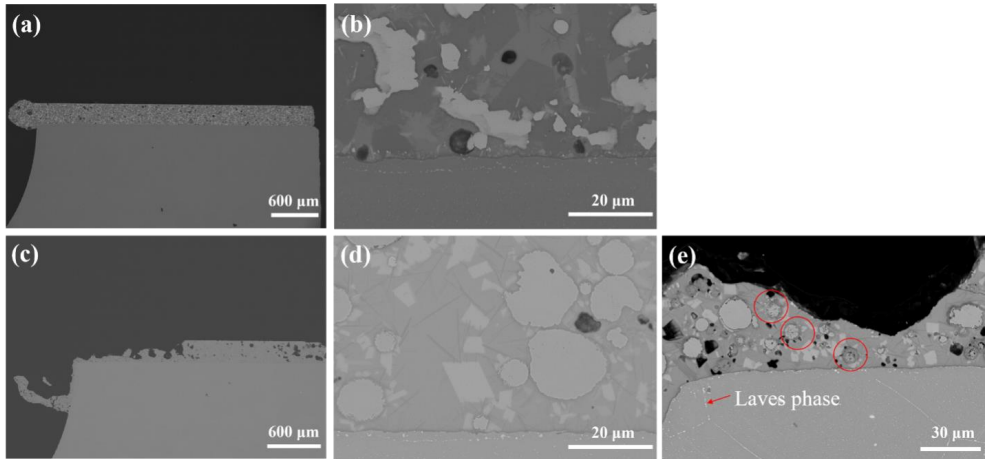
Fig. 4-20. SEM images of cross sections of HAg40 (a, b) and HNC30 (c-e) samples after torsion tests, overview on the left and magnification on the right
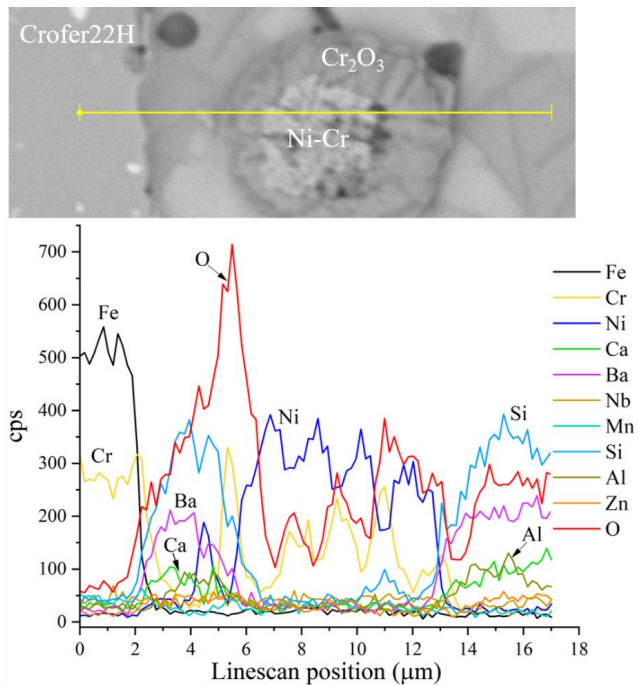
Fig. 4-21. Line scan through the filler Ni-Cr at the sample Crofer22H/HNC30
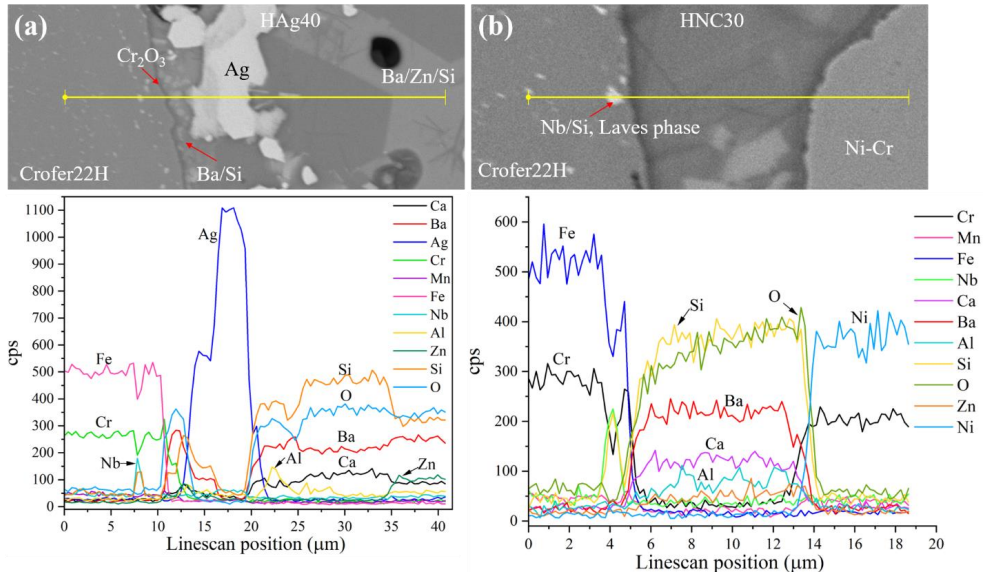
Fig. 4-22. Line scans through the interfaces between (a) HAg40 and Crofer22H, (b) HNC30 and Crofer22H

4.2.7 Thermal cycling study on metal filler reinforced sealants

The glass composites of HAg40 and HNC30 were selected for a thermal cycling study (0-50 times) under 800 °C since their joint with OTM stuck components exhibited excellent joining characteristics after 850 °C 10 h joining. The sandwiched joints were joining firstly at 850 °C 10 h, then put into furnace for different times thermal cycling. The gas-tightness and the cross-sections of the joints were investigated.

Table 4-5 listed the gas leakage test results of the joints Aluchrom/HAg40/Aluchrom and Aluchrom/HNC30/Aluchrom under different thermal cycling times (0-50). It is obvious that the joints sealed by HAg40 and HNC30 after cycling times up to 20 times both received an excellent gas-tightness with leakage rate smaller than 10^{-9} mbar·l·s^{-1}. With the cycling times increased up to 50 times, HAg40 joint did not adhere well anymore to the steel surface and some cracks through the sealant were formed as seen Fig. 4-23 (a). Besides, HNC30 joint got a helium leakage rate 5×10^{-4} after 50 thermal cycles. Red ink penetration method was applied to inspect the defect of the HNC30 joint after 50 times cycling. Fig. 4-23 (b) shows a macrograph of the Aluchrom/HNC30/Aluchrom joint after forcibly taken apart. Red ink penetrated into some areas of the sealants. From SEM image Fig. 4-23 (c) one can see that the crack formed and propagated through Aluchrom and sealant HAg40 surface. This may be caused from the thermal expansion difference between Aluchrom and sealant HAg40. In Fig. 4-23 (d), the homogeneous structure and

good adhesion between Aluchrom and HNC30 sealant after 50 times cycling is shown. EDS mapping analysis revealed that Ni-Cr particles from sealant HNC30 were oxidized after 50 times cycling, as visible in Fig. 4-24, and the oxidized layer coating the grain is Cr_2O_3. The oxidation level of filler Ni-Cr increased with thermal cycling time, which could cause the higher leakage rate of HNC30 joint after 50 times cycling.

Table 4-5. Gas leakage results for the joints (Aluchrom/sealant/Aluchrom) joined at 850 °C for 10 h by HAg40 and HNC30 and then thermal cycling different times (0-50), thermal cycling program: heating up to 800 °C for 1 h then cooling down to room temperature with same heating and cooling rate 2 °C/min in air

Cycling times	Sealant	Gas tightness $mbar \cdot l \cdot s^{-1}$	Sealant	Gas tightness $mbar \cdot l \cdot s^{-1}$
0	HAg40	$<10^{-9}$	HNC30	$<10^{-9}$
2	HAg40	$<10^{-9}$	HNC30	$<10^{-9}$
5	HAg40	$<10^{-9}$	HNC30	$<10^{-9}$
10	HAg40	$<10^{-9}$	HNC30	$<10^{-9}$
20	HAg40	$<10^{-9}$	HNC30	$<10^{-9}$
50	HAg40	leakage	HNC30	5×10^{-4}
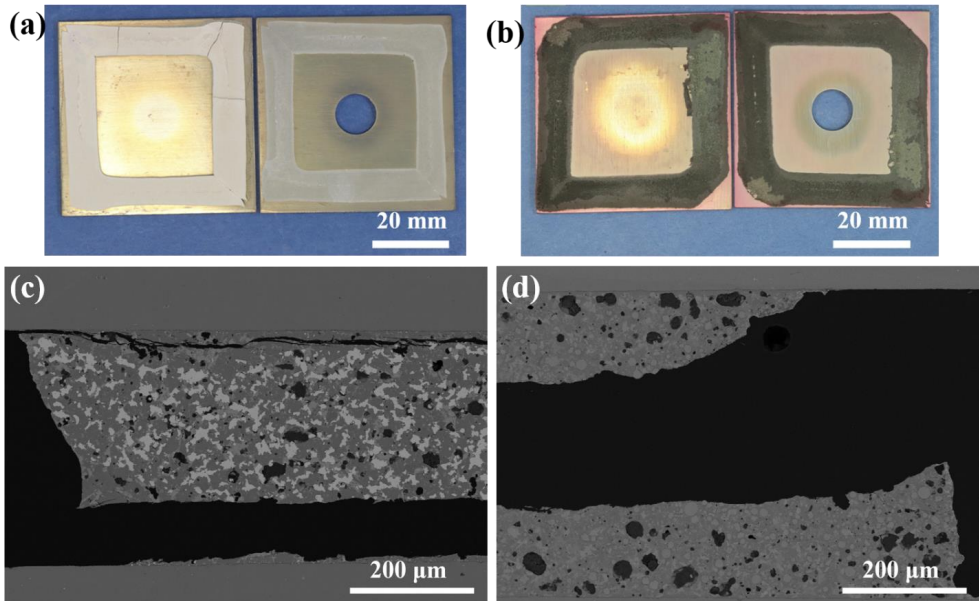
Fig. 4-23. Gas tightness joints Aluchrom/sealant/Aluchrom 50 times cycling thermal treatment, (a) the joint Aluchrom/HAg40/Aluchrom not adhesion anymore after 50 times cycling, (b) after ink penetration test, the chopped Aluchrom/HNC30/Aluchrom joint, some part red ink penetrated into the joint, (c) SEM image of the 50 times cycling cross section of joint Aluchrom/HAg40/Aluchrom, (d) cross section microstructure of the chopped joint Aluchrom/HNC30/Aluchrom after 50 times cycling.
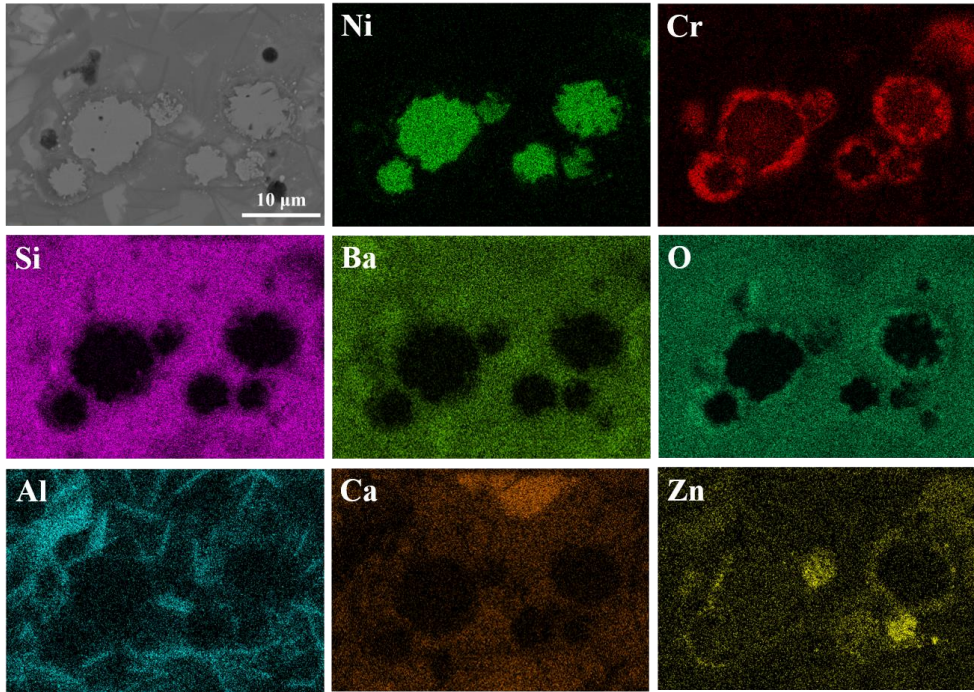
Fig. 4-24. EDS maps of the joint Aluchrom/HNC30/Aluchrom after 50 times thermal cycling

Fig. 4-25 shows the SEM images of the assembled joints STF25/sealant/Aluchrom sealed by HAg40 (a, b) and HNC30 (c, d) after different cycling times. The microstructures of the sealants HAg40 and HNC30 are similar when comparing between 2 times and 10 times cycling. Small cracks could be found after 10 times cycling in HAg40 joint, as well as for 2 times cycling HNC30 joint and 10 times HNC30 joints, which may be caused from metallographic process. The two sealants both joined well with membrane STF25 and Aluchrom.
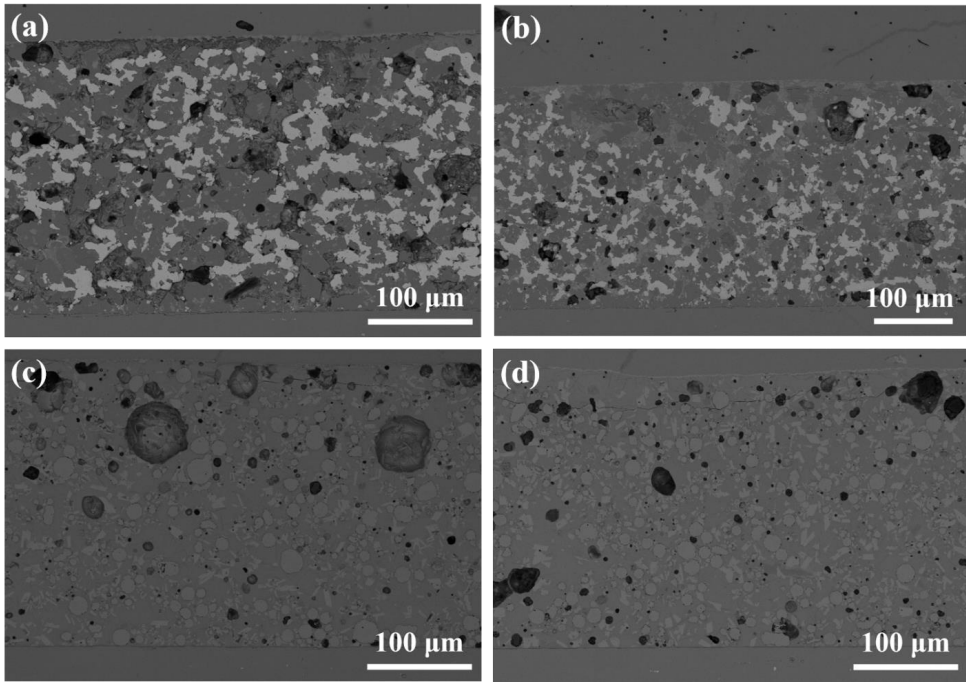
Fig. 4-25. SEM images of the assembled joints after different cycling times, (a) STF25/HAg40/Aluchrom, 2 times cycling, (b) STF25/HAg40/Aluchrom, 10 times cycling, (c) STF25/HNC30/Aluchrom, 2 times cycling, (d) STF25/HNC30/Aluchrom, 10 times cycling.

4.2.8 Long term stability of metal filler reinforced sealants

With the knowledge obtained from the investigations reported in part 4.1, one can know that the glass matrix H would partially or nearly completely crystallize after thermal treatments in the temperature region of 800-850 °C. Joining behaviors of the glass-based sealant could be possibly influenced by the amount of crystal phases, especially under long term thermal exposure. If the glass-based sealant HAg40 and HNC30 want to be used in OTM stack, long term thermal stability is a requirement which needs to be considered. So, joining behaviors for HAg40 and HNC30 joints were investigated by heating 500 h, 1000 h and 1500 h at the typical OTM operation temperature 800 °C and were examined by Helium leakage measurements. The joints (Aluchrom/sealant/Aluchrom) were sealed at 850 °C for 10 h firstly.

In Table 4-6 Helium leakage test results of the joints before and after thermal treatments at 800 °C sealed by HAg40 and HNC30 are listed. Both as-joined samples Aluchrom/HAg40/Aluchrom and Aluchrom/HNC30/Aluchrom exhibited excellent gas tightness with leakage rate smaller than 10^{-9}

mbar·l·s^{-1}. After initial quality control of the joining process, the samples were put into furnace again for long term thermal treatment at 800 °C from 500 h to 1500 h. The sample sealed with HAg40 could be resistance to 800°C heating for 1500 h and maintained good gas tightness like the as-joined sample. The sample sealed by HNC30 has already shown leakage rate values of the magnitude 5×10^{-4} mbar·l·s^{-1} after 500 h heating. An ink penetration test was performed for this sample. The pictures of the broken sample are presented in Fig. 4-26. Red ink penetrated into the sealant HNC30, which means there existed cracks and open pores. In similarity to the thermal cycling tests, the Ni-Cr filler particles were oxidized during long term thermal operation resulting in a foamy sponge-like structure close to the interface of the gas atmosphere.

Table 4-6. Gas tightness tests for the joints (Aluchrom/sealant/Aluchrom) before and after long term heat treatments under 800 °C sealed by HAg40 and HNC30

Long term treatment 800 °C	Sealant	Gas tightness mbar·l·s^{-1}	Sealant	Gas tightness mbar·l·s^{-1}
0	HAg40	$<10^{-9}$	HNC30	$<10^{-9}$
500 h	HAg40	$<10^{-9}$	HNC30	5×10^{-4}
1000 h	HAg40	$<10^{-9}$	---	---
1500 h	HAg40	$<10^{-9}$	---	---
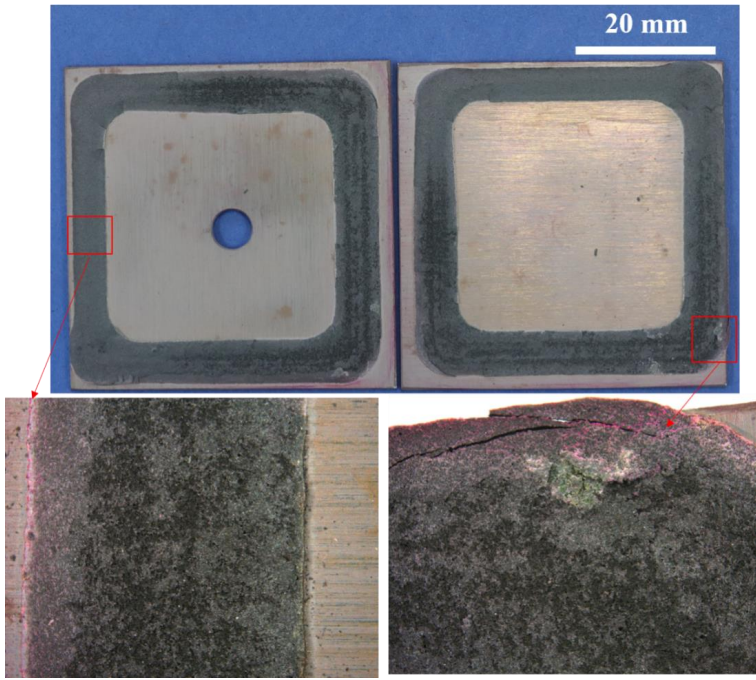
Fig. 4-26. After ink penetration test, the chopped gas-tight joint Aluchrom/HNC30/Aluchrom joint sealed at 850 °C for 10 h and later heated at 800 °C for 500 h

4.2.9 Summary

In this work, seven different filler materials (Ag, Ni, Ni-Cr, CGO, STF25, STF35, and FE) in different proportions were added to a Ba-Ca-Si glass matrix to investigate new sealant with higher CTE value and good joining performance for application in OTM. In chemical compatibility tests, six composites HAg20, HAg30, HAg40, HN30, HNC30, and HCGO20 exhibited good compatibility with the matrix, i.e., glass "H", homogeneous microstructure, moderate porosity, and the required viscous flow. Undesired foaming effects were found for composites with STF25, STF35, and FE.

The CTE improved with increasing filler content. The composites with 40 wt.% Ag and with 30 wt.% Ni resulted in the highest CTE values compared with other filler-reinforced samples: up to 12.9×10^{-6} K^{-1} as-sintered sample and 10.4×10^{-6} K^{-1} after annealing. The decrease in CTE of annealed samples is attributed to the formation of barium feldspar with a low CTE during long-term annealing.

The samples sealed with HAg40 and HNC30 glass composites showed good gas-tightness and sealing behaviors with STF25 and support metals (Aluchrom and pre-oxidized Aluchrom). The membrane side with a glass composite sealant formed a transitional thin layer by chemical bonding. On the support metal side, pre-oxidized Aluchrom formed a thicker oxidation Al_2O_3 layer compared with Aluchrom, which enhanced the sealing strength at the joints by forming chemical bonds with the glass matrix.

Mechanical shear strengths of two sealants HAg40 and HNC30 were measured by torsion test on the hourglass-shaped samples at room temperature. The sealed joint with HAg40 achieved the higher shear strength value of 62.2 ± 2.8 MPa, which is in the similar range compared to state-of-art sealants for SOFCs. The samples sealed with HAg40 and HNC30 after cycling times up to 20 times at 800 °C received an excellent gas-tightness with leakage rate smaller than 10^{-9} mbar·l·s^{-1}. The joint of HAg40 can resist 1500 h heat treatment at 800 °C with maintaining good gas tightness. Of all the investigated joining materials, HAg40 is the most promising candidate as sealant for OTM.

4.3. Fast joining process investigation

4.3.1 Motivation

Energy crisis is one of serious challenges in the 21st century. Energy economizing production process could be beneficial for industry fields to save the cost of manufacture. According to state of art reported in literatures, long joining process were commonly used when glass-based sealants were applied in high temperature joining for SOFC and OTM. The joining experiments of BaO-CaO-SiO$_2$ system glass "H" and glass H composites reinforced by ZrO$_2$ were carried out at 850 °C and dwelling for 10 h [109]. Greven reported multilayer glass-ceramic sealants also joined at 850 °C for 10 h in a resistance heated chamber furnace in air [148]. Rodriguez-Lopez et al. reported joining behavior of MgO–BaO/SrO–B$_2$O$_3$–SiO$_2$ glass sealant joined at 850 °C with a dwell time of 10 h [132]. Reddy et al. investigated SrO-containing diopside glass-ceramic sealants joined 850 °C with a hold time of 250 h to complete the joining process [149].

The glass joining process is similar to the brazing method with metal alloys. For both their joining processes the assembled sample are put into the heating furnace. The connection is made by wetting the base materials with the brazing solder or glass sealant in the intermediate layer and diffusion processes occur. While the heating time used for brazing is relatively short compared to glass joining. Kaletsch at al. reported that oxygen transport membrane Ba$_{0.5}$Sr$_{0.5}$Co$_{0.8}$Fe$_{0.2}$O$_{3-\delta}$ and AISI 314 were brazed by reactive air brazing alloy Ag3Cu with 3 at% copper at 955 °C for 0.2 h [55]. Kiebach et al. adopted 940 °C to braze Ba$_{0.5}$Sr$_{0.5}$Co$_{0.8}$Fe$_{0.2}$O$_3$ membrane ceramic and high temperature alloys for 20 min with the help of Ag solder [62]. Raju et al. reported oxygen transport membrane ceramic and Crofer 22 APU joining by reactive air brazing with Ag–10 wt.% CuO at 1050 °C for 30 min [150].

Based on the reflection on the glass joining process and inspiration by the reactive air brazing process, fast joining process would be meaningful and worthwhile for our glass composite sealants at higher temperatures than 850 °C. There are several advantages: first, using high temperature joining increases fluidity of glass and wetting to base materials (OTM ceramic and alloy). Second, lowering the sealing time at high temperatures could decrease oxidation of support metal. In addition, applying a fast joining process could save energy and time which is favorable for future industrial applications.

In this study several fast joining processes were investigated for two glass-based sealants HAg40 and HNC30. First, hot stage microscopy (HSM) was carried out to monitor shrinkage, softening and viscous flow behaviors of HAg40 and HNC30. Based on these results optimum joining temperature zone could be determined for fast joining experiments. In order to evaluate fast joining processes, joining behaviors of the sealants were examined by helium leakage detection, x-ray computed tomography (CT) and microstructural analysis on cross-sections by scanning electron microscopy (SEM) with energy-dispersive x-ray spectroscopy (EDS).

4.3.2 Shrinkage and viscous behavior investigation on metal reinforced glass composites

The reinforced glass composites HAg40 and HNC30 were examined by means of HSM to investigate viscous flow behavior and to find optimum temperature for joining for an OTM application. The results of HSM measurement are summarized in Fig. 4-27. Fig. 4-27 (a) compares the area deformation rate curves of HAg40 and HNC30. Area deformation rate curve was obtained by dividing the area of the sample shade at each temperature by the initial area of sample shade. There is an expansion behavior observed at the temperature 750-930 °C from the area deformation curve of HAg40. Then after 930 °C, near half ball temperature, a quick shrinkage occurs for the HAg40 sample. Fig. 4-27 (b) summarizes the shadow images of HAg40 at the fixed viscosity temperature values (T_{FS}, T_{MS}, T_D, T_{HB} and T_F). No sphere ball point was observed from HSM measurement for HAg40. The T_{HB} is at 935 °C. The thermal expansion coefficient of Ag filler is higher than glass H matrix, which may provoke an expansion behavior at temperature 750-930 °C, afterwards the pellet shows a quick creep collapse due to viscous flow effects of glass matrix and softening of Ag filler. From the shrinkage behavior, the optimal joining temperature of HAg40 glass-composite sealant is assumed to be around high expansion of area deformation rate and half ball temperature 935 °C, i.e., 880 °C – 935 °C.

For HNC30 sealant, there is an area expansion behavior higher than 950 °C, which is possibly caused by Ni-Cr particle oxidation at high temperatures. In that case, the joining temperature of HNC30 sealant should not be chosen higher than 950 °C. Fig. 4-27 (c) summarizes the shadow images of HNC30 at the fixed viscosity temperature values (T_{FS}, T_{MS}, T_D, T_S, T_{HB} and T_F). The sphere ball point of HNC30 is measured at 880°C. The half ball point is recorded at 920 °C. From the shrinkage behavior, the optimal joining temperature of HNC30 glass-ceramic sealant is assumed to be around sphere point and half ball temperature, i.e., 880 °C – 920 °C.

The method proposed by Pascual et al. [73] was adopted to predict the viscosity-temperature data of the glass-ceramic sealants HAg40 and HNC30 based on hot stage microscopy (TOMMIplus). The viscosity-temperature data of the two composites were compared with pure glass matrix H [82] as seen the Table 4-6. Around typical joining temperature 850 °C, glass H is at forming half ball stage [82], but the half ball temperatures of the two composites are much higher. The addition of ceramic fillers could reduce the creep behavior of sealant at high temperature. And filler type and amount also effect deformation and viscous behavior of the sealants at high temperature.
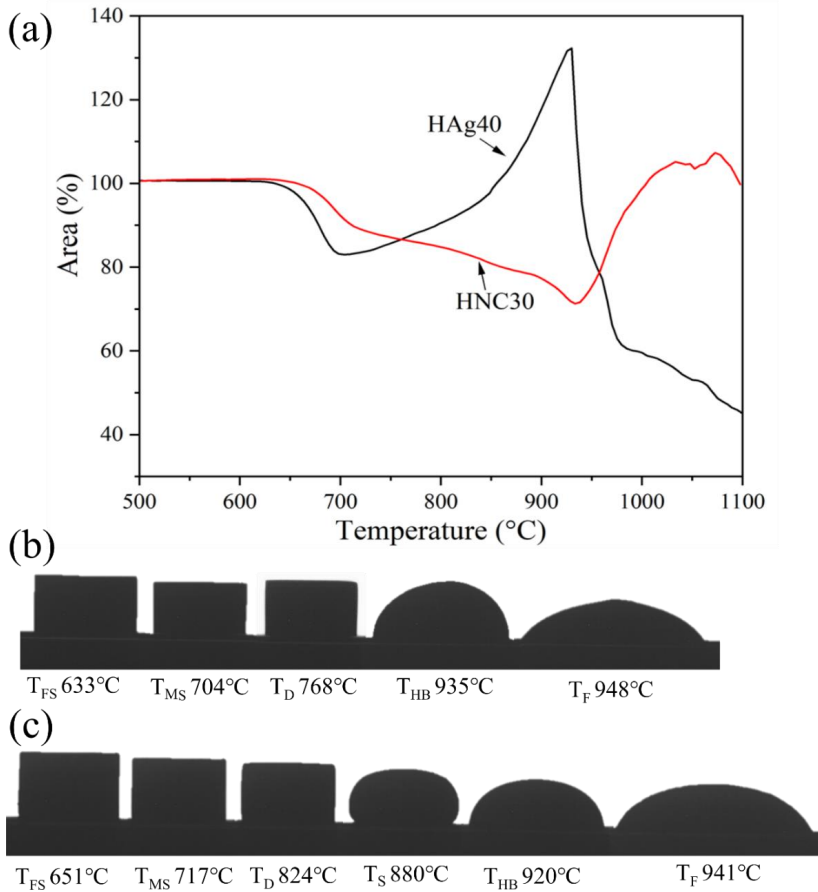
Fig. 4-27. HSM analysis (TOMMIplus) for HAg40 and HNC30 glass composite sealant on Crofer22APU substrate recorded at 5 °C/min, (a) area deformation versus temperature curves, (b) shadow images of HAg40 at the fixed temperatures, (c) shadow images of HNC30 at the fixed temperatures

Table 4-6. Fixed viscosity temperatures of pure glass H [82] and glass H reinforced composites HAg40 and HNC30

Sample	Fixed viscosity (log η) [73], η (dPa.s)					
	9.1	7.8	6.3	5.4	4.1	3.4
	Temperature (°C)					
	T_{FS}	T_{MS}	T_D	T_S	T_{HB}	T_F
Glass H [82]	610	725	730	795	844	-----
HAg40	633	704	768	----	935	948
HNC30	651	717	824	880	920	941

4.3.3 Effect of fast sintering processes on sealant gas tightness

In order to pursue a more environmental friendlier and cost-efficient joining process, the joining temperature and dwell time of the two sealants were explored for further industrial application. The joining temperatures of HAg40 and HNC30 were selected according to the above hot stage microscopy analyses for each glass composite sealant instead of the typical joining process at 850 °C for 10 h. For the composite HAg40, four sealing processes with Aluchrom plates were tested: 935 °C for 5 min, 920 °C for 15 min, 900 °C for 30 min, 880 °C for 30 min. For the composite HNC30, following four sealing processes with Aluchrom plates were tried: 880 °C for 15 min + 920 °C for 5 min, 920 °C for 5 min, 900 °C for 15 min, 880 °C for 30 min. The Helium leakage results joined under different thermal process by two glass composites are summarized in Table 4-7. All of the samples exhibit low helium leakage values below the detection limit of 10^{-9} mbar·l·s^{-1}, which fulfills the requirements for the high temperature operation of the OTM stack [143]. The sealing process is affected by temperature and dwell time. Adhesion with the components of OTM happened by wetting behavior of glass viscous flow and diffusion process at high temperature. High temperature joining process contributes to the reduction of glass matrix viscosity and the increase of kinetic energy for molecular diffusion. In order to obtain good sealing result, dwell time was adjusted for gas-tight setup, for example the joining processes 920 °C 5 min and 880 °C 30 min sealed by HNC30 received same gas-tightness result. A dwell time of 30 min is counted as short joining comparing to typical glass joining time 10 h which is much favorable for an industrial application.

Table 4-7. Gas tightness tests for the sandwiched samples sealed by HAg40 and HNC30 under different joining process

Sealant	Joining process	Gas tightness mbar·l·s^{-1}	Sealant	Joining process	Gas tightness mbar·l·s^{-1}
HAg40	935 °C, 5 min	$<10^{-9}$	HNC30	880 °C, 15 min + 920 °C, 5 min	$<10^{-9}$
HAg40	920 °C, 15 min	$<10^{-9}$	HNC30	920 °C, 5 min	$<10^{-9}$
HAg40	900 °C, 30 min	$<10^{-9}$	HNC30	900 °C, 15 min	$<10^{-9}$
HAg40	880 °C, 30 min	$<10^{-9}$	HNC30	880 °C, 30 min	$<10^{-9}$

4.3.4 Internal structure analysis by X-ray computed tomography

Assembling tests were performed by joining membrane STF25 and counterpart Aluchrom together with the help of sealant HNC30 and HAg40. The effects of several fast joining processes were inspected by X-ray computed tomography (CT) to the joints without destruction of the joints. Fig. 4-28 exhibits CT images of the joints from inner scanning longitudinal section.

From Fig. 4-28 (a), one can see that the sample STF25/HNC30/Aluchrom after joining at 880 °C, 15 min + 920 °C, 5 min obtained a dense and compact sealant joining layer, except of some small round closed pores distributed near the center of the joining layer. By contrast, there are some large sized pores formed in the sealant HAg40 layer at joining temperature of the sample 935 °C for 5 min as shown in Fig. 4-28 (b). It can be explained that the glass matrix has better fluidity at high temperature, resulting in the non-smooth joining structure of HAg40. And pores agglomerated at higher temperature easily. Besides, filler amount also effects the size and number of pores. Same samples joined at lower temperature were prepared and the cross-sections of the joints was analyzed by SEM.
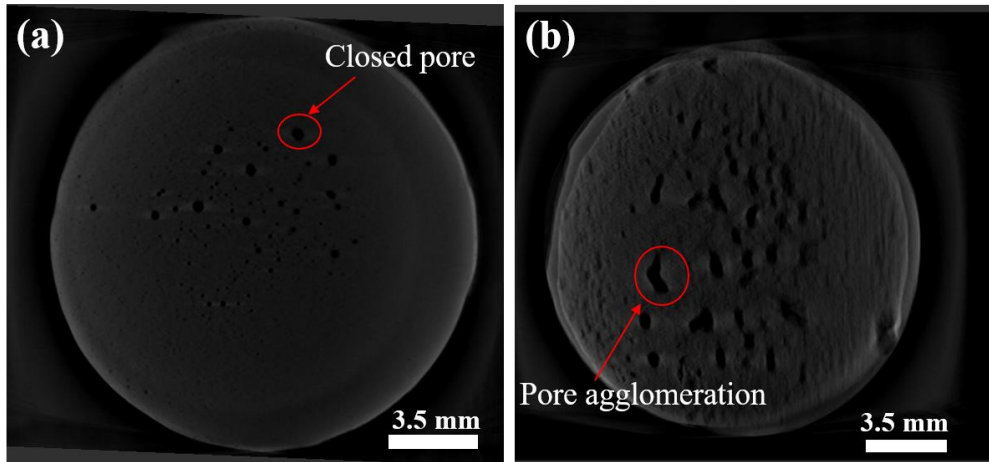
Fig. 4-28. CT images of inner scanning from longitudinal section for inspecting sealants joining behaviors without destruction, (a) STF25/HNC30/Aluchrom joining at 880 °C, 15 min + 920 °C, 5 min, (b) STF25/HAg40/Aluchrom joining at 935 °C, 5 min

4.3.5 Microstructure analysis for fast joining samples

The effects of fast joining processes were also evaluated by destructive analytical techniques via SEM analyses on metallographically prepared cross-sections of the joints.

4.3.5.1 HNC30

The microstructures of STF25/HNC30/Aluchrom joints sealed by three different joining processes are presented in Fig. 4-29: (a-c) 880 °C 15 min + 920 °C 5 min, (d-f) 900 °C 15 min, (g-h) 880 °C 15 min. There is a crack formed near membrane STF25 side in the joint STF25/HNC30/Aluchrom (880 °C 15 min + 920 °C 5 min) as seen Fig. 4-29 (a), which probably was caused by metallographic preparation. Sealant HNC30 exhibited good joining behavior with STF25 and Aluchrom in all three joining processes. Besides, pores and Ni-Cr filler particles are uniformly dispersed in the sealant layer. Sealant HN30 exhibits homogeneous structures in all three joining processes. There are some small crystals that preferentially precipitated from the two interfaces. The glass matrix H in the fast-joined samples basically retains the glassy phase only with tiny crystallization, comparing to the traditional joined samples at 850 °C for 10 h.
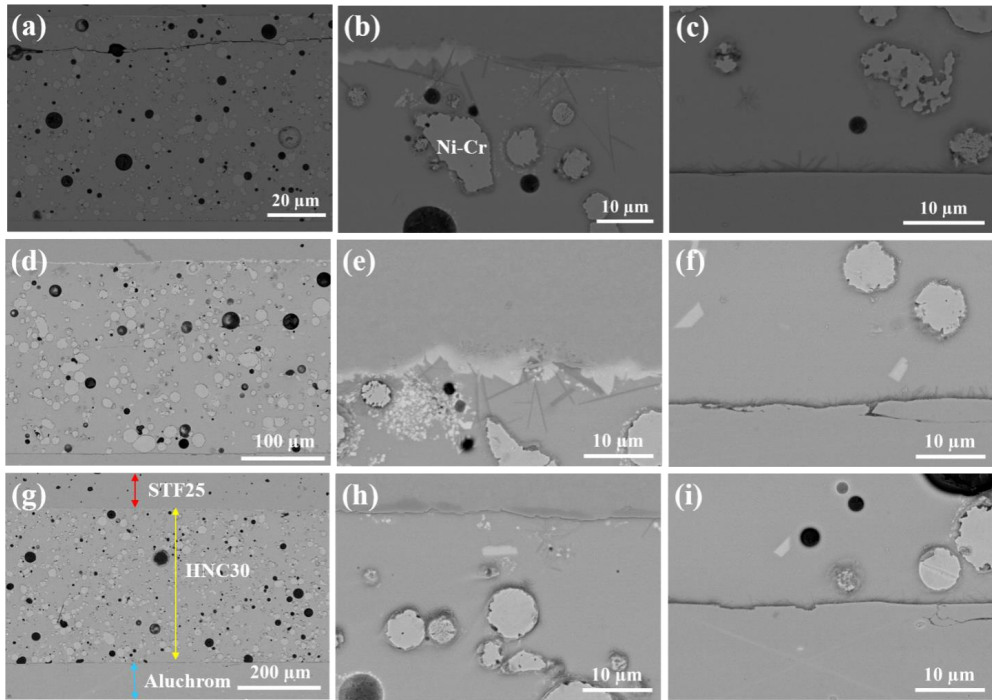
Fig. 4-29. SEM images of cross-section of STF25/HNC30/Aluchrom, (a-c) 880 °C 15 min + 920 °C 5 min, (d-f) 900 °C 15 min, (g-i) 880 °C 30 min

In order to investigate the filler Ni-Cr oxidation condition and the crystalline phases formed at interphase, EDS mapping and line scanning were performed. From Fig. 4-30 SEM-EDS maps of STF25/HNC30/Aluchrom joined at 880 °C 15 min + 920 °C 5 min, it can be seen that the filler was oxidized because Cr and O slightly stood out at the edges of the filler particles. While, the oxidation condition of Ni-Cr is slight compared with the HNC30 sample joined at 850 °C for 10 h (Fig. 4-9). Fig. 4-31 shows line scanning through the interface between sealant HNC30 and Aluchrom joined at 880 °C 15 min + 920 °C 5min. There is a continuous thin oxidation layer formed at the interface between glass composite seal and Aluchrom, which is assumed to be Al_2O_3. The precipitated crystalline phase from glass matrix is detected to be $BaAl_2Si_2O_8$, which agrees with the results from traditional joining process. $BaAl_2Si_2O_8$ crystallizes at first in glass matrix H during fast joining processes.
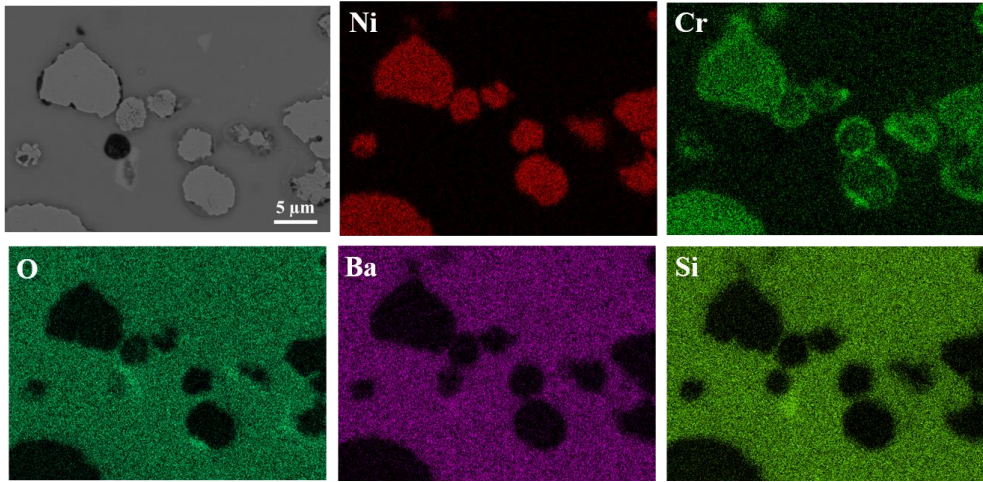
Fig. 4-30. SEM-EDS maps of STF25/HNC30/Aluchrom, joined at 880 °C 15 min + 920 °C 5 min, for investigating the condition of filler Ni-Cr
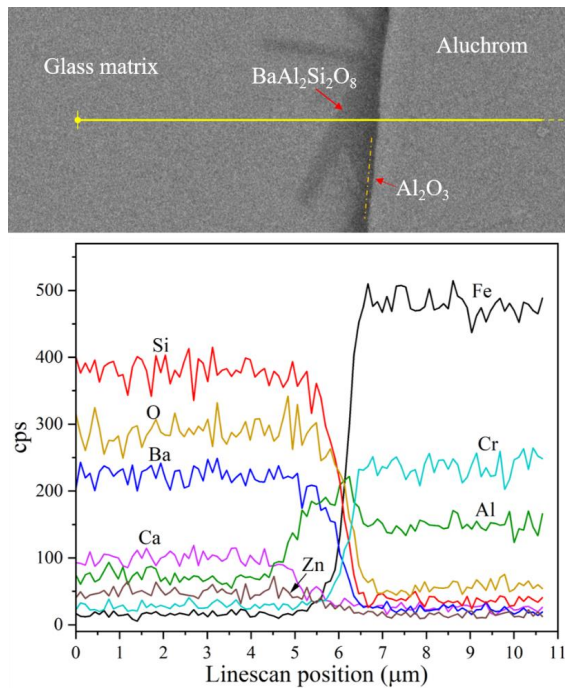
Fig. 4-31. Line scan through the interface between sealant HNC30 and Aluchrom joined at 880 °C 15 min + 920 °C 5 min

4.3.5.2 HAg40

Fig. 4-32 shows microstructures of joints STF25/HAg40/Aluchrom joining at different processes, (a-c) 935 °C 5 min, (d-f) 900 °C 30 min. Ag particles appear to agglomerate at high temperatures for both fast joining processes because some of the silver particles have been connected together and are larger than the size of the original size of Ag filler added to the green composite mixture. The large collapsed Ag particles aggregated in the middle during the joining process, leaving glass matrix phase and small amount of Ag nanoparticles at the interfaces to the steel, which results in uneven distribution of filler in the sealant layer. Microcracks formed in the sealant layer near STF25, probably due to the difference in thermal expansion coefficients between glass matrix and STF25. Lowering the joining temperature could alleviate the aggregation of Ag particles to the middle of sealant layer, but 900 °C 30 min is not the best joining process comparing with the filler distribution and joining results of HAg40 joining at 850 °C for 10 h.
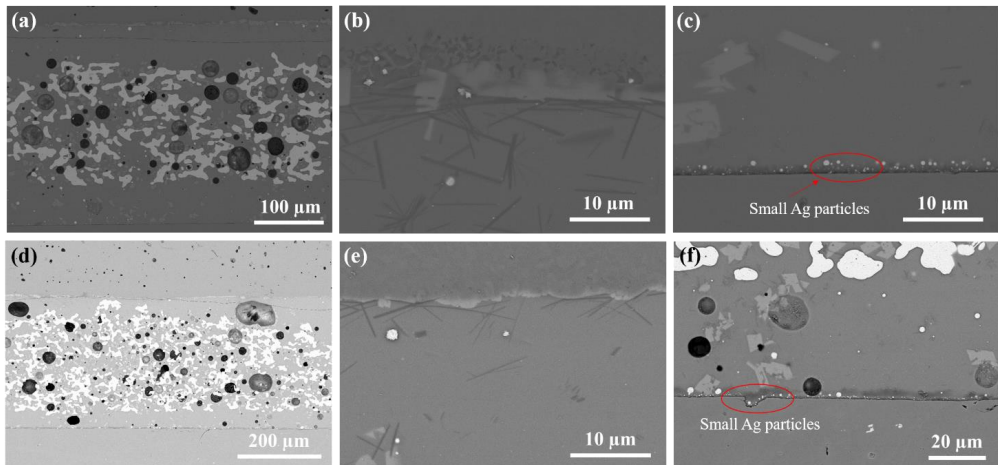
Fig. 4-32. SEM images of cross-section of STF25/HAg40/Aluchrom, joining at: (a-c) 935 °C 5 min, (d-f) 900 °C 30 min

4.3.6 Summary

The feasibility of fast joining process was investigated for two glass-based sealants HAg40 and HNC30. Viscous flow behavior and optimum joining temperature zone were monitored by HSM. The optimal joining temperature of HAg40 glass-composite sealant is assumed to be around high expansion of area deformation rate and half ball temperature 935 °C, between 880 °C – 935 °C. The optimal joining temperature of HNC30 glass-ceramic sealant is assumed to be around sphere point and half ball temperature, between 880 °C – 920 °C. All of the fast-joined samples obtained low helium leakage values below the detection limit of 10^{-9} mbar·l·s^{-1}, which will fulfill the requirements for the high temperature operation of the OTM stack.

The sample STF25/HNC30/Aluchrom joining at 880 °C, 15 min + 920 °C, 5 min received a dense and good sealant joining layer from CT inspection. Whereas there are some large sized pores formed in the sealant HAg40 layer at joining temperature 935 °C for 5 min.

Sealant HNC30 exhibited homogeneous structures and good joining behavior with STF25 and Aluchrom in all three joining processes from microstructural analysis. There are some small crystals that preferentially precipitated near the two interfaces. The glass matrix H in the fast-joined samples basically retains the glassy phase only with tiny crystallites formed, and the oxidation condition of filler Ni-Cr is reduced, when comparing with the sample of HNC30 joined at 850 °C for 10 h.

The large Ag particles aggregated to the middle during the fast-joining process, leaving glass matrix phase and small amount Ag nanoparticles at the interfaces to the Aluchrom, which results in an uneven distribution of filler and microcracks formed in the sealant layer near STF25. Lowering the joining temperature could alleviate the aggregation of Ag particles, but the reduction to 900 °C 30 min was not sufficient to reach the best filler distribution and joining results as obtained in the joining process of HAg40 joining at 850 °C for 10 h.

4.4 Ceramic BaSiO$_3$ reinforced glass composite sealants

4.4.1 General remark

Ceramic oxygen transport membrane (OTM) is a functional reactor medium to produce synthesis gas from carbon fuels and possibly capture CO_2 from exhaust gas. Sealants are needed to assemble OTMs with support metals to modules for their application in industrial process. Barium-calcium-silicate glass "H" was investigated as a sealant matrix for joining OTMs because of its excellent viscosity, chemical compatibility, and joining properties demonstrated in solid oxide fuel cell (SOFC) applications [20].

The only shortcoming of glass H (9.6×10^{-6} K^{-1}) is the relatively low thermal expansion coefficient (CTE) comparing with membrane materials STF25 (12×10^{-6} K^{-1}). Adding filler materials with higher thermal expansion coefficient into the glass matrix is a feasible strategy to obtain suitable thermal expansion coefficients [109]. The properties of glass-based sealants can be tailored for OTM sealing by filler addition [13, 151]. Brendt et al [94]. described the crystallization behavior of glass H and reported the formation of barium silicate during heat treatment at 850 °C. BaSiO$_3$ exhibits a high thermal expansion coefficient around 16.9×10^{-6} K^{-1} [79]. The CTE value of composite sealants can be adjusted by controlling the amount of reinforcement filler material BaSiO$_3$. When BaSiO$_3$ filler is added to the glass H matrix, good compatibility with the glass matrix and suitable thermal expansion can be expected to this composite sealant.

In this study, BaSiO$_3$ was added as filler material to glass H in various amounts to obtain composite sealants, as listed in Table 4-8. In-house synthesized powder of BaSiO$_3$ was analyzed by XRD first. The thermal expansion properties of the composites were measured using a dilatometer apparatus. Hot stage microscope (HSM) was adopted to investigate shrinkage and viscosity behavior of the composite and optimum temperature for joining in the OTM application. Joining behaviors of the sealant were examined by helium leakage detection, x-ray computed tomography (CT) and microstructural analysis on cross-sections by scanning electron microscopy (SEM) with energy-dispersive x-ray spectroscopy (EDS).

Table 4-8. Abbreviations of glass ceramic composites

Abbreviation	Glass H	Fillers	
HBS10	90 wt.%	BaSiO$_3$	10 wt.%
HBS20	80 wt.%	BaSiO$_3$	20 wt.%
HBS30	70 wt.%	BaSiO$_3$	30 wt.%

4.4.2 XRD analysis for BaSiO₃

X-ray diffraction was used to characterize the phase for the in-house synthesized filler material BaSiO₃. The XRD result presented in Fig. 4-33 verify that raw filler powder is a pure material with orthorhombic BaSiO₃ phase (ICDD: 01-0700-2112).
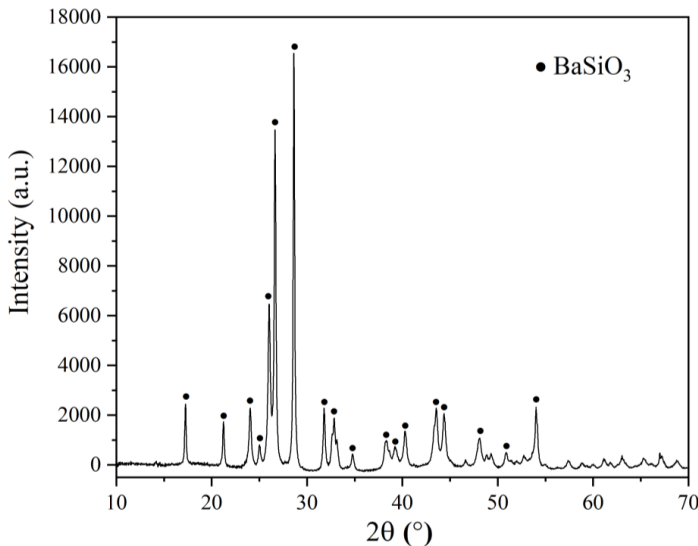
Fig. 4-33. XRD pattern of the BaSiO₃ filler

4.4.3 Investigate BaSiO₃ filler amount on thermal expansion coefficients of glass composites

In Fig. 4-34 (a) the thermal expansion behaviors of the glass-ceramic composite samples are reported as a positive function of the reinforced BaSiO₃ filler. It can be observed that the thermal expansion coefficient (CTE) of the composites increases with increasing the filler amount. This can be explained by the CTE of BaSiO₃ (16.9×10^{-6} K^{-1} [138]) being higher than the glass matrix H. All three composites show a distinct amorphous behavior with a stepwise increase of CTE between 550 and 680 °C. The CTE values of the annealed samples are lower compared to the as sintered composites, which is shown in Fig. 4-34 (b). Still the CTE values show similar ranking with the increase of filler material amount as found for the sintered composites. The addition of 30 wt.% BaSiO₃ resulted in the highest CTE values of up to 11.9×10^{-6} K^{-1} as-sintered sample and 10.4×10^{-6} K^{-1} after annealing, respectively, measured in a temperature range between 200 °C and 900 °C (see Table 4-9). As known by literature data of glass H [13, 94], the formation of low CTE phase BaAl₂Si₂O₈ (7×10^{-6} K^{-1} [82]) is the main reason that caused the declination of CTE values after long-term annealing.
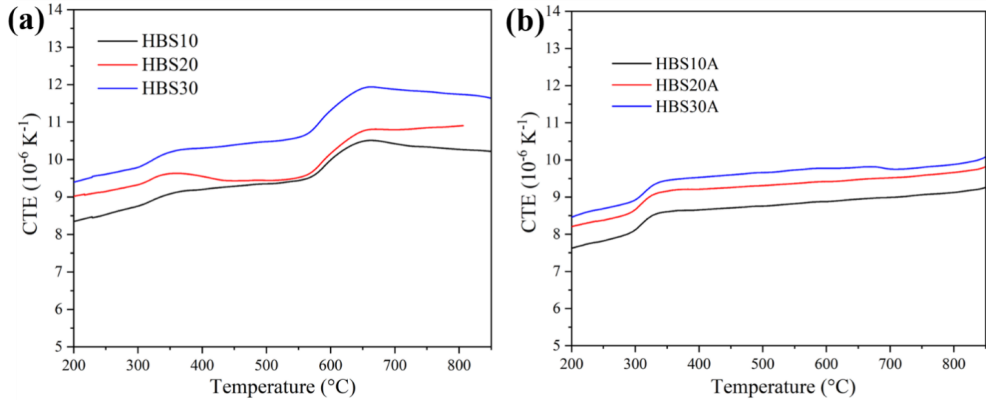
Fig. 4-34. Dilatometer curves of glass H reinforced by $BaSiO_3$ with different amount, (a) composite samples as sintered after heat treatment at 850 °C for 10 h, (b) additionally treated at 800 °C for 1000 h

Table 4-9. Thermal expansion coefficients (as-sintered and long term-annealed) of the glass H and glass ceramic composite sealants

Sample	CTE [×10^{-6} K^{-1}] (200-900 °C)	Annealed sample	CTE [×10^{-6} K^{-1}] (200 – 900 °C)
Glass H [82]	----	HA	----
HBS10	8.4-10.5	HBS10A	7.7-9.7
HBS20	9.1-10.8	HBS20A	8.2-10.1
HBS30	9.5-11.9	HBS30A	8.5-10.4

Fig. 4-35 shows the SEM micrographs of the glass composites reinforced by $BaSiO_4$ after 800 °C annealing 1000 h. One can see that the big $BaSiO_4$ grains caused some cracks. In Fig. 4-35 (d), barium silicate phase was detected in gray which maybe the phase formed from residual glass or fain powder of $BaSiO_4$. The needle-like phase is $BaAl_2Si_2O_8$. The light dot phase is Ba/Al/Si. The light gray phase is Ba/Zn/Si. And residual glass phase still exists in the long-term annealed sample.
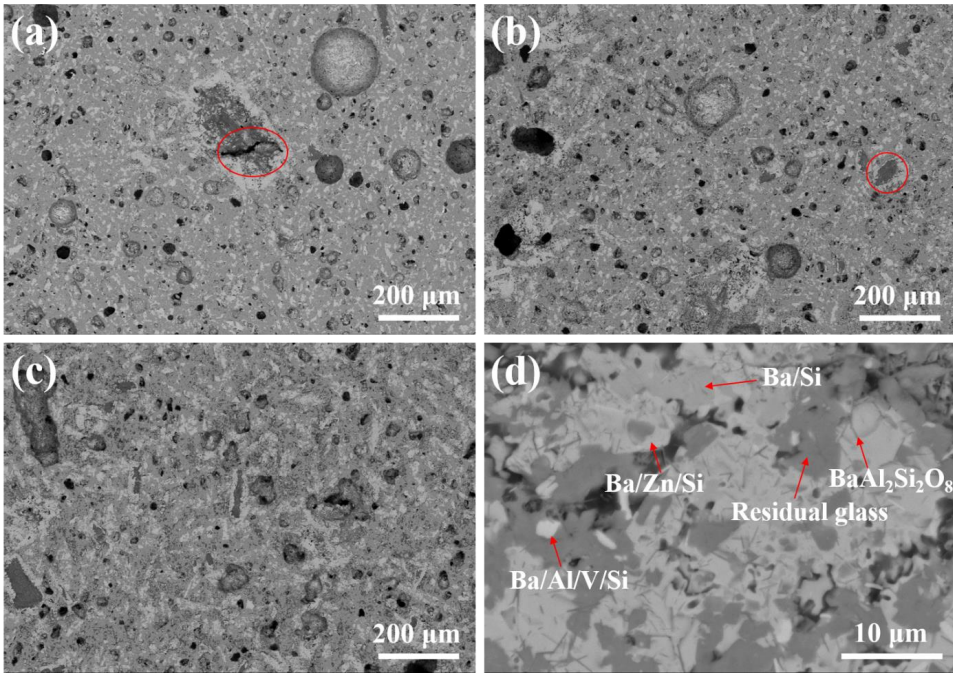
Fig. 4-35. SEM-EDS analyses for annealing composites (a) HBS10A, (b) HBS20A, (c) HBS30A, (d) magnification microstructure of HBS30A

4.4.4 Viscous flow behavior of BaSiO₃ reinforced sealant

The reinforced composite HBS30 was chosen as possible joining material for OTMs and the other composite materials were rejected for the following experiments. The material was examined by means of hot stage microscopy to investigate its shrinkage shrinking behavior and optimum joining temperature, as visualized in Fig. 4-36. Fig. 4-36 (b) summarizes the shadow images at the fixed viscosity temperature values (T_{FS}, T_{MS}, T_D, T_S, T_{HB} and T_F). First shrinkage temperature is at 672 °C. Maximum shrinkage point is at 748 °C. Half ball point is around 951 °C, which is higher than pure glass H half ball point 844 °C [82]. From the shrinkage behavior, the optimal joining temperature of HBS30 glass-ceramic sealant is assumed to be around maximum expansion peaks height and area variation ratio curves and half ball temperature (T_{HS}) 951 °C, i.e., 920 °C – 960 °C.
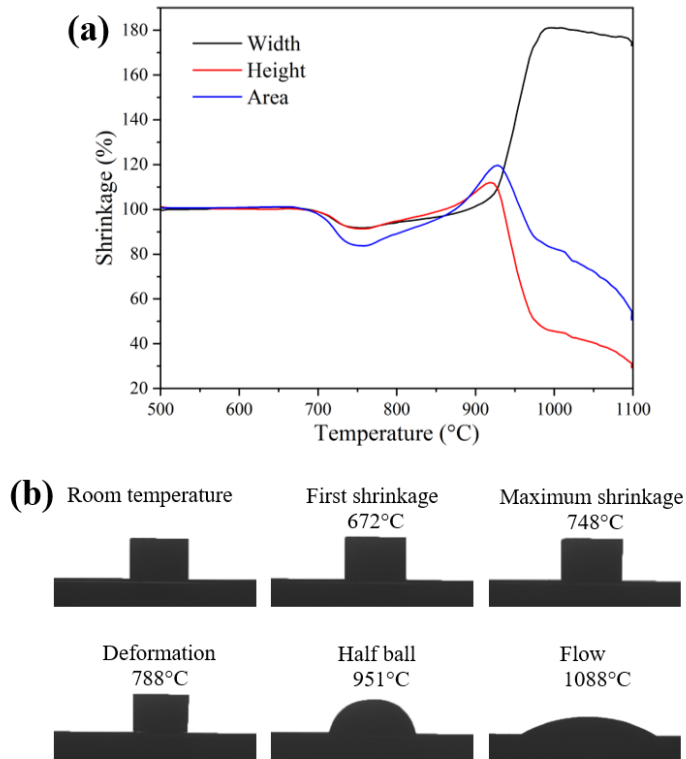
Fig. 4-36. HSM analysis (TOMMIplus) for HBS30 glass composite sealant on Crofer22APU substrate recorded at 5 °C/min, (a) shrinkage curves, (b) Shadow images of the sample at the fixed temperatures

4.4.5 Gas tightness test of BaSiO$_3$ reinforced sealant

The gas tightness results of samples joined under different thermal processes by HBS30 glass composite are summarized in Table 4-10. Three joining temperatures were chosen for this study: 850 °C as the typical joining temperature used in SOFC glass-sealing, in addition 920 °C and 960 °C as maximum expansion of area shrinkage and beginning of the flow temperature according to the above described HSM analysis. Sealing performance of HBS30 sealant with different counterparts (Crofer22APU, Aluchrom and pre-oxidized Aluchrom) were analyzed by Helium leakage test. The setups joined at 850 °C for 10 hours showed leakage for all combinations. For pure glass H, the best sealing temperature is around half ball temperature 850 °C [82]. In our study, the addition of filler material strongly reduces the viscous flow of glass at comparable temperatures.

Elevated temperatures for the joining process could be a feasible strategy to achieve good sealing behaviors with the new composite mixture.

The samples joined at higher temperatures of 960 °C and 920 °C have shown low helium leakage rates below the detection limit of 10^{-9} mbar·l·s^{-1}, which will fulfill the requirements for the high temperature operation of an OTM module [143]. At the same joining temperature, the samples sealing with different metal alloys achieve same sealing performance. Joining temperature should be the key factor in sealing success instead of metal counterparts. In general, under elevated temperature glass sealants have better viscous properties and improved wetting behaviour of the counterparts, which also could explain the low leakage rates of HBS30 after joining at 960 °C and 920 °C.

Table 4-10. Gas tightness measurements of samples sealed by HBS30 sealant after different thermal treatments

Joining process	Substract	Gas tightness (mbar·l·s^{-1})
850°C 10h	Aluchrom	leakage
850°C 10h	Pre-oxidized Aluchrom	leakage
850°C 10h	Crofer 22 APU	leakage
960°C 5min	Aluchrom	$<10^{-9}$
960°C 5min	Pre-oxidized Aluchrom	$<10^{-9}$
960°C 5min	Crofer 22 APU	$<10^{-9}$
920°C 15min	Aluchrom	$<10^{-9}$
920°C 15min	Crofer 22 APU	$<10^{-9}$

4.4.6 Internal structure analysis of STF25/HBS30/Aluchrom joints by X-ray computed tomography

CT images of the sample STF25/HBS30/Aluchrom after joining at 960 °C are shown in Fig. 4-37. From the cross section and longitudinal section, one can clearly see the inner joining behavior of the sealant HBS30 without destructive breaking of the sample. There are many pores formed in the sealant during the joining at 960 °C. It can be assumed that small pores are getting into contact with each other and agglomerate at the increased temperatures to form large sized pores. The green circle marks a large pore leaving a gap between support metal and membrane. The foam-like porosity has a high risk of leakage and inadequate strength of the joining material. The joining

process at lower temperature 920 °C are shown in Fig. 4-38, it presented relatively smooth, dense and less pores in the joining layer. It reveals that joining at 920 °C is the more suitable joining process for HBS30 composite sealant.
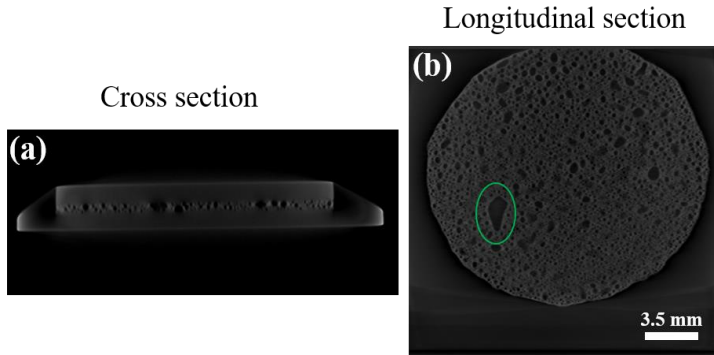
Fig. 4-37. CT images of STF25/HBS30/Aluchrom after joining at 960 °C, (a) cross section scanning, (b) longitudinal section inner scanning in the sealant axis
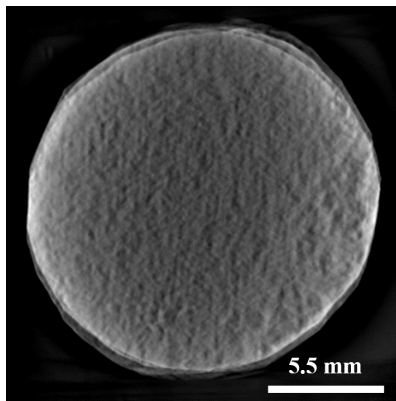
Fig. 4-38. CT images of STF25/HBS30/Aluchrom after joining at 920 °C for 15 min scanning from longitudinal section

4.4.7 Microstructural analysis of joining behavior

The SEM images of cross-sections of joined samples using the sealant HBS30 after thermal treatment at 960 °C are shown in Fig. 4-39. In Fig. 4-39 (a-c) the membrane STF25 was joined with the metal substrate Aluchrom and in Fig. 4-39 (d-f) the membrane STF25 was joined with pre-oxidized Aluchrom. The joining gap of the composite sealant HBS30 was 480 μm for both

samples. The pores formed in the sealant HBS30 are of a round shape, indicating a closed porosity which will not cause gas leakage. Some large sized particles of the filler material $BaSiO_3$ can be recognized, visible as the white phases marked by red circles in Figure 4-39 d. SEM-EDS maps in Fig. 4-40 shows the elemental distribution around a filler particle. A crack was formed, running through the particle. As the size of filler $BaSiO_3$ is rather large, it is discussable if the oversize might lead to a low mechanical property. The $BaSiO_3$ filler particle is surrounded by a thin amorphous layer. In contrast to scientific expectations, glassy matrix phase seems to prevent crack propagation as seen in Fig. 4-40. The filler particle surrounded by a thin residual glass phase layer is then encircled by a crystallized binary Ba-Silicate layer. This layered structure is typical for large sized filler grains. Whereas small size $BaSiO_3$ fillers are hard to recognize because the binary Ba/Si phases precipitated from the glass H matrix after the joining process are mistakable with the same contrasts. There is no crack formation observed in the small size fillers or Ba/Si phases. An improvement for composite sealant production can diminish the filler size effect. The interface between sealant and membrane is shown in Fig. 4-41. The elemental mapping was carried out using the Trumap software in order to resolve the line overlaps of Ba/Ti and Sr/Si. A thin interdiffusion layer around 1 µm thickness was found between the STF25 and the glass matrix, which formed an interdiffusion layer with Ba/Sr/Ti/Si elements. No pores or crack formed near this interdiffusion layer. Besides, a grey needle-like phase is formed, which is assumed to be $BaAl_2SiO_3$, while medium grey blocks exhibit ternary silicate phases consisting of Ba/Ca/Si.
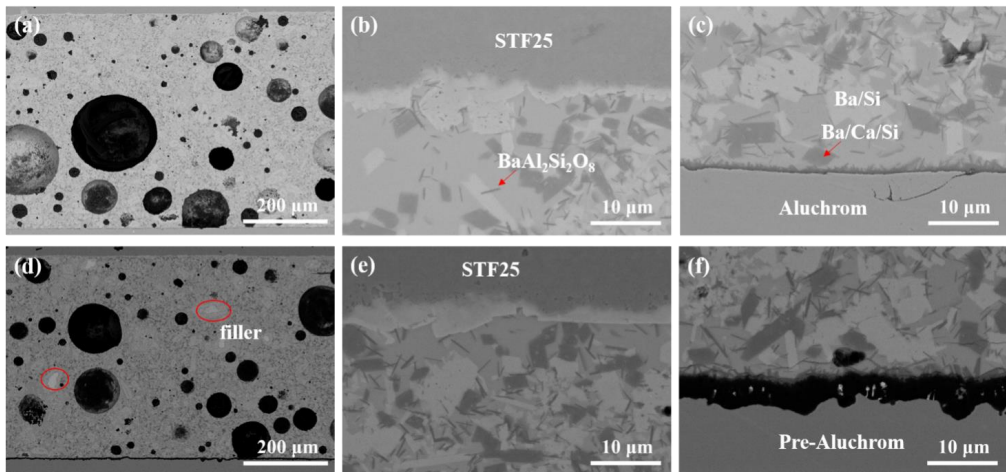
Fig. 4-39. Joints STF25/HBS30/Aluchrom (a-c) and STF25/HBS30/pre-oxidized Aluchrom (d-f); both joints jointed at 960 °C for 5 min.
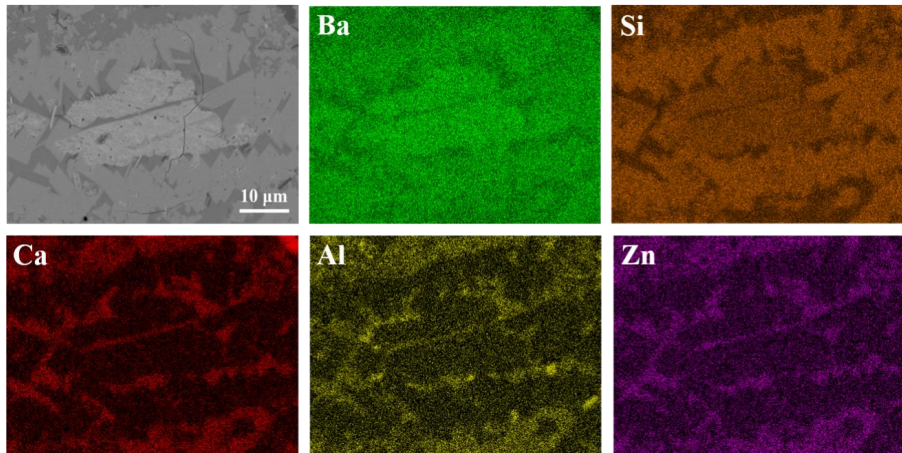
Fig. 4-40. SEM-EDS maps of the sealant HBS30 from STF25/HBS30/pre-Aluchrom joint
(960 °C, 5 min) for analyzing filler $BaSiO_3$
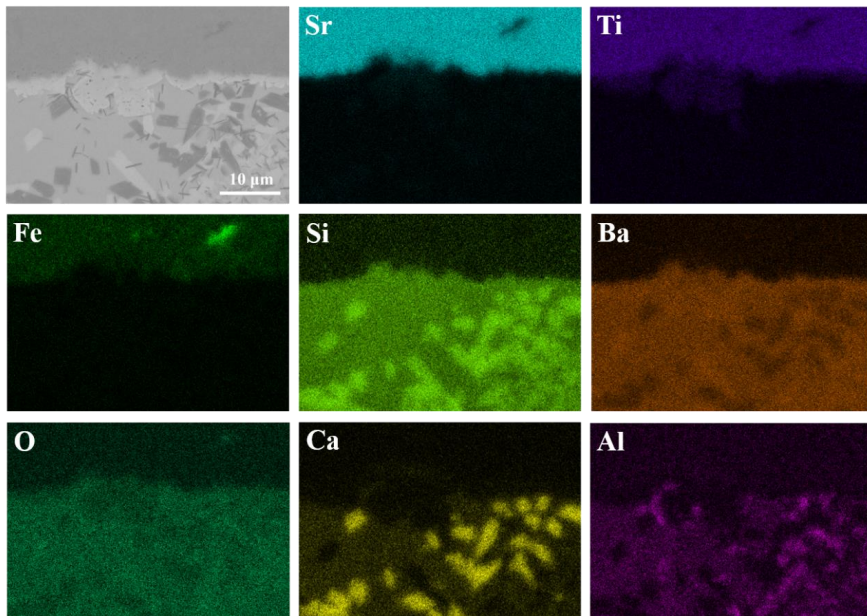
Fig. 4-41. SEM-EDS Trumaps of the joint STF25/HBS30/Aluchrom (960 °C, 5 min) for
analyzing diffusion layer of STF25 and HBS30

The analysis of interfaces between Aluchrom and the glass composite sealant HBS30 is shown in Fig. 4-42. A continuous thin oxidation layer with a thickness of around 0.3 µm connecting the glass composite seal and Aluchrom alloy was detected after the joining process at 960 °C for 5 min. In Fig. 4-43 the differences in heat-treatment of the support metals are visualized by line scans through the interface between sealant HBS30 and Aluchrom (a), and the sealant HBS30 and pre-oxidized Aluchrom (b). When comparing them, it is clear that the layer thickness of the pre-oxidized Aluchrom is much higher. From the two lines scans in Fig. 4-43, the scale is convinced by Al_2O_3 and formation followed by a thin interaction layer of Ba/Al/Si layer. Aluchrom formed the Al_2O_3 layer at high temperature [145], then the scale Al_2O_3 contacted with the glass sealant, and the Ba/Al/Si layer formed in situ because of elements diffusions. Nevertheless, both samples display a good adherence between the glass sealant and support metals, without crack or delamination.
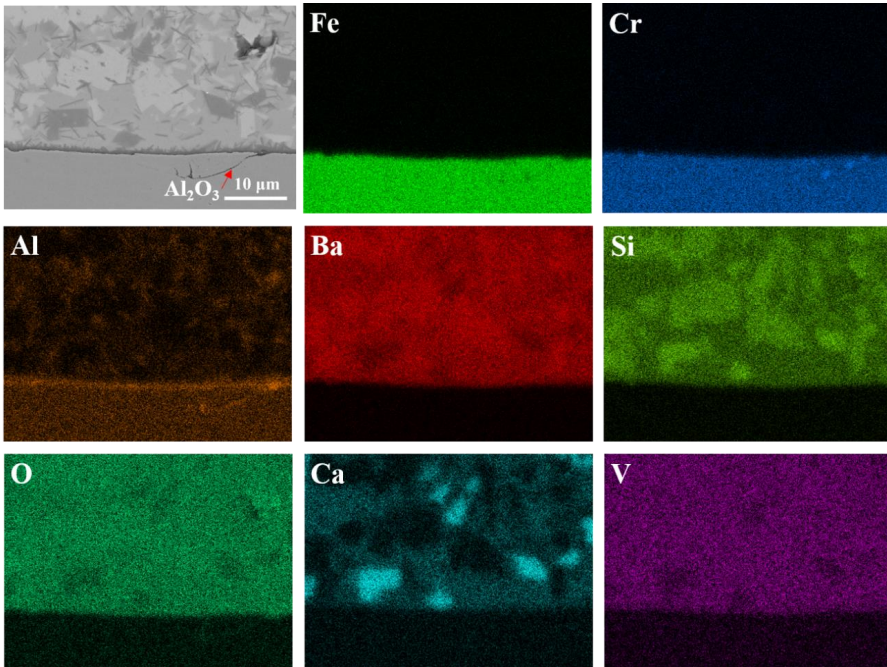
Fig. 4-42. SEM-EDS maps of the joint STF25/HBS30/Aluchrom (960 °C, 5 min) for analyzing diffusion layer of Aluchrom and HBS30
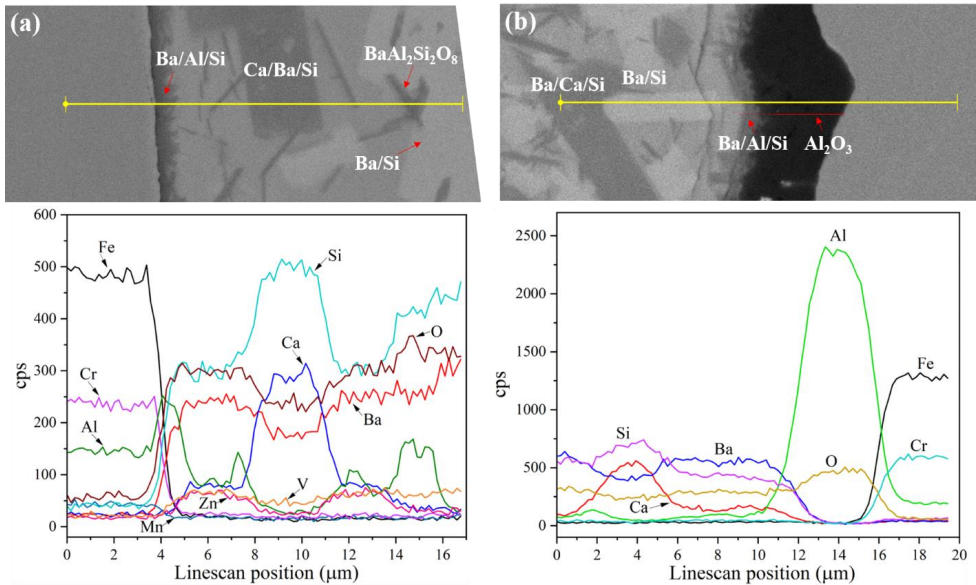
Fig. 4-43. Line scans through the interface between sealant HBS30 and Aluchrom (a), HBS30 and pre-oxidized Aluchrom (b), the samples joined at 960 °C for 5 min

Fig. 4-44 shows the microstructure of joint STF25/HBS30/Aluchrom joined at 920 °C for 15 min. HBS30 received good adhesion with STF25 and Aluchrom. Some pores agglomerated to large sized pores in sealant at joining temperature 920 °C. There are many pores formed in the sealant HBS30 with none round shape comparing with the sealant microstructure joined at 960 °C for 5 min. This may be caused by joining temperature and too high viscosity of the composite. The glass matrix has better viscous flow at higher joining temperature resulting in better wetting of the filler particles and allowing pores to collapse.
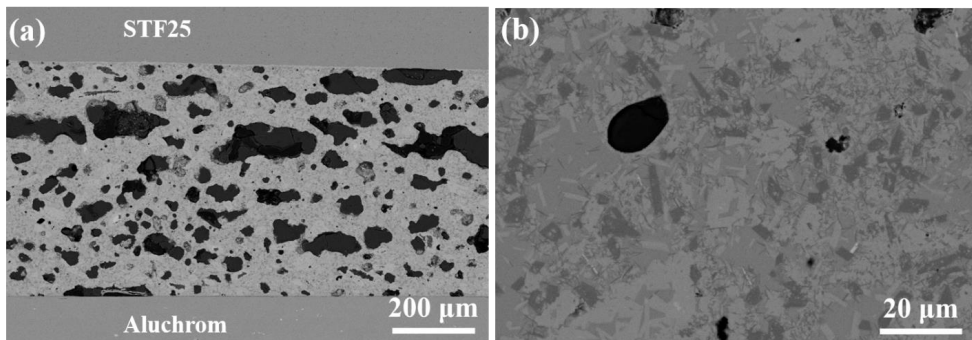
Fig. 4-44. Joint STF25/HBS30/Aluchrom joined at 920 °C for 15 min

4.4.8 Summary

In this study, $BaSiO_3$ was added as filler material into the glass matrix H with varying amounts of 10-30 wt.%. The CTE improved with increasing filler content. The composite with reinforcement of 30 wt.% $BaSiO_3$ resulted in the highest mean CTE values: as-sintered sample 10.7×10^{-6} K^{-1} and 9.6×10^{-6} K^{-1} after annealing. According to the viscosity behavior measured by HSM, the optimal joining temperature of HBS30 glass-ceramic sealant is assumed to be around 920 – 960 °C. The joining behaviors were investigated by comparing three joining temperatures 850 °C, 920 °C and 960 °C by means of Helium leakage test, CT and SEM-EDS. Sealing performance of HBS30 sealant with different counterparts, Crofer22APU, Aluchrom and pre-oxidized Aluchrom were detected by Helium leakage test. The setups joined at 850 °C for 10 hours failed for all support metals. High temperature joined samples under 960 °C or 920 °C obtained helium leakage values lower than 10^{-9} mbar·l·s^{-1}. Pore agglomeration was detected by the means of CT for the joint STF25/HBS30/Aluchrom joined at 960 °C. The joining process at lower temperature 920 °C presented smooth and less pores in the joining layer. The cross-sections of the joints were analysed by SEM and EDS. The samples joined with HBS30 showed good gas-tightness and sealing behaviors with STF25 and support metals (Aluchrom and pre-oxidized Aluchrom). The membrane side with a glass composite sealant formed an interdiffusion layer with Ba/Sr/Ti/Si elements. On the support metal side, pre-oxidized Aluchrom has shown a thick oxidation Al_2O_3 layer followed of a Ba/Al/Si layer. In comparison, Aluchrom formed in-situ a Ba/Al/Si layer during the joining process without reaching the equilibrium of Al_2O_3 formation. Both samples display good joining behavior between the glass sealant and support metals. It reveals that joining at 920 °C is the more suitable joining process for HBS30 composite sealant.

4.5 Ceramic Sr₂SiO₄ reinforced glass composite sealants

4.5.1 General remark

The only shortcoming of glass H is the relatively low thermal expansion coefficient (CTE) comparing with membrane materials STF25. Adding filler materials with higher thermal expansion coefficient into the glass matrix is a feasible strategy for improving the CTE of glass H (9.6×10^{-6} K^{-1}) in order to obtain matchable thermal expansion coefficients (around 12×10^{-6} K^{-1}) with membrane and the counterpart [109].

The properties of glass-based sealants can be tailored for OTM sealing through filler addition [13, 151]. All studied strontium silicate (Sr_2SiO_4) exhibit CTE (12.8×10^{-6} K^{-1}) [80] in a range suitable for components of sealing materials in high temperature oxygen transport membranes, that means if the respective crystalline phases reinforcement is combined with other crystalline or amorphous phases, an appropriate CTE can be adjusted. Moreover, the diffusion at the interface between the glass sealant and the membrane STF25 can possibly be reduced by the reduction in chemical gradient between the components [77] as the filler has the same element Sr as the membrane material STF25. When Sr_2SiO_4 fillers are added to the glass H matrix, good compatibility with the other components of the STF25 membrane stack and suitable thermal expansion can be expected to this glass-ceramic composite sealant.

In this study, filler material Sr_2SiO_4 was synthesized and added into glass H in order to adjust the CTE of the composites by changing the amount of the Sr_2SiO_4 additive. Viscous deformation behavior of glass composite was examined by means of hot stage microscope (HSM) to investigate viscous flow behavior and optimum temperature for joining OTM application. In the end, the effects of joining temperature on glass composite sealant joining behavior were investigated by gas leakage measurement and microstructural analysis with scanning electron microscopy (SEM) on the cross sections of the joints with STF25 membrane and Aluchrom plate.

4.5.2 XRD analysis for Sr₂SiO₄

Fig. 4-45 shows the XRD-pattern of strontium silicate Sr_2SiO_4 filler powder synthesized at 1350 °C for 30 h. One can see that Sr_2SiO_4 has been identified to exist in the allotropy phases with different symmetries, monoclinic (ICDD: 01-076-1630) and orthorhombic (ICDD: 01-076-1494). Residues form quartz (sea sand) and $SrCO_3$ could not be detected. Strontium silicate Sr_2SiO_4 filler was got as the reaction anticipated (e.2).

$$2SrCO_3 + SiO_2 \xrightarrow[t=30\,h]{T=1350\,°C} Sr_2SiO_4 + 2CO_2 \uparrow \qquad (e.2)$$
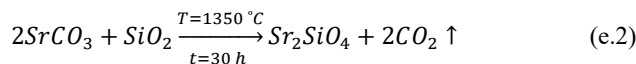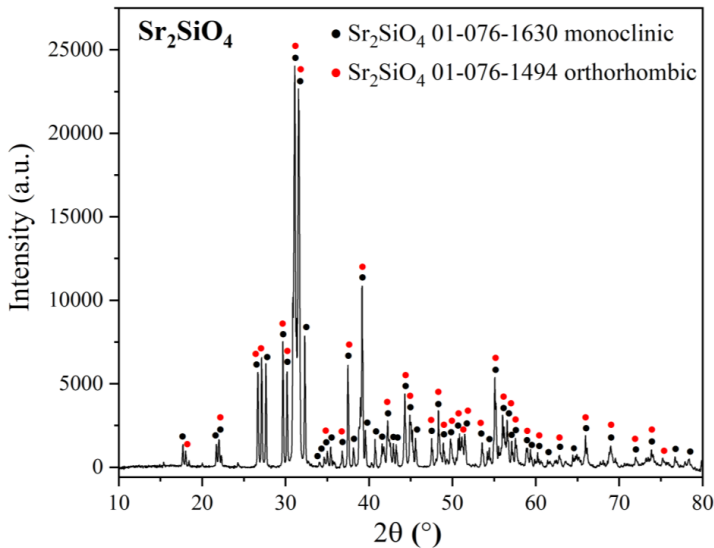
Fig. 4-45. XRD pattern of the synthesized Sr_2SiO_4 filler (1350 °C for 30 h)

4.5.3 The effect of Sr_2SiO_4 filler amount on thermal expansion behavior and microstructure of glass-based sealant

Dilatometer measurements were performed for the glass ceramic composites, HS2S10, HS2S20, HS2S30, and HS2S40. The dilatometer bars of composites were pressed and sintered at 850 °C for 10 h. Half of the bars were additionally annealed at 800 °C for 1000 h. The thermal dilatometric results of the sintered and annealed composites are shown in Fig. 4-46. The CTE curves of the sintered composites with Sr_2SiO_4 fillers (Fig. 4-46 a) obtained a transformation temperature (T_g) of around 625 °C which coincides with the DSC results measured for pure glass H. The sintered samples reinforced by Sr_2SiO_4 received higher CTE values than pure glass H (see Table 4-11). The CTE value of the annealed samples decreased comparing to the as sintered composites shown in Fig. 8-2 (b), whereas CTE values improved with the filler material amount increased. The addition of 20 wt.% Sr_2SiO_4 resulted in the highest CTE values of up to $11.7 \times 10^{-6}\,K^{-1}$ for as-sintered sample and the addition of 40 wt.% Sr_2SiO_4 got the highest CTE up to $10.9 \times 10^{-6}\,K^{-1}$ after annealing, respectively, measured in a temperature range between 200 °C and 900 °C (see Table 4-11).
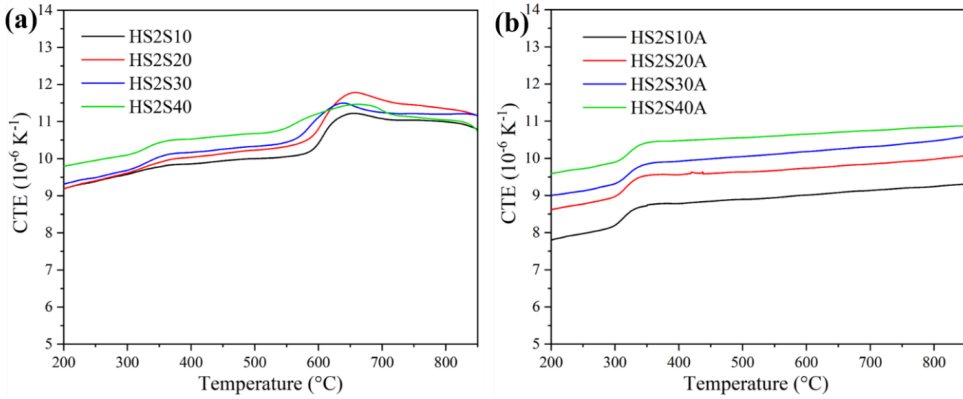
Fig. 4-46. CTE curves for composites samples sintered (a) and annealed (b)

Table 4-11. Thermal expansion coefficients (as sintered and long-term annealed) of the glass H and glass ceramic composite sealants

Sample	CTE [$\times 10^{-6}$ K^{-1}] (200 – 850 °C)	Annealed sample	CTE [$\times 10^{-6}$ K^{-1}] (200 – 850 °C)
Glass H	8.5-10.8	HA	8.0-9.6
HS2S10	9.2-11.2	HS2S10A	7.9-9.3
HS2S20	9.2-11.7	HS2S20A	8.7-10.1
HS2S30	9.3-11.5	HS2S30A	9.0-10.6
HS2S40	9.8-11.5	HS2S40A	9.6-10.9

To explore the microstructure features of sealing glass-based composites reinforced with different Sr_2SiO_4, SEM analysis was performed on the annealed samples, as shown in Fig. 4-47. Microstructures of these composites were influenced by the amount of the Sr_2SiO_4 additive. In the case of the composites with 20 – 30 wt.% Sr_2SiO_4 additive, homogeneous, dense structure and close pores were observed. However, a lot of large irregular pores were observed in the composite with 40 wt.% Sr_2SiO_4 reinforcement. The glass cannot completely wrap the fillers by viscous flow during sintering, when the content of the filler in the composite material is 40 wt.% (Fig. 4-47 d). When the filler amount is too high, the probability of the formation of open pores increases and fully densified materials can hardly be obtained, which would lead to gas leakage used in OTM module. Fig. 4-48 shows SEM-EDS maps of the HS2S20A sample. The filler Sr_2SiO_4 is in chrysanthemum-shape. The needle like phase was determined to be $BaAl_2Si_2O_8$ [13, 94] formed from glass H during heating, which agrees with XRD crystallization analysis and FactSage simulation of the composition of glass H.
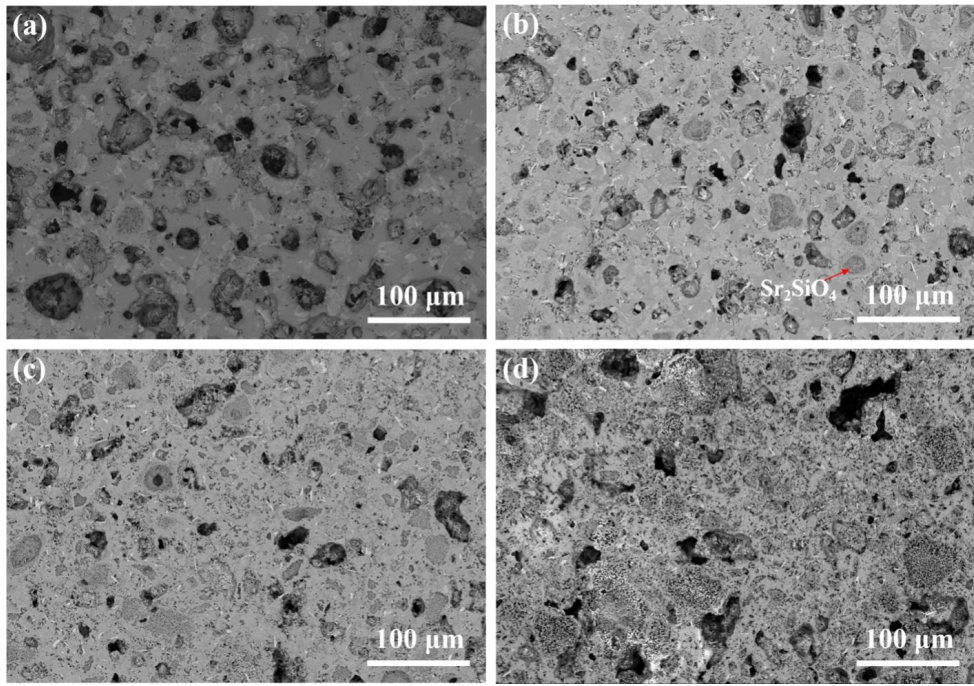
Fig. 4-47. SEM-EDS analyses of annealed composites (a) HS2S10A, (b) HS2S20A, (c) HS2S30A, (d) HS2S40A
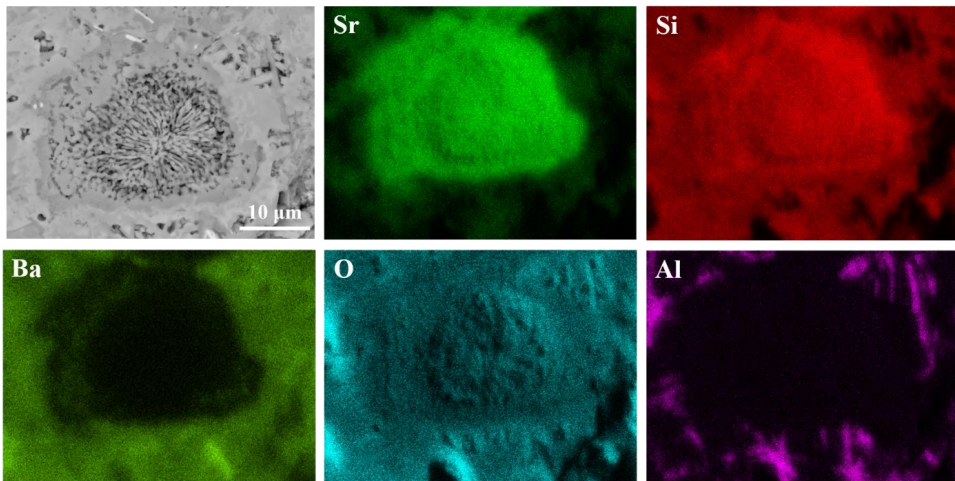
Fig. 4-48. SEM-EDS maps of the HS2S20A sample

4.5.4 Shrinkage and viscous behavior investigation on Sr_2SiO_4 glass sealant

The reinforced composite HS2S20 was examined by means of HSM to investigate viscous deformation behavior and optimum temperature for joining OTM application, as seen in Fig. 4-49. Fig. 4-49 (b) summarizes the shadow images at the fixed viscosity temperature values (T_{FS}, T_{MS}, T_D, T_S, T_{HB} and T_F). From the shrinkage behavior, the optimal joining temperature of HS2S20 glass-ceramic sealant is assumed to be around maximum expansion peaks height and area variation ratio curves and sphere temperature (T_s) 957 °C, between 920 °C – 960 °C.

The method proposed by Pascual et al. [73] was adopted to predict the viscosity-temperature data of the glass-ceramic sealant HS2S20 based on hot stage microscopy (TOMMIplus). The viscosity-temperature data of HS2S20 were compared with pure glass matrix H [82] as seen in the Table 4-12. Around typical joining temperature 850 °C, glass H is at forming half ball stage, but adding 20 wt.% Sr_4SiO_4 composite HS2S20 is just in the deformation range. The addition of ceramic fillers could reduce the creep behavior of sealant at high temperature. Fig. 4-50 shows the fitting lines of the two viscosity-temperature data, which could provide the possibility to predict the viscosity of the glass-based sealants. Moreover, it was evidently to see that the addition of ceramic filler Sr_2SiO_4 caused an increase in the viscosity and the fixed viscosity temperature of the glass sealant with the temperature.
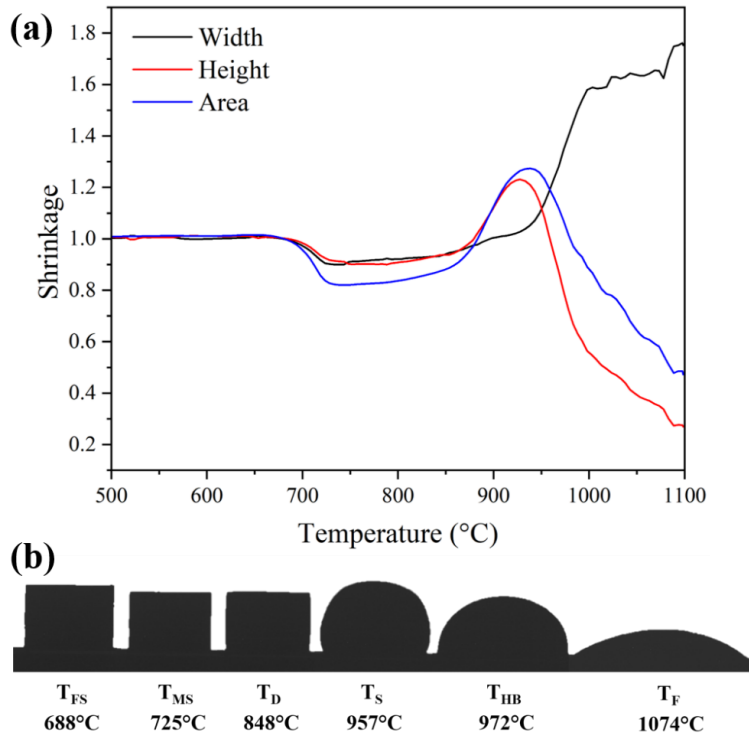
Fig. 4-49. HSM analysis (TOMMIplus) for HS2S20 glass composite sealant on Crofer 22 APU substrate recorded at 5 °C/min, (a) shrinkage curves, (b) Shadow images of the sample at the fixed temperature

Table 4-12. Fixed viscosity temperatures of pure glass H [82] and glass H reinforced composite HS2S20

Sample	Fixed viscosity (log η) [73], (η, dPa·s)					
	9.1	7.8	6.3	5.4	4.1	3.4
	Temperature (°C)					
	T_{FS}	T_{MS}	T_D	T_S	T_{HB}	T_F
Glass H [82]	610	725	730	795	844	-----
HS2S20	688	728	848	957	972	1074
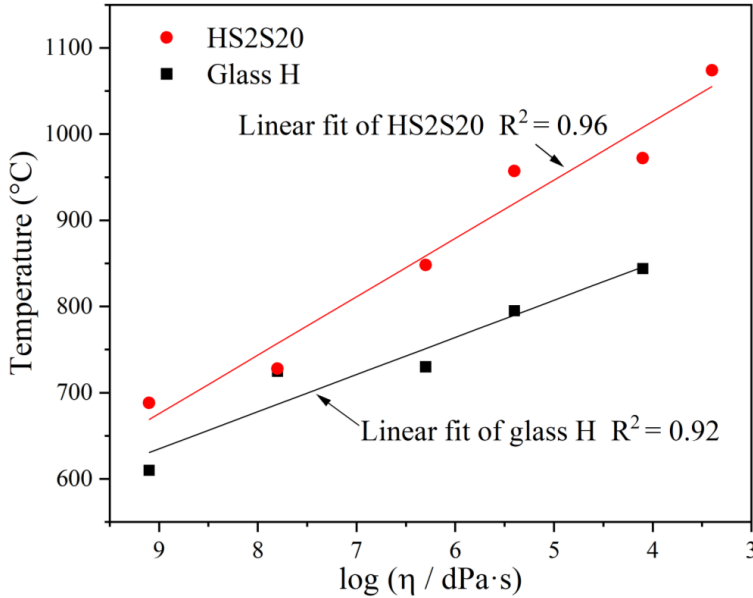
Fig. 4-50. Viscosity-temperature curves of glass H and composite sealant HS2S20

4.5.5 Joining behavior of Sr$_2$SiO$_4$ reinforced glass composite sealant

4.5.5.1 Gas tightness

The gas-tightness results of samples joined under different thermal processes by HS2S20 glass composite are summarized in Table 8-3. 850 °C is the typical joining temperature used in SOFC glass-sealing. 920 °C and 960 °C were chosen according to the above HSM analysis. The setup joined at 850 °C for 10 hours showed leakage under 800 g deadload. Another three symmetrical setups joined at different temperatures and adequate deadload exhibit low helium leakage values lower than the detection limit of 10^{-9} mbar·l·s^{-1}, which will fulfill the requirements for the high temperature operation of the OTM module [143]. Besides, the hermetic samples sealed with glass-ceramic sealant HS2S20 under different joining processes received the same joining gap around 0.3 mm. In the case of the same sealing material, the sealing process is affected by temperature, pressure and dwell time. Choosing the correct temperature and pressure are key factors for sealing success. In general, under elevated temperature glass sealants have better flow properties and good wetting behavior with the counterparts as seen from the HSM profiles Fig. 8-5 (b), so in order to obtain same sealing result, longer dwell time and higher dead load were adopted and adjusted for HS2S20 gas-tightness setup.

Table 4-13. Gas tightness measurements on samples sealed by HS2S20 sealant under different joining processes

Joining process	Dead load	Gas tightness mbar·l·s^{-1}	Joining gap
850 °C, 10 h	800 g	leakage	---
850 °C, 10 h	1200g	<10^{-9}	0.3 mm
920 °C, 15 min	800g	<10^{-9}	0.3 mm
960 °C, 10 min	520g	<10^{-9}	0.3 mm

4.5.5.2 Microstructure of assembled joints

In order to simulate the joining behavior of sealant in the OTM stack, HS2S20 sealant was assembled in between membrane STF25 and Aluchrom plate, and the joints heated under different processes: 960 °C 10 min, 920 °C 15 min, 850 °C 10 h.

Fig. 4-51 presents the microstructures of the joint STF25/HS2S20/Aluchrom joining at 960 °C for 10 min. There are some big sized pores formed in the sealant as seen Fig. 4-51 (a). The glass matrix exhibits a good viscous flow state around high temperature 960 °C, and at this time, the small pores in the sealant were easily in contact of each other and coagulate to large bubbles, some of which may be released under deadload, but some remained in the sealant as closed pores. The filler Sr_2SiO_4 particles could be found in the sealant, as marked in the Fig. 4-51 (b). The ceramic filler powders partially solved with glass matrix at high temperature 960 °C. One can see that Sr_2SiO_4 filler was covered by a corona which assumed to be a diffusion layer consisting of Ba/Sr/Ca/Si as analyzed by EDS in Fig. 4-52. The dark grey needle-shaped phase in the amorphous matrix was attributed to $BaSi_2Al_2O_8$ as seen the EDS analysis in Fig. 4-52, which agrees with XRD results and FactSage calculation (Fig 3 and 4). HS2S20 sealant exhibited good adhesion joining with the stack components Aluchrom and STF25 (Fig. 4-51 c and d). There is no crack or delamination at both interfaces.
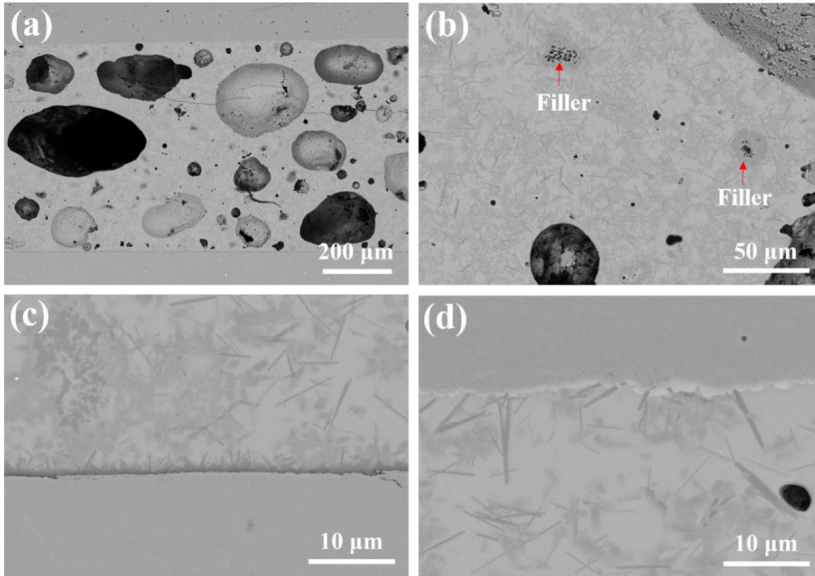
Fig. 4-51. SEM images of the cross-section of joint STF25/HS2S20/Aluchrom joining at 960 °C for 10 min with a 60 g dead load
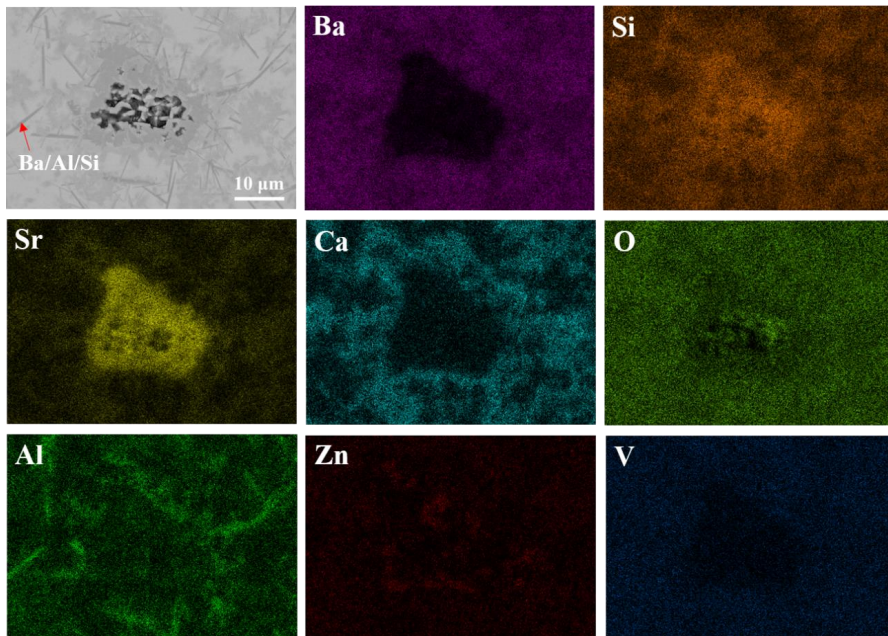
Fig. 4-52. SEM-EDS maps of the sealant HS2S20 from STF25/HS2S20/Aluchrom joint

Fig. 4-53 compares SEM images of the cross-sections of joints STF25/HS2S20/Aluchrom joined by different thermal processes: 920 °C 15 min (a, b), 850 °C 10 h (c-e). HS2S20 sealant joined at 920 °C for 15 min showed highly porous structure compared with the joints heated at 850 °C, because viscosity and strength of glass matrix are lower at high temperature and gas bubbles are easier to expand. The joint joined with HS2S20 at 920 °C shows crack free microstructure and good adhesion with membrane STF25 and counterpart Aluchrom.

Despite the stack joining at 850 °C showed no separation and was well connected with both Aluchrom and OTM before cutting and polishing, obvious cracks were found in the sealant. The sealant is the weakest and fragile part of the whole stack. In addition, the long-term dwell time makes the glass matrix precipitate more crystal phases, which indicates this joint (850 °C) is more fragile than the short time sintered samples. While, the sealant shows good adhesion with Aluchrom and STF25 at the interfaces joining at 850 °C. Besides, no covered corona has been observed around the filler Sr_2SiO_4 in the stack joined at relatively low temperature of 850 °C.

In summary, the joining performance of HS2S20 sealant joined at high temperature of 920 °C is more promising. The sealant joined at 960 °C causes problems of pores agglomeration and a high risk of leakage in further operation. The sealant jointed at 850 °C needs longer time to join Aluchrom and STF25 together and exhibited a higher chance of crystalline formation and fragile risk. The ceramic filler powders are partially solved in the glass matrix at 960 °C and 920 °C, and covered with a corona diffusion layer consisting of Ba/Sr/Ca/Si.
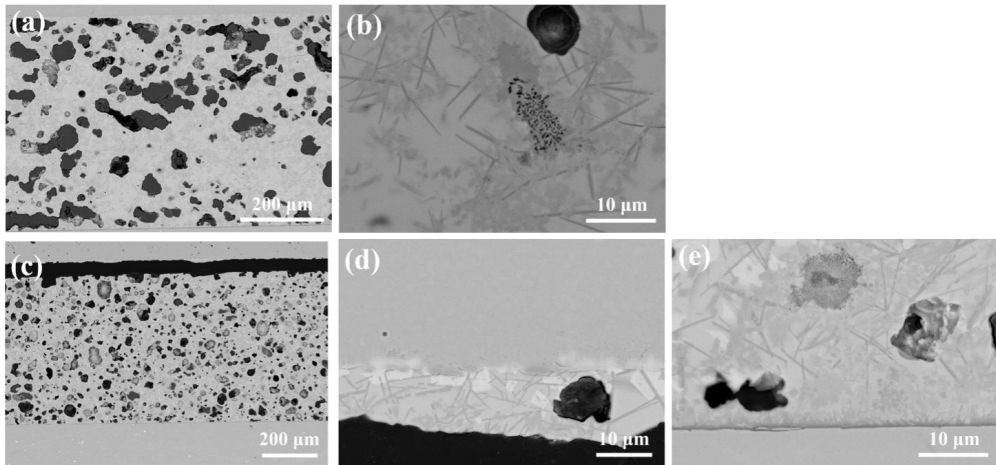
Fig. 4-53. SEM images of the cross-sections of joints STF25/HS2S20/Aluchrom, (a, b) joined at 920 °C for 15 min with a 100 g dead load, (c-e) joined at 850 °C for 10 h with a 150 g dead load

4.5.6 Summary

Sr_2SiO_4 was added 10 – 40 wt.% into the glass matrix H. The CTE improved with increasing filler content. The composite with 40 wt.% Sr_2SiO_4 reinforcement resulted in the highest mean CTE values: as-sintered sample 10.7×10^{-6} K^{-1} and 10.3×10^{-6} K^{-1} after annealing. The microstructures of these composites were strongly influenced by the amount of the additive. The composites with 20-30 wt.% Sr_2SiO_4 filler received homogeneous, dense structures. According to the shrinkage behavior measured by HSM, the optimal joining temperature of HS2S20 glass-ceramic sealant is assumed to be around 920 °C-960 °C. The joining behaviors were investigated by comparing three joining temperatures (850 °C, 920 °C, 960 °C). Excellent hermeticity with low helium leakage values below 10^{-9} mbar·l·s^{-1} was received for three symmetrical samples joined at different temperatures and adequate deadload respectively. Joining temperature and pressure are key factors for sealing success. Good joining behavior was observed in the sample STF25/HS2S20/Aluchrom after joining at 960 °C compared with the other two samples joined at lower temperatures. Some big pores formed in the sealant which are attributed to glass viscous flow at high temperature and agglomeration of small pores. The ceramic filler powders partially dissolved in the glass matrix at 960 °C and were covered with a corona diffusion layer consisting of Ba/Sr/Ca/Si.

4.6 New Ba-Sr-Si-B glass sealant development

4.6.1 Principle idea of new glass development

Glass sealants are excellent candidates for joining materials due to their heat resistance, tunable composition and properties, and good sealing behavior at OTM operation environment (> 700 °C) [91]. Silva et al. [96] investigated BaO–Al$_2$O$_3$–SiO$_2$ glasses modified with B$_2$O$_3$ and reported that a BaAl$_2$Si$_2$O$_8$ phase was formed after heat treatment at 850 °C. Brendt et al. [94] and Borhan et al. [83] also reported that the same phenomenon was found in barium aluminosilicate system glasses after heat treatment. The addition of Al$_2$O$_3$ to glasses causes the formation of undesirable low CTE phase BaAl$_2$Si$_2$O$_8$, which would cause a mismatch when joining the glass sealant. Due to this problem, many compositions of glass sealants without Al$_2$O$_3$ have been investigated [152]. Rezazadeh et al. [153] fabricated SiO$_2$–B$_2$O$_3$–BaO system glasses with a decent CTE of up to 12.6×10^{-6} K^{-1}, and barium silicate crystalline phases were formed after heat treatment. If a glass sealant includes the same element, Sr, as the STF25 membrane material, it can be expected to reduce diffusion at the interface between the glass sealant and the STF25 membrane through a reduction in the chemical gradient between the components [77], while their chemical compatibility could be improved. Some strontium silicate phases also have a decent CTE, such as SrSiO$_3$ (11.4×10^{-6} K^{-1}) and Sr$_2$SiO$_4$ (12.8×10^{-6} K^{-1}) [80]. Kim et al. [154] reported SrO–SiO$_2$–B$_2$O$_3$ glass with a CTE of around 9.2×10^{-6} K^{-1}. Literature values of barium silicate phases are reported to have a relatively high CTE, such as BaSi$_2$O$_5$: 14.1×10^{-6} K^{-1} [155], Ba$_2$Si$_3$O$_8$: 12.6×10^{-6} K^{-1} [155], and Ba$_5$Si$_8$O$_{21}$: 14.5×10^{-6} K^{-1} [79]. Zhang et al. [131] found that the low CTE phase SrB$_2$O$_4$ (8.5×10^{-6} K^{-1}) was formed when borate content is higher than or equal to 30 mol% in on Sr–Ba-borosilicate glasses. The focus of this work is to investigate the effect of SrO on BaO–SrO–SiO$_2$–B$_2$O$_3$-based (BS) glasses, with the hope of obtaining desirable crystalline phases such as barium silicates, strontium silicates, or Ba–Sr silicate compounds. Moreover, the glass-forming tendency is related to the critical cooling rate and the ability against devitrification. A glass with a higher glass-forming tendency means glass is easily fabricated with a small cooling rate, for example free cooling in air, and prevents volume crystallization during cooling [134]. Hrubý measured the glass-forming tendency parameter by calculating the relation of the onset crystallization temperature (T_r), the glass transition temperature (T_g), and the onset melting temperature (T_m) [112].

In this work, three BS glasses with different SrO contents were fabricated using the melt-quenching method, and the effect of SrO on the glass-forming tendency, thermal properties, crystallization, and joining behavior was investigated. Differential scanning calorimetry (DSC) measurements were performed to determine the glass formation ability of each BS glass. The thermal expansion coefficients of BS glass were measured to investigate the effect of Sr concentration on the thermal properties of BS glasses. The microstructures of annealed samples were investigated by scanning electron microscopy (SEM) and energy-dispersive X-ray analysis spectroscopy (EDS). In addition, crystalline phases of BS glasses after heat treatment at 850 °C were investigated by X-ray powder diffraction and their influence on the thermal expansion coefficient was discussed. Finally, the

joining ability of BS glasses was assessed by sinking dilatometer, hot stage microscopy (TOMMIplus) measurements, helium leak testing, and joining with the STF25 membrane.

4.6.2 Glass forming tendency evaluation

Fig. 4-54 (a-c) shows the results of DSC, which was carried out on the quenched glasses BS6, BS15, and BS25 to characterize their thermophysical properties. From the DSC curves, it is possible to determine the characteristic temperatures of BS glasses, such as T_g, T_r, exothermic peak temperature of crystallization (T_p), melting onset temperature (T_m), and endothermic melting peak temperature (T_{mp}), all of which are summarized in Table 9-1. Fig. 4-54 (d) shows the DSC magnification curves of BS glasses between 500 °C and 800 °C for better visualization of the glass transition temperature (T_g) and crystallization onset temperature (T_r). The T_g values of the BS glasses decrease with increasing strontia content from 637 °C to 581 °C. Similar findings in the literature on the decline of T_g was explained by the formation of non-bridging oxygens [156]. Moreover, T_r and T_p values decrease with increasing SrO content in BS glasses, which means that BS25 glass has a lower activation energy for crystallization when heating. The BS6 and BS15 glasses have only one distinct exothermal crystallization peak T_p at 778 °C and 741 °C, respectively. In contrast, the BS25 DSC curve exhibited four crystalline peaks at 717 °C, 755 °C, 904 °C, and 1031 °C, which means that four different crystalline structures would originate before reaching melting temperature. With the measuring temperature rising, BS glasses start to melt. Glass does not have a fixed melting point, but a melting process that continuously absorbs heat. The position of the maximum endothermic peak T_{mp} can be determined. Firstly, the T_{mp} of BS15 is at 1071°C. Subsequently, the T_{mp} of BS6 is at 1127 °C and BS25 T_{mp} is close to BS6 at around 1133 °C

From the DSC data, the glass-forming tendency and glass thermal stability of each BS glass were evaluated on the basis of the relative onset temperatures of the T_g, T_r, and T_m, which were calculated using the equations proposed by Hrubý (K_{gl}) in 1972 [112]:

$$K_{gl} = \frac{T_r - T_g}{T_m - T_r} \tag{1}$$

Table 4-14 presents the corresponding K_{gl} values of BS glasses. BS15 has the largest K_{gl} value (0.26), which is close to that of BS6 (0.25). BS6 and BS15 show better resistance against devitrification. $0.20 \leq K_{gl} \leq 0.26$ means that all the BS glasses can be easily prepared under a cooling rate of around 15 °C/min. BS glasses are still in a glassy state after a DSC measurement cooling procedure of 15 °C/min (as shown in Fig. 4-55), which verifies the above conclusion using the Hrubý equation (1). BS15 has the best glass-forming tendency and thermal stability in three BS glasses according to the K_{gl} calculation.

Table 4-14. DSC data, K_{gl} of BS glasses

Sample	T_g (°C)	T_r (°C)	T_p (°C)	T_m (°C)	T_{mp} (°C)	K_{gl}
BS6	637	725	778	1083	1127	0.25
BS15	616	700	741	1022	1071	0.26
BS25	581	668	717	1113	1133	0.20
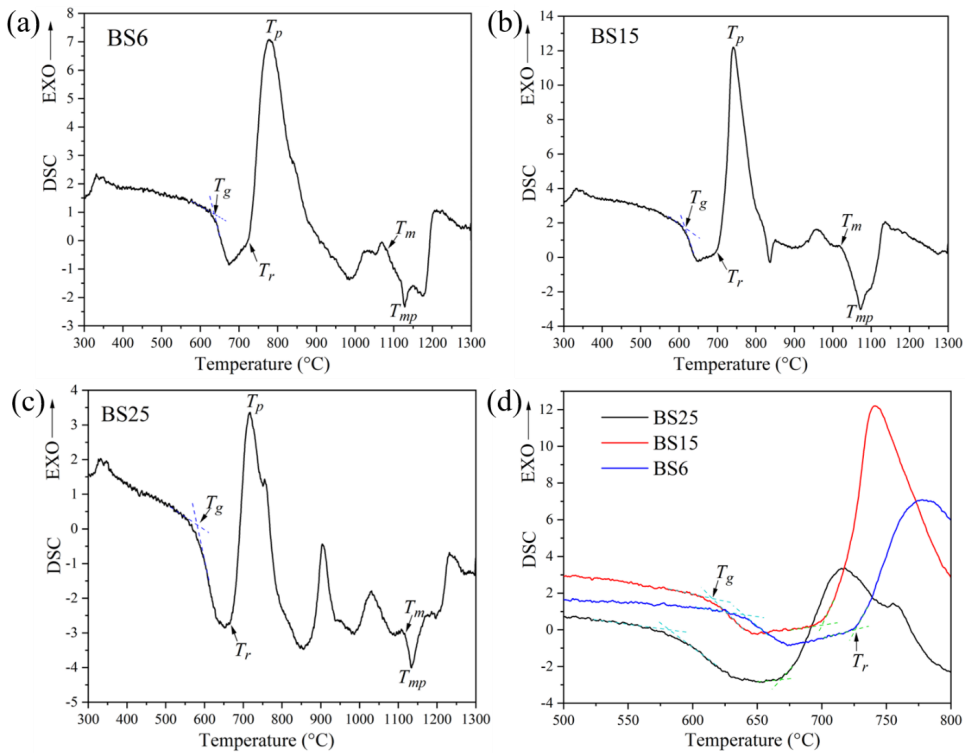
Fig. 4-54. DSC curves of BS glasses at a heating rate of 15 °C/min, (a) BS6, (b) BS15, (c) BS25, (d) magnification of DSC curves between 500 – 800 °C for clear marking T_g and T_r

Fig. 4-55. DSC crucibles of BS glasses (cooling rate 15 °C/min)

4.6.3 Thermal expansion behavior of BS glasses

The coefficients of thermal expansion (CTEs) of BS glasses were measured using a dilatometer with rods sintered at 900 °C for 1 h. The results are presented in Fig. 4-56 as (a) elongation plots and (b) calculated CTE values of BS glasses as a function of temperature in comparison with the STF25 membrane and the Aluchrom support metal. Elongation and CTE curves of BS glasses increased with rising temperature and decreased with an increasing concentration of Sr. In contrast, the dilatometric softening temperature (T_s) of BS glasses rises with increasing Sr concentration – from 835 °C for BS6 glass to 886 °C for BS25 glass. As the dilatometric softening temperature of all BS glasses is higher than 835 °C, BS glasses should be ideal for use as high-temperature sealants. The respective CTE values in the temperature range from 200 °C to 850 °C as well as the dilatometric softening temperature of the glasses BS are summarized in Table 3. BS6 resulted in the highest CTE value (up to 14.5×10^{-6} K^{-1}) compared with BS15 and BS25, even higher than the CTE of the STF25 membrane ($10.7 – 13.1 \times 10^{-6}$ K^{-1}). The CTE plot of Aluchrom intersects with the BS6 curve at 617 °C, and the CTE value of BS6 is higher than Aluchrom in the range of 617–855 °C. The step increasing of the CTE of BS6 at 600 °C is due to the typical change of property at the glass transition zone. The steep decrease in the CTE of BS6 after 810 °C can be attributed to the initial softening of the dilatometric glass rod. A similar phenomenon was also observed for BS15 and BS25. The CTEs of the BS15 ($10.4 – 11.9 \times 10^{-6}$ K^{-1}) and BS25 ($9.9 – 10.9 \times 10^{-6}$ K^{-1}) glasses were slightly lower than Aluchrom ($11.4 – 13.8 \times 10^{-6}$ K^{-1}) and STF25. The coefficient of thermal expansion decreases with the increasing SrO content of the BS glasses. This finding was expected, since the substitution of the network modifier BaO as the bigger cation with SrO as the smaller cation in a composition produces a smaller CTE in silicate glasses [152].

Figure 4-56 (c) presents the dilatometer curves of the annealed BS glass samples after thermal treatment at 850 °C for 50 h. The annealed samples exhibited highly ceramic behavior of the material, as no glass transition point T_g is visible. Moreover, the CTE of the annealed samples decreases with increasing strontium, which is in accordance with the regularity of measurement of short-term sintered BS glasses. The CTE values of the annealed samples decreased slightly when compared to the BS glasses sintered at 900 °C for 1 h. A comparison of expansion values is given in Table 4-15. The decrease of CTE is likely a result of the formation of low CTE phases, which is

the reason for the detailed investigation of the crystallization behavior carried out in the following by SEM and XRD analyses. The cross sections of the annealed BS dilatometry specimens are depicted in Fig. 4-57. The annealed BS15 specimen shows the highest compaction with a dense microstructure and minimal porosity compared to BS6 and BS25. When comparing the differences, there are some crystalline phases precipitated from BS glasses after annealing. An EDS elemental mapping of BS6 is presented in Fig. 4-58. It is hard to distinguish between the phases in the EDS mapping. The crystallization behavior of the annealed samples at 850 °C for 50 h is analyzed by XRD in section 4.6.4.
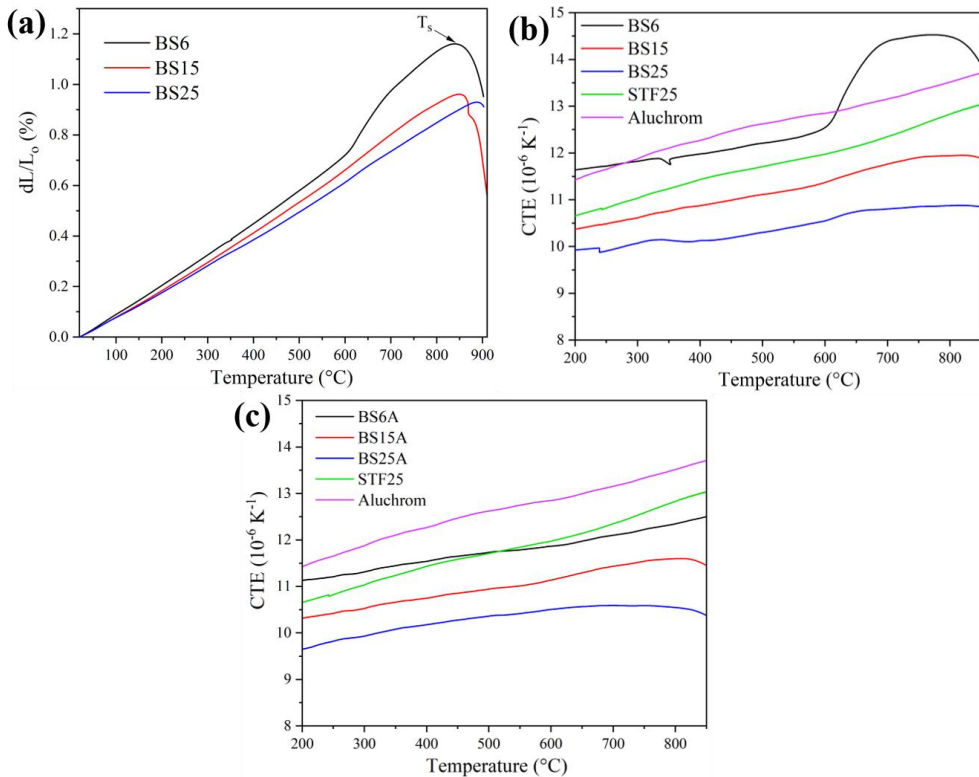
Fig. 4-56. Dilatometer curves of BS glasses, (a) elongation plots, dilatometer softening temperature (T_s), (b) CTE of BS glasses as a function of temperature comparing with membrane STF25 and Aluchrom, (c) dilatometer curves of the annealed BS samples after 850 °C for 50 h

Table 4-15. Thermal properties of BS glasses

Sample	T_s (°C)	CTE (10^{-6} K^{-1}) (200 – 850 °C) sintered	CTE (10^{-6} K^{-1}) (200 – 850 °C) annealed
BS6	835	11.6-14.5	11.1-12.5
BS15	846	10.4-11.9	10.3-11.6
BS25	886	9.9-10.9	9.7-10.6
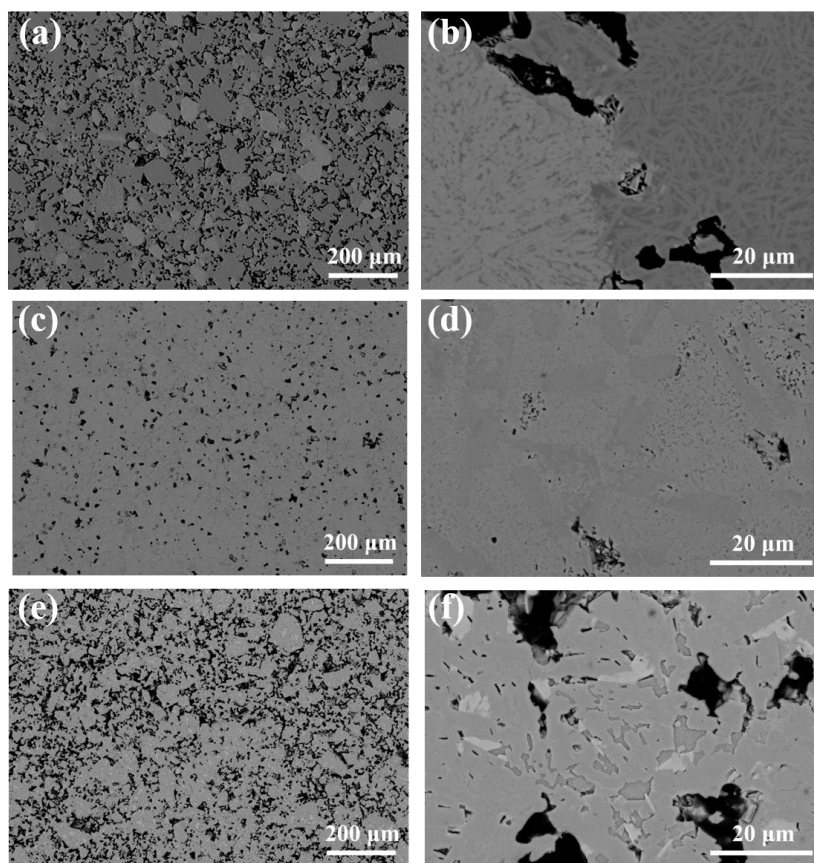
Fig. 4-57. SEM-EDS analyses for the annealed dilatometer samples (a, b) BS6A, (c, d) BS15A, (e, f) BS25A; overview on the left and magnification on the right
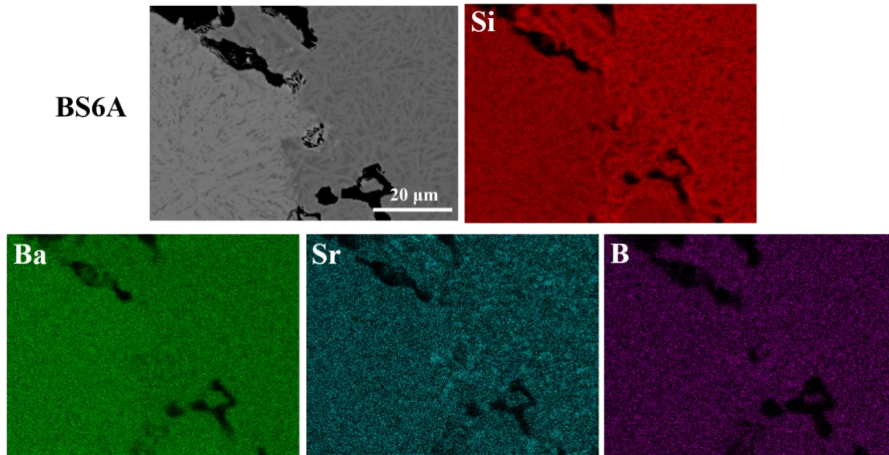
Fig. 4-58. EDS maps of the annealed sample BS6A after sintering at 900 °C for 1 h and thermal treatment at 850 °C for 50 h

4.6.4 Crystallization analysis of BS glasses

All three BS glasses were heated at 850 °C for 50 h, and XRD analysis was carried out in order to investigate phase formation and to analyze their possible influence on the thermal expansion coefficient. The XRD patterns of the BS glasses are shown in Fig. 4-59. The main crystalline phases precipitated in the heated BS6 glass (Fig. 4-59 a) were two binary barium silicates ($BaSi_2O_5$ and $Ba_5Si_8O_{21}$) and a ternary barium strontium silicate ($BaSrSi_3O_8$), while tiny amounts of low quartz (α-SiO_2) were also present after heat treatment at 850 °C. Similar crystalline behavior was observed for the BS15 glass in Fig. 4-59 (b). The phases present after heat treatment of the BS15 sample were $Ba_5SrSi_{10}O_{26}$, $Ba_2Si_3O_8$ $Ba_2SrB_6O_{12}$, and tridymite. Barium strontium boride ($Ba_{1.84}Sr_{1.16}$) $(B_3O_6)_2$, SrO, and α-SiO_2 precipitated in BS25 glass (Fig. 4-59 c).

We listed crystallographic information of polymorphism SiO_2 phases formed in BS glasses in Table 4-16. BS6 and BS25 glasses formed same low quartz phase in principle, even though they have different PDF cards. Low quartz (α-SiO_2) and syn low quartz have the same crystal structure, space group and space group number. Hexagonal tridymite was identified in the annealed BS15, which is a high temperature phase comparing with low quartz. From literature, pure tridymite is formed and stable at high temperatures between 867-1470 °C [157]. In complex system such as glass-ceramic [158] and kaolin [159], tridymite formation was observed beginning at 600 °C.

Binary Ba/Si phases have relatively high thermal expansion coefficients, which are reported to be $BaSi_2O_5$: 14.1×10^{-6} K^{-1} [155], $Ba_2Si_3O_8$: 12.6×10^{-6} K^{-1} [155], and $Ba_5Si_8O_{21}$: 14.5×10^{-6} K^{-1} [79]. In contrast, the binary Sr/Si phases have a comparably lower CTE than the Ba/Si compounds, such

as $SrSiO_3$: 11.2×10^{-6} K^{-1} [80]. Ternary Ba/Sr silicates were formed and a small amount of SiO_2 (α-SiO_2: 10.5×10^{-6} K^{-1} [160], tridymite: $10 - 4 \times 10^{-6}$ K^{-1} [161]) with lower CTE values was found for all of the BS glasses after heat treatment at 850 °C, which would decrease thermal expansion property of the sealants.

These findings could explain the slight decrease of the CTE values of BS glasses after annealing at 850 °C, as shown in the dilatometer curves of Fig. 4-56 (c). Barium silicate phases, barium–strontium silicate phases, and strontium silicate phases are desirable phases in crystallized BS-based glass due to their relatively high CTE values, which might enable the sealing of OTM components such as Aluchrom and STF25. With the increase in SrO content in BS glasses, Sr^{2+} replaces Ba^{2+} in some cases, which is why some Ba/Sr compounds were formed in three BS glasses after heat treatment at 850 °C, such as barium strontium silicates and barium strontium borides. It is worth noting that the formation of borate-containing crystalline phases, for example $Ba_2SrB_3O_{12}$ and $(Ba_{1.84}Sr_{1.16})$ $(B_3O_6)_2$, reduces the vitreous B_2O_3 content in the glass matrix. The capture of B_2O_3 in a crystalline phase is expected to lead to good stability against volatilization and thus an improvement in the thermal stability of the resulting glass ceramic is also expected [131]. Furthermore, alkaline-earth boride phases have a possible self-healing behavior in glass sealants [102].

Table 4-16. The crystallographic information of polymorphism SiO_2 phases formed in BS glasses

Sample	PDF card	Mineral name	Crystal structure	Space group	Space group number
BS6	01-081-0067	Quartz low (α-SiO_2)	Hexagonal	P3221	154
BS15	00-011-0378	Tridymite	Hexagonal	P63/mmc E	194
BS25	03-068-0466	Quartz low, syn	Hexagonal	P3221	154
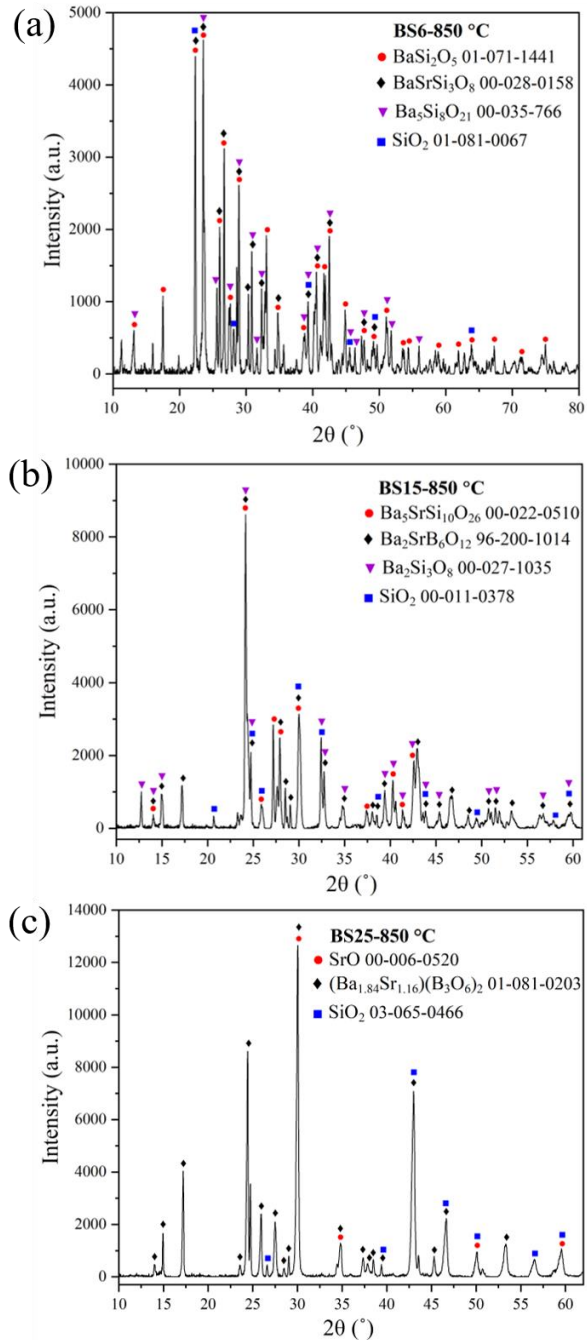
Fig. 4-59. XRD patterns of BS glasses heated at 850 °C for 50 h, (a) BS6, (b) BS15 and (c) BS25

4.6.5 Joinability investigation of BS glasses

4.6.5.1 Shrinkage behavior of BS glasses analysis by sinking dilatometer

Sinking dilatometric measurements were able to simulate the stack joining conditions and the shrinkage behavior of BS glasses was observed in between two steel plates under a constant pressure of 10 KPa. Fig. 4-60 shows the shrinkage behavior for three different BS glass solders. Onset shrinking temperature (T_a), end shrinking temperature (T_b), and the maximum shrinkage rate of BS glasses are listed in Table 4-17. BS6 glass underwent a sharp shrinkage process from T_a 717 °C to T_b 786 °C. Below 717 °C, BS6 only showed slight shrinkage of less than 3%. The shrinkage curve of BS6 then remained steady after T_b until the end of the measurement. BS15 glass has a similar shrinking process to BS6 and showed the highest shrinkage rate (about 24% at 850 °C) compared with the other BS glasses. BS25 exhibited the lowest shrinkage rate (around 15%). The shrinkage rates of BS glasses are lower than that of glass H, with 39% reported in previous investigations [109]. The shrinkage is due to sintering densification and compaction of the powder as well as the viscous behavior of the glass at high temperatures.
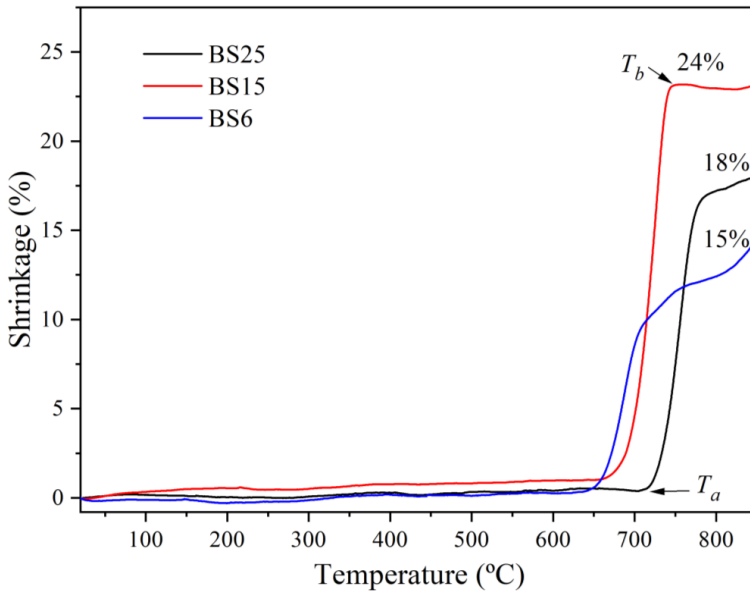
Fig. 4-60. Sinking dilatometry plots of BS glasses

Table 4-17. Onset shrinking temperature T_a, shrinking end temperature T_b and shrinkage rate at 850 °C

Sample	T_a (°C)	T_b (°C)	Shrinkage 850 °C
BS6	717	786	18%
BS15	665	748	24%
BS25	654	753	15%

4.6.5.2 Viscous flow behaviors of BS glasses

Fig. 4-61 shows hot stage microscopy (HSM) and differential scanning calorimetry (DSC) curves of the powdered BS glasses: (a) BS6, (b) BS15, and (c) BS25. The fixed viscosity temperatures[73] can be obtained from the HSM results, such as first shrinkage temperature (T_{FS}), maximum shrinkage temperature (T_{MS}), deformation temperature (T_D), half ball temperature (T_{HB}), and flow temperature (T_F). Table 4-18 summarizes the temperature values (T_{FS}, T_{MS}, T_D, T_{HB}) and the area shrinkage rates at T_{MS} for the different BS glasses obtained by TOMMIplus measurements.

Comparing HSM and DSC results in the same temperature range shows how the composition affects sintering, devitrification phenomena, and the melting behavior of glasses, and enables the suitable joining temperature for OTM application to be determined. BS glasses exhibited a similar trend with this procedure, i.e., crystallization points T_r and T_p occur between the onset shrinkage stage T_{FS} and the final sintering stage T_{MS}. In Fig. 4-62, it can be seen that where the crystallization appears, the area shrinkage rates of the curves slow down, or there is even a plateau stage. The crystallization phenomena appear before complete shrinkage/densification is obtained, which means it could prevent further sintering. With the SrO composition increasing, the T_{FS} and T_{MS} of the BS glasses decline respectively. The maximum shrinkage temperature of the BS6 glass is up to 1018 °C. BS15 and BS25 have similar T_{MS} values (878 °C, 868 °C). BS15 glass shows the highest area shrinkage rate at the maximum shrinkage point (A_{MS}/A_0), which is around 84.4%.

In contrast, no deformation or flow point of the BS6 and BS25 glasses takes place under 1100 °C. According to their DSC plots, BS6 and BS25 could melt around 1130 °C. Fig. 4-62 shows the shadow images of BS15 glass on the Crofer22APU substrate from hot stage microscopy. The deformation temperature (T_D) of BS15 occurs after the melting onset temperature (T_m), and the half ball point (T_{HB}) is at 1075 °C. From Fig. 4-62, it can be seen that the optimal joining temperature of BS15 glass should be around the maximum melting peak temperature (T_{mp}), 1071 °C, between T_D and T_{HB}. The Half ball temperature of the BS glass is higher than 1000 °C, which is advantageous for high-temperature (HT) joining applications.

Table 4-18. Hot stage microscopy data of BS glasses

Sample	T_{FS} (°C)	T_{MS} (°C)	T_D (°C)	T_{HB} (°C)	A_{MS}/A_0
BS6	675	1018	–	–	85.5%
BS15	650	878	1033	1075	84.4%
BS25	633	868	–	–	87.5%
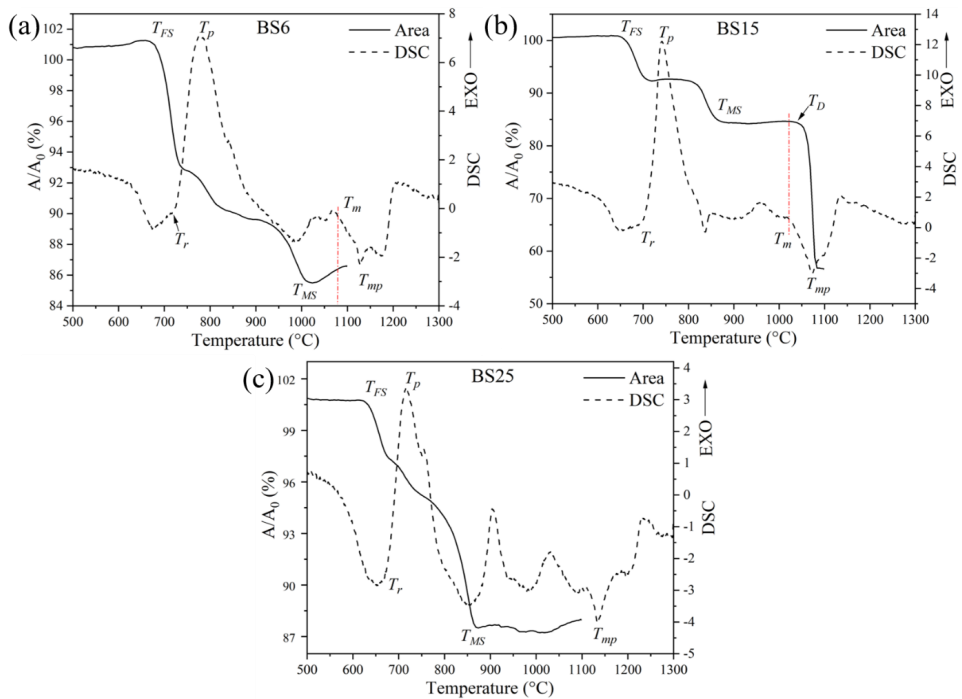
Fig. 4-61. HSM and DTA curves obtained from the powdered BS glasses (a) BS6, (b) BS15, and (c) BS25.

(a) First shrinkage
651°C

(b) Maximum shrinkage
878°C

(c) Start deformation
1033°C

(d) deformation
1070°C

(e) Half ball
1075°C

(f) Flow
1080°C
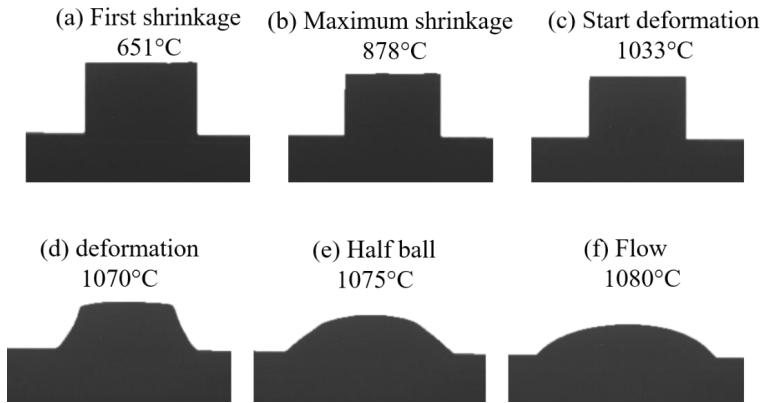
Fig. 4-62. Shadow images of BS15 glass pellet on Crofer22APU substrate from HSM

4.6.5.3 Helium leakage test for the joint

In accordance with the previous investigation, BS15 glass was chosen for Helium leak testing and assembly test joining with Aluchrom and STF25 due to their relatively high CTEs (11.9×10^{-6} K^{-1}), dense microstructure, highest shrinkage rate (24%), and good viscous behavior at high temperatures compared with other BS glasses.

As a next step, a gas leakage experiment was firstly performed to verify the joinability of the BS15 sealant with the Aluchrom substrate. In accordance with hot stage microscopy analyses for BS15 glass, the joining process was chosen at 1075 °C for 5 min. The sample sealed by glass sealant BS15 showed very good gas-tightness with a helium leakage rate lower than the detection limit of 10^{-9} mbar·l·s^{-1}. According to the indications of Mahapatra et al., the sealant with a gas leakage rate of lower than 10^{-7} mbar·l·s^{-1} would fulfill the requirements for the high temperature operation of the OTM module [143]. In order to check inner joining structure, the gas-tight joint Aluchrom/BS15/Aluchrom was cut open. The macroscopic and magnified images of the joint are presented in Fig. 4-63. The joint exhibits a very dense joining structure (Fig. 4-63 b), and no crack or defect could be found. This joint setup was separated with difficulty, and the mechanical force that was applied significantly exceeded the strength of ZrO_2, meaning that the ZrO_2 spacers were torn, as seen in Fig. 4-63 (c). In contrast, the BS15 glass sealant achieved good wettability and excellent adherence to Aluchrom. BS15 should have good mechanical properties. The specific mechanical test will be carried out in future.
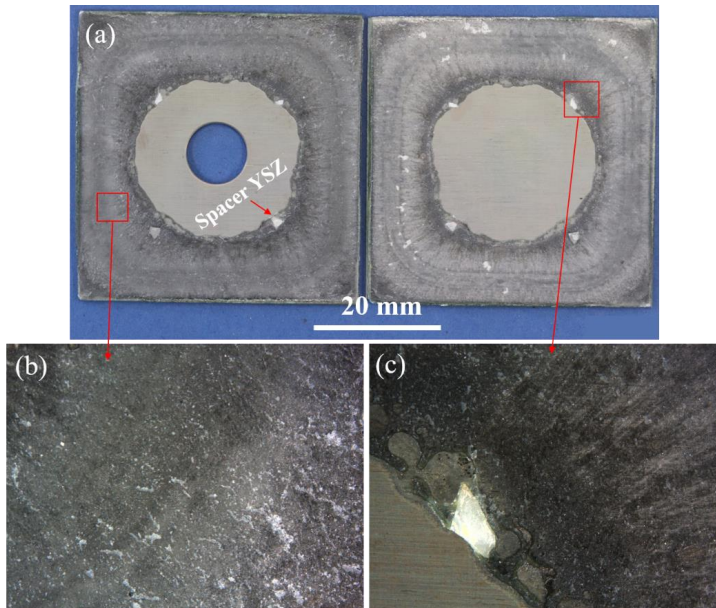
Fig. 4-63. The chopped gas-tight joint Alchrom/BS15/Aluchrom joining at 1075 °C for 5 min, (a) overview, (b) and (c) magnification

SEM images of the cross sections of the gas-tight Alchrom/BS15/Aluchrom joint are shown in Fig. 4-64. No large pores were detected from the SEM analysis. However, obvious cracks were found in the sealant. Since no cracks were found in Fig. 4-63 and the joint showed excellent gas tightness, it is concluded that the cracks were formed during metallographic processing, such as cutting and grinding. Moreover, Fig. 4-64 (a) and (b) show two different areas of the same joint. Inhomogeneous structures were observed for the two different parts of BS15, which could be explained by the phase segregation in the pure glass sealant. For the interfaces of the BS15 glass sealant and Aluchrom, BS15 glass achieved excellent adherence to Aluchrom, and there was no reaction, crack, or formation of pores found at the two interfaces. Fig. 4-65 shows SEM-EDS maps of the gas-tight Aluchrom/BS15/Aluchrom joint after joining at 1075 °C for 5 min to analyze crystalline phases from the BS15 sealant and the interdiffusion layer of BS15 and Aluchrom. Aluchrom formed a thin scale layer, which is assumed to be Cr/Al oxide scale from the mapping images. The black columnar pointed phase is assumed to be quartz with a small amount of Sr diffusion inside. Some crystal phases also formed from the BS15 glass, such as the Ba silicate phase and the Ba–Sr silicate phase. The SEM-EDS mapping results are in good agreement with the XRD result of BS 15 (Fig. 4-59 c).

Fig. 4-66 shows interfacial microstructure and EDS mapping of Aluchrom and glass sealant BS15. One can see the formation of a Al_2O_3 scale followed by a chromia sublayer which is in a good agreement with literature [145]. A schematic diagram of the interface reaction between BS15 glass

sealant and Aluchrom joined at 1075 °C for 5 min was shown in Fig. 4-67. Besides, the scale oxidized at interface of Aluchrom has been partially dissolved by BS15 glass during high temperature joining process. Internal corrosion of the steel leads to Fe/Cr nodules precipitation and the interface is composed of the two zones of island-like steel residues with Alumina-enriched glass-ceramic adjacent to the Aluchrom.
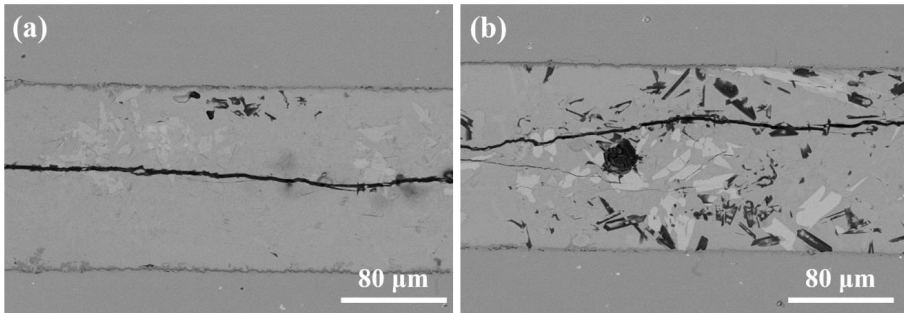
Fig. 4-64. SEM images of the gas-tight joint Alchrom/BS15/Aluchrom joining at 1075 °C for 5 min, (a) and (b) show inhomogeneous structures.
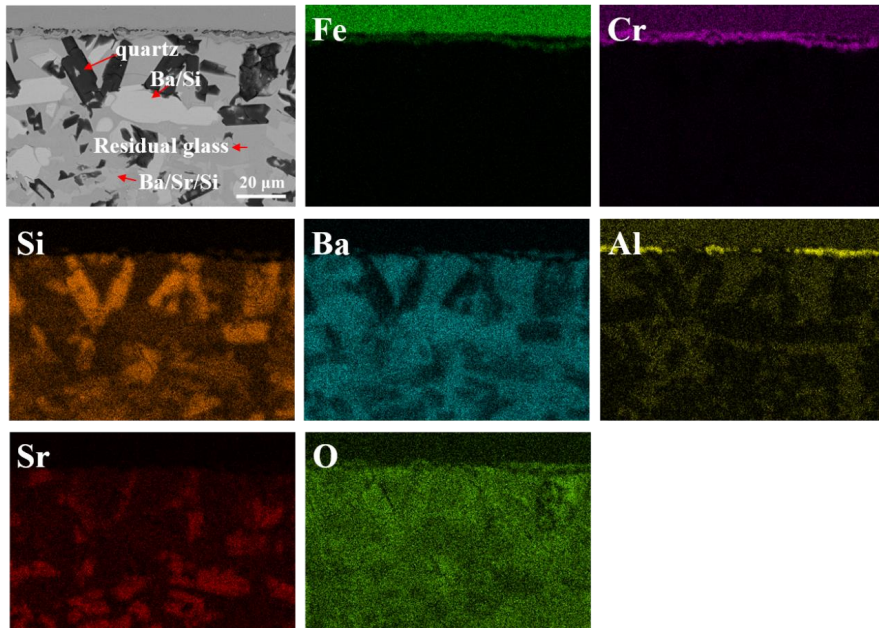
Fig. 4- 65. SEM-EDS maps of the gas-tight joint Alchrom/BS15/Aluchrom joining at 1075 °C for 5 min for analyzing crystalline phases from BS15 sealant and interaction layer of BS15 and Aluchrom.
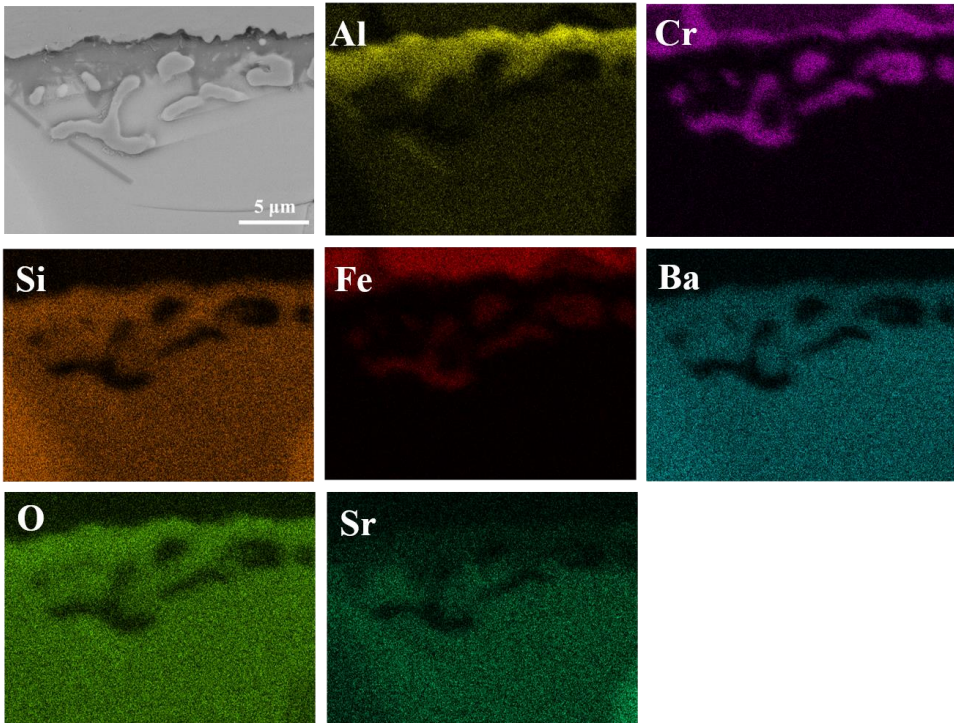
Fig. 4-66. SEM-EDS maps of the gas-tight joint Alchrom/BS15/Aluchrom joined at 1075 °C for 5 min to analyze interaction between BS15 glass and Aluchrom
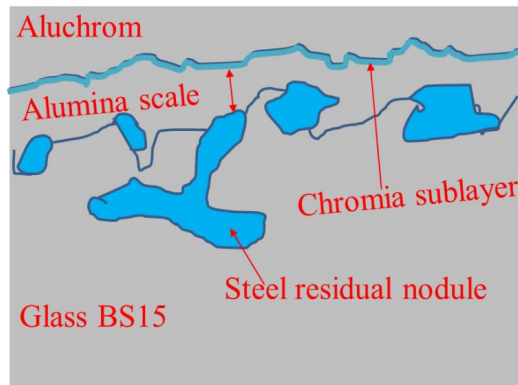
Fig. 4-67. Schematic diagram of the interface reaction between BS15 glass sealant and Aluchrom joined at 1075 °C for 5 min

4.6.5.4 Assembling test with membrane STF25

The assembly of the experiment with OTM and Aluchrom was also investigated to verify the joinability of the BS15 for further applications. Fig. 4-68 (a) shows the assembly before joining. The glass sealant green foil stamped to a suitable size was placed in the middle of the Aluchrom and the STF25. In contrast, there is a severe reaction and spallation between the BS15 glass and the STF25 membrane and Aluchrom after joining for 5 min at 1075 °C, as seen in Fig. 4-68 (b-d). The dark green part visible in Fig. 4-68 (c) can be assumed to be BS15 glass as shown in SEM image of Fig. 4-69 (a) of glass sealant layer. From literature, observation of a color change (to green) is associated with the formation of a chromia sublayer under the alumina scale [145], which coincides with Aluchrom/BS15 interfacial analysis (Fig. 4-66). There is a hypothesis that chromium ions diffuse into glass sealant layer at high temperature, so that the color of glass BS15 changes to green. From Fig. 4-69 (b) the side view of the broken BS15/STF25 part, BS15 displayed good adherence with STF25 at interface. Whereas the surface of BS15/STF25 shows a red-yellow reaction product which has a coloring similar to rusty. In the STF25 ($SrTi_{0.75}Fe_{0.25}O_{3-\delta}$) membranes, Fe^{3+} and essentially smaller amounts of Fe^{4+} predominantly exist [162]. The Fe–O band of high valences Fe^{4+} show metallic behavior [163]. Moreover, according to investigations by Silva [130], a hexagonal (Sr, Fe)-rich secondary phase $SrFe_{12}O_{19}$ was identified in STF25, with the exception of the cubic perovskite phase, which may cause the inhomogeneous phase distribution, rust color, and severe reaction with the BS15 glass at a high temperature over 1000 °C.

There are two possible ways to solve the reaction problem between BS15 and STF25. First, the joining temperature could be reduced to around 900 °C. Another possible strategy is to use the coated membrane SF25, such as yttria-stabilized zirconia (YSZ) coating. Some literatures have studied oxygen transport membrane of YSZ showed high chemical, mechanical stabilities [164-166] and good compatibility with other membranes such as $LaCrO_3$ [164], $SrCo_{0.4}Fe_{0.6}O_{3-\delta}$ [167]. Future studies are necessary to investigate the possibility of these two strategies and their interfacial reaction behavior.
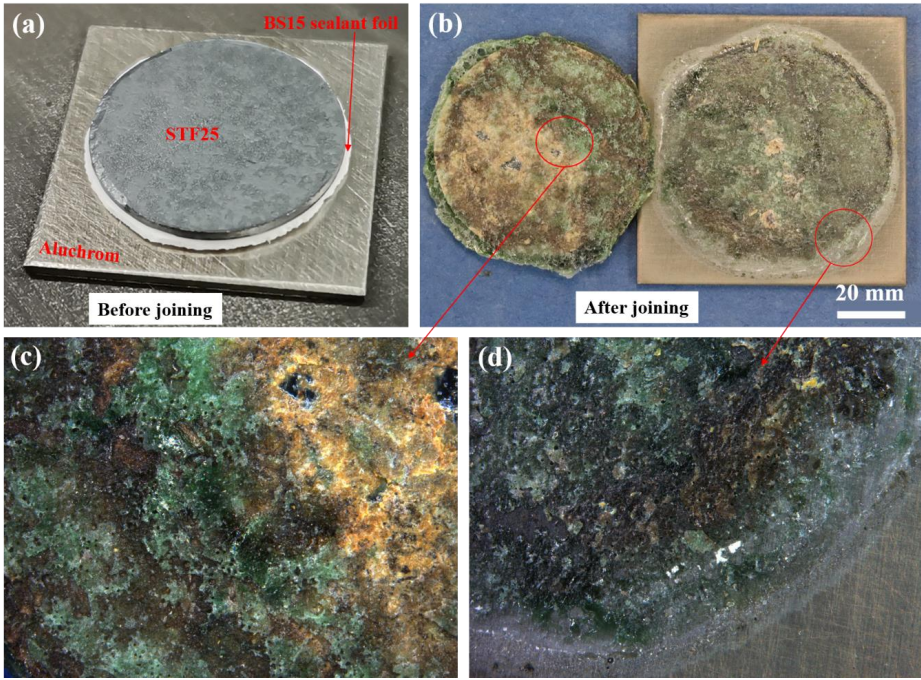
Fig. 4-68. BS15 sealant joining with Aluchrom and STF25 membrane (1075 °C, 5 min), (a) before joining, (b) after joining, (c) zoom in picture of membrane side, (d) zoom in picture of Aluchrom side
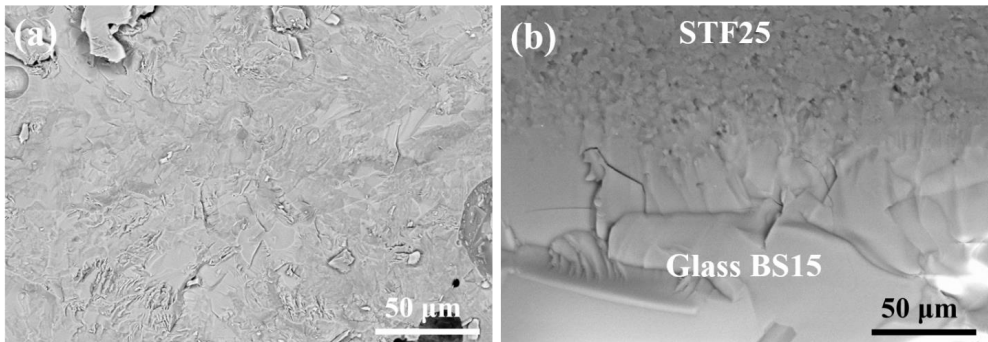
Fig. 4-69. SEM images of BS15/STF25 part from the assembled joint shown in Fig. 4-68 (c), (a) top view on glass sealant layer, (b) side view after breaking of the BS15/STF25 piece

4.6.6 Summary

Three new BaO–SrO–SiO$_2$–B$_2$O$_3$ glasses (BS6, BS15, and BS25) with different SrO contents were fabricated using the melting quenching method. The content of strontium was investigated firstly in terms of its effect on the glass-forming tendency, thermal expansion coefficient (CTE), crystallization, shrinkage behavior and viscous flow properties. The values of T_g, T_r, and T_p of BS glasses decrease with increasing strontia content. BS15 glasses has the best glass-forming tendencies and thermal stability in three BS glasses. The CTE value decreases with the increasing SrO content of the BS glasses. The composition BS6 reached the highest CTE values of up to 14.5×10^{-6} K^{-1}. The glass with 15 mol% SrO (BS15) achieved the most matching CTE of 11.9×10^{-6} K^{-1} with STF25 and Aluchrom. Ba/Sr compounds were formed in three BS glasses after heat treatment at 850 °C. Besides, BS15 glass shows the densest microstructure, highest shrinkage rate (24%), and good viscous behavior at high joining temperatures compared with other BS glasses. Thus, BS15 glass was chosen for helium leak test and assembly test joining with Aluchrom and STF25. The optimal joining temperature of the BS15 glass was chosen at close to half-ball temperature. The sandwiched sample sealed by BS15 glass at 1075 °C for 5 min achieved excellent gas-tightness with low helium leakage rate $< 10^{-9}$ mbar·l·s^{-1} and dense microstructure when joining with Aluchrom. Unfavorable strong interaction and spallation was observed in the assembly test joining of BS15 glass with STF25. Lowering the joining temperature and testing of other oxygen transport membranes will be investigated in the future to solve this problem.

5. Conclusions

The aim of this work is focused on developing new glass-based sealants with suitable thermal expansion properties. Two strategies were used to achieve this aim. One is to add different filler materials to glass matrix H to form composites. Another is the development of a new glass by adjusting the glass composition. To gain a better understanding of the technological aspects, the crystallization behavior of the investigated glass matrix, the joining behaviors of different composite materials and variations of the thermal treatment to fast joining processes were also investigated and evaluated in this thesis.

BaO–CaO–SiO$_2$–B$_2$O$_3$ glass H exhibits a good glass glass-forming tendency and great stability. The CTE of the sintered glass H is in the range of 8.5–10.8 $\times$ 10^{-6} K^{-1}. The CTE of annealed samples decreased compared to as-sintered glass H. XRD results and FactSage simulation indicate the formation of low CTE phases Hexacelsian BaAl$_2$Si$_2$O$_8$ and calcium aluminosilicate Ca$_2$Al$_2$SiO$_7$ in glass composition H to be the main reason causing the CTE to decline. Boron is dissolved in the slag and bonded in crystalline phases. The volatilization of boron in glass H is negligible below 1300 °C. FactSage calculation is in good agreement with XRD analysis. The FactSage simulations provides a visual guidance for the development of glass sealants.

Metallic fillers (Ni, Ni-Cr, Ag, Fe30Cr5Al0.5Y) and membrane-type fillers (STF25, STF35 and CGO) were added to glass H in different proportions. The CTE improved with increasing filler content. The composites with 40 wt.% Ag and with 30 wt.% Ni resulted in the highest CTE values compared to other filler-reinforced samples up to 12.9 $\times$ 10^{-6} K^{-1}. The samples sealed with HAg40 and HNC30 glass composites showed good gas-tightness and sealing behaviors with STF25 and support metals (Aluchrom and pre-oxidized Aluchrom). The membrane side with a glass composite sealant formed a transitional thin layer by chemical bonding. On the support metal side, pre-oxidized Aluchrom formed a thicker oxidation Al$_2$O$_3$ layer compared to Aluchrom, which enhanced the sealing strength at the joints by forming chemical bonds with the glass matrix. The HAg40 sealed joint obtained the higher shear strength of 62.2 MPa. Both HAg40 and HNC30 samples exhibited excellent gas-tightness with leakage rate smaller than 10^{-9} mbar·l·s^{-1} after 20 thermal cycles between room temperature and 800 °C. The HAg40 joint demonstrated good chemical stability with a good gas tightness after 1500 h heat treatment at 800 °C. Thus, HAg40 is thus the most promising candidate as a sealant for OTM.

The feasibility of the fast joining process was investigated for two glass-based sealants HAg40 and HNC30. Viscous flow behavior and the optimum joining temperature zone were monitored by HSM. The optimal joining temperature of the HAg40 glass-composite sealant was measured to be in the range of 880 – 935 °C. The optimal joining temperature of the HNC30 glass-ceramic sealant was recorded at 880 – 920 °C. All fast-joined samples have shown low helium leakage values below the detection limit of 10^{-9} mbar·l·s^{-1}. Microstructural analysis revealed that the HNC30 sealant exhibited homogeneous structures and good joining behavior with STF25 and Aluchrom in all three joining processes. Some small crystals preferentially precipitated from the two interfaces.

The glass matrix H in the fast-joined samples remained amorphous and shows small amount beginning crystalline phases, and the oxidation condition of the Ni-Cr filler is only slight compared to the HNC30 sample joined at 850 °C for 10 h. The large Ag particles aggregated to the middle during the fast joining processes. The HNC30 composite is the most promising sealant for fast joining processes used in OTM applications.

$BaSiO_3$ was added as a filler material to the glass matrix H in varying amounts (10-30 wt.%). The CTE improved with increasing filler content. The composite with the addition of 30 wt.% $BaSiO_3$ resulted in the highest CTE values up to 11.9×10^{-6} K^{-1}. The joining behaviors were investigated by comparing three joining temperatures: 850 °C, 920 °C and 960 °C. The setups joined at 850 °C for 10 h failed for all support metals. All samples joined at increased temperatures of 960 °C or 920 °C exhibited helium leakage rates lower than 10^{-9} mbar·l·s^{-1}. The joining process at 920 °C presented smooth and less pores in the joining layer analyzed by CT. Good adhesion was achieved for HBS30 with STF25 and Aluchrom joined at 920 °C for 15 min.

10-40 wt.% Sr_2SiO_4 was then to the glass matrix H. The addition of 20 wt.% Sr_2SiO_4 (HS2S20) achieved the highest CTE value of up to 11.7×10^{-6} K^{-1} for the as-sintered sample. The HS2S20 composite with 20 wt.% Sr_2SiO_4 filler achieved a homogeneous, dense structure. The joining temperature of the HS2S20 glass-ceramic sealant was determined at around 920–960 °C. The joining behaviors were investigated by comparing three joining temperatures (850 °C, 920 °C, 960 °C). Excellent hermeticity with low helium leakage rates below 10^{-9} mbar·l·s^{-1} was achieved for three symmetrical samples joined at different temperatures and adequate deadload. Joining temperature and pressure are key factors in the success of sealing. Very promising joining behavior was observed in the joint STF25/HS2S20/Aluchrom joining at 920 °C.

Three new $BaO–SrO–SiO_2–B_2O_3$ glasses (BS6, BS15, and BS25) with different SrO contents were fabricated and investigated. Thermal properties such as the T_g, T_r, and T_p values of the BS glasses decreased with increasing strontia content. The composition BS15 exhibits the best glass-forming tendencies and thermal stability of all three investigated glasses. The CTE value decreased with the increasing SrO content of the BS glasses. BS6 reached the highest CTE values of up to 14.5×10^{-6} K^{-1}. Glass BS15 achieved the most matching CTE of 11.9×10^{-6} K^{-1} with STF25 and Aluchrom. Several Ba/Sr compounds were formed in the three BS glasses after heat treatment at 850 °C. In addition, BS15 glass presented the densest microstructure, the highest shrinkage rate 24% and good viscous behavior at high joining temperatures compared to the other BS glasses. BS15 glass was thus chosen for the helium leak test and assembly test joining with Aluchrom and STF25. The optimal joining temperature of the BS15 glass was chosen at close to half-ball temperature. The sandwiched sample sealed by BS15 glass at 1075 °C for 5 min achieved excellent gas-tightness with a low helium leakage rate ($< 10^{-9}$ mbar·l·s^{-1}) and a dense microstructure when joining with Aluchrom.

6. Outlook

The properties of glass-based sealants can be tailored for sealing OTMs by microstructural and compositional design and the addition of filler materials. Performing the joining procedure at the suitable viscous temperature can save considerable joining time and energy. In summary, glass-based sealants are promising joining materials for OTM applications. Still, further investigations need to be addressed about interfacial diffusion mechanism, mechanical properties and long-term stability in order to realize the application of the glass-based sealants in future OTMs industrialization. Therefore, it is suggested that the following points should be considered in upcoming studies of glass-based sealants:

(1) Reduce severe reactions between STF25 and BS15 glass

There are two possible ways to solve the problem of BS15 reacting with STF25. Firstly, the joining temperature could be reduced to around 900 °C. Another possible strategy is to use a coated STF25 membrane, such as an yttria-stabilized zirconia (YSZ) coating on the sealing area of STF25.

(2) Interfacial diffusion mechanism investigation

High-resolution, advanced characterization techniques such as wavelength-dispersive X-ray spectroscopy (WDS) mapping or atom probe tomography (APT) analysis will play an important role in gaining a detailed understanding of the interfacial diffusion mechanism between joined glass and OTM component.

(3) Mechanical properties of joined components

Mechanical measurements for the joints sealed by BS15, HBS30, and HS2S20 glass-based sealants need to be carried out. In addition, it is worth investigating the creep behavior and shear strength of glass-based sealants at high temperatures such as OTM operation temperature (800 °C).

(4) Long-term stability investigation

For OTM applications, glass-based sealants need to withstand long term temperature operation. Therefore, it is necessary to investigate longer term thermal stability for more than 1500 h, for instance 5000 h, 10,000 h, or even longer in future experiments.

7. References

[1] The Earth Science Communications Team at NASA's Jet Propulsion Laboratory. The Causes of Climate Change. Avalable online: https://climate.nasa.gov/causes/, 2022.

[2] European Commission. 'Fit for 55' - delivering the EU's 2030 climate target on the way to climate neutrality, Avaluable online: https://ec.europa.eu/info/strategy/priorities-2019-2024/european-green-deal/delivering-european-green-deal_en, in: E. Commission (Ed.), European Commission, Brussel, 2021, pp. https://ec.europa.eu/info/strategy/priorities-2019-2024/european-green-deal/delivering-european-green-deal_en.

[3] K. Zhang, J. Sunarso, Z.P. Shao, W. Zhou, C.H. Sun, S.B. Wang, S.M. Liu, Research progress and materials selection guidelines on mixed conducting perovskite-type ceramic membranes for oxygen production, RSC Adv., 1 (2011) 1661-1676.

[4] M. Gambini, M. Vellini, Oxygen Transport Membranes for Ultra-Supercritical (USC) Power Plants With Very Low CO_2 Emissions, Journal of Engineering for Gas Turbines and Power, 134 (2012).

[5] A.C. Bose, Inorganic Membranes for Energy and Environmental Applications, Springer New York 2009.

[6] W. Deibert, M.E. Ivanova, S. Baumann, O. Guillon, W.A. Meulenberg, Ion-conducting ceramic membrane reactors for high-temperature applications, Journal of Membrane Science, 543 (2017) 79-97.

[7] R. Oliveira Silva, Microstructure and Thermomechanical Properties of $SrTi_{1-x}Fe_xO_{3-\delta}$ Oxygen Transport Membranes and Supports, 2018.

[8] W.A. Meulenberg, F. Schulze-Kuppers, W. Deibert, T. Van Gestel, S. Baumann, Ceramic Membranes: Materials - Components - Potential Applications, Chem. Ing. Tech., 91 (2019) 1091-1100.

[9] K. Zhang, G.R. Zhang, Z.K. Liu, J.W. Zhu, N. Zhu, W.Q. Jin, Enhanced stability of membrane reactor for thermal decomposition of CO_2 via porous-dense-porous triple-layer composite membrane, Journal of Membrane Science, 471 (2014) 9-15.

[10] Y.L. Luo, T. Liu, J.F. Gao, C.S. Chen, $Zr_{0.84}Y_{0.16}O_{1.92}$ -$La_{0.8}Sr_{0.2}Cr_{0.5}Fe_{0.5}O_{3-\delta}$ composite membrane for CO_2 decomposition, Mater. Lett., 86 (2012) 5-8.

[11] F. Schulze-Kuppersa, F. Drago, L. Ferravante, S. Herzog, S. Baumann, P. Pinacci, W.A. Meulenberg, Design and fabrication of large-sized planar oxygen transport membrane components for direct integration in oxy-combustion processes, Sep. Purif. Technol., 220 (2019) 89-101.

[12] F. Schulze-Kuppers, S.F.P. ten Donkelaar, S. Baumann, P. Prigorodov, Y.J. Sohn, H.J.M. Bouwmeester, W.A. Meulenberg, O. Guillon, Structural and functional properties of $SrTi_{1-x}Fe_xO_{3-\delta}$ ($0 \le x \le 1$) for the use as oxygen transport membrane, Sep. Purif. Technol., 147 (2015) 414-421.

[13] X. Li, S.M. Groß-Barsnick, T. Koppitz, S. Baumann, W.A. Meulenberg, G. Natour, Sealing behaviour of glass-based composites for oxygen transport membranes, J. Eur. Ceram. Soc., 42 (2022) 2879-2891.

[14] K. Scott Weil, C.A. Coyle, J.T. Darsell, G.G. Xia, J.S. Hardy, Effects of thermal cycling and thermal aging on the hermeticity and strength of silver–copper oxide air-brazed seals, J. Power Sources, 152 (2005) 97-104.

[15] K. Asaoka, N. Kuwayama, Temperature dependence of thermal expansion coefficient for palladium-based binary alloy, Dent Mater J, 9 (1990) 47-57.

[16] M. Salvo, V. Casalegno, S. Rizzo, F. Smeacetto, A. Ventrella, M. Ferraris, Glasses and glass-ceramics as brazing materials for high-temperature applications, in: D.P. Sekulic (Ed.) Advances in Brazing: Science, Technology and Applications, Woodhead Publ Ltd, Cambridge, 2013, pp. 525-544.

[17] N.S. Saetova, E.S. Shirokova, D.A. Krainova, N.S. Chebykin, B.A. Ananchenko, I.V. Tolstobrov, K.S. Belozerov, A.V. Kuzmin, The development of 3D technology for the creation of glass sealants for tubular oxide fuel cells, Int. J. Appl. Glass Sci., (2022).

[18] J.W. Fergus, Sealants for solid oxide fuel cells, J. Power Sources, 147 (2005) 46-57.

[19] M.K. Mahapatra, K. Lu, Glass-based seals for solid oxide fuel and electrolyzer cells - A review, Mater. Sci. Eng. R-Rep., 67 (2010) 65-85.

[20] S.M. Gross, D. Federmann, J. Remmel, M. Pap, Reinforced composite sealants for solid oxide fuel cell applications, J. Power Sources, 196 (2011) 7338-7342.

[21] M.J. den Exter, W.G. Haije, J.F. Vente, Viability of ITM Technology for Oxygen Production and Oxidation Processes: Material, System, and Process Aspects, in: A.C. Bose (Ed.) Inorganic Membranes for Energy and Environmental Applications, Springer New York, New York, NY, 2009, pp. 27-51.

[22] R.O. Silva, J. Malzbender, F. Schulze-Kuppers, S. Baumann, M. Kruger, O. Guillon, Creep behaviour of dense and porous $SrTi_{0.75}Fe_{0.25}O_{3-\delta}$ for oxygen transport membranes and substrates, J. Eur. Ceram. Soc., 38 (2018) 5067-5073.

[23] R. Kiebach, S. Pirou, L.M. Aguilera, A.B. Haugen, A. Kaiser, P.V. Hendriksen, M. Balaguer, J. Garcia-Fayos, J.M. Serra, F. Schulze-Kuppers, M. Christie, L. Fischer, W.A. Meulenberg, S. Baumann, A review on dual-phase oxygen transport membranes: from fundamentals to commercial deployment, J. Mater. Chem. A, 10 (2022) 2152-2195.

[24] J. Sunarso, S. Baumann, J.M. Serra, W.A. Meulenberg, S. Liu, Y.S. Lin, J.C.D. da Costa, Mixed ionic-electronic conducting (MIEC) ceramic-based membranes for oxygen separation, Journal of Membrane Science, 320 (2008) 13-41.

[25] P.N. Dyer, R.E. Richards, S.L. Russek, D.M. Taylor, Ion transport membrane technology for oxygen separation and syngas production, Solid State Ion., 134 (2000) 21-33.

[26] X. Zhu, W. Yang, Introduction to Mixed Ionic–Electronic Conducting Membranes, in: X. Zhu, W. Yang (Eds.) Mixed Conducting Ceramic Membranes: Fundamentals, Materials and Applications, Springer Berlin Heidelberg, Berlin, Heidelberg, 2017, pp. 1-10.

[27] F. Zeng, Mechanical reliability and oxygen permeation of $Ce_{0.8}Gd_{0.2}O_{2-\delta}$-$FeCo_2O_4$ dual phase membranes, 2021.

[28] F.A. Kröger, H.J. Vink, Relations between the Concentrations of Imperfections in Crystalline Solids, in: F. Seitz, D. Turnbull (Eds.) Solid State Physics, Academic Press1956, pp. 307-435.

[29] L.L. Cai, X.Y. Wu, X.F. Zhu, A.F. Ghoniem, W.S. Yang, High-performance oxygen transport membrane reactors integrated with IGCC for carbon capture, Aiche Journal, 66 (2020).

[30] S. Smart, J.C.D. da Costa, S. Baumann, W.A. Meulenberg, Oxygen transport membranes: dense ceramic membranes for power plant applications, in: A. Basile, S.P. Nunes (Eds.) Advanced Membrane Science and Technology for Sustainable Energy and Environmental Applications2011, pp. 255-292.

[31] A.S. Bhalla, R. Guo, R. Roy, The perovskite structure—a review of its role in ceramic science and technology, Materials Research Innovations, 4 (2000) 3-26.

[32] S. Gupta, M.K. Mahapatra, P. Singh, Lanthanum chromite based perovskites for oxygen transport membrane, Materials Science and Engineering: R: Reports, 90 (2015) 1-36.

[33] J. Sunarso, S.S. Hashim, N. Zhu, W. Zhou, Perovskite oxides applications in high temperature oxygen separation, solid oxide fuel cell and membrane reactor: A review, Progress in Energy and Combustion Science, 61 (2017) 57-77.

[34] Z. Shao, W. Yang, Y. Cong, H. Dong, J. Tong, G. Xiong, Investigation of the permeation behavior and stability of a $Ba_{0.5}Sr_{0.5}Co_{0.8}Fe_{0.2}O_{3-\delta}$ oxygen membrane, Journal of Membrane Science, 172 (2000) 177-188.

[35] S. Baumann, J.M. Serra, M.P. Lobera, S. Escolástico, F. Schulze-Küppers, W.A. Meulenberg, Ultrahigh oxygen permeation flux through supported $Ba_{0.5}Sr_{0.5}Co_{0.8}Fe_{0.2}O_{3-\delta}$ membranes, Journal of Membrane Science, 377 (2011) 198-205.

[36] Y. Zou, W. Zhou, S. Liu, Z. Shao, Sintering and oxygen permeation studies of $La_{0.6}Sr_{0.4}Co_{0.2}Fe_{0.8}O_{3-\delta}$ ceramic membranes with improved purity, J. Eur. Ceram. Soc., 31 (2011) 2931-2938.

[37] J.M. Serra, J. Garcia-Fayos, S. Baumann, F. Schulze-Küppers, W.A. Meulenberg, Oxygen permeation through tape-cast asymmetric all-$La_{0.6}Sr_{0.4}Co_{0.2}Fe_{0.8}O_{3-\delta}$ membranes, Journal of Membrane Science, 447 (2013) 297-305.

[38] J. Ovenstone, J.-I. Jung, J.S. White, D.D. Edwards, S.T. Misture, Phase stability of BSCF in low oxygen partial pressures, J. Solid State Chem., 181 (2008) 576-586.

[39] Y. Liu, V. Motalov, S. Baumann, D. Sergeev, M. Müller, Y.J. Sohn, O. Guillon, Thermochemical stability of Fe- and co-functionalized perovskite-type $SrTiO_3$ oxygen transport membrane materials in syngas conditions, J. Eur. Ceram. Soc., 39 (2019) 4874-4881.

[40] A.A. Murashkina, E.Y. Pikalova, A.K. Demin, Promising membrane materials based on strontium titanate, Russian Journal of Electrochemistry, 45 (2009) 542-547.

[41] R.O. Silva, J. Malzbender, F. Schulze-Kuppers, S. Baumann, M. Kruger, O. Guillon, Microstructure and anisotropic mechanical properties of freeze dried $SrTi_{0.75}Fe_{0.25}O_{3-\delta}$ for oxygen transport membrane substrates, J. Eur. Ceram. Soc., 38 (2018) 2774-2783.

[42] L.L. Anderson, P.A. Armstrong, R.R. Broekhuis, M.F. Carolan, J. Chen, M.D. Hutcheon, C.A. Lewinsohn, C.F. Miller, J.M. Repasky, D.M. Taylor, C.M. Woods, Advances in ion transport membrane technology for oxygen and syngas production, Solid State Ion., 288 (2016) 331-337.

[43] J. Garcia-Fayos, M.P. Lobera, M. Balaguer, J.M. Serra, Catalyst Screening for Oxidative Coupling of Methane Integrated in Membrane Reactors, Frontiers in Materials, 5 (2018).

[44] D.G. Lee, J.W. Nam, S.H. Kim, S.W. Cho, Structure Optimization of a High-Temperature Oxygen-Membrane Module Using Finite Element Analysis, Energies, 14 (2021).

[45] N. Nauels, S. Herzog, M. Modigell, C. Broeckmann, Membrane module for pilot scale oxygen production, Journal of Membrane Science, 574 (2019) 252-261.

[46] F. Drago, P. Fedeli, A. Cavaliere, A. Cammi, S. Passoni, R. Mereu, S. de la Pierre, F. Smeacetto, M. Ferraris, Development of a Membrane Module Prototype for Oxygen Separation in Industrial Applications, Membranes, 12 (2022).

[47] R. Loehman, T. Garino, R. Tandon, E. Corral, M. Brochu, B. Gauntt, S. Widgeon, Filled Glass Composites for Sealing of Solid Oxide Fuel Cells, Sandia Report, (2009).

[48] V. Middelkoop, Reactive Air Brazing (RAB) for Gas Separation Membranes, in: E. Drioli, L. Giorno (Eds.) Encyclopedia of Membranes, Springer Berlin Heidelberg, Berlin, Heidelberg, 2016, pp. 1710-1713.

[49] S. Escolastico, F. Schulze-Kuppers, S. Baumann, K. Haas-Santo, R. Dittmeyer, Development and Proof of Concept of a Compact Metallic Reactor for MIEC Ceramic Membranes, Membranes, 11 (2021).

[50] M. Singh, T.P. Shpargel, R. Asthana, Brazing of stainless steel to yttria-stabilized zirconia using gold-based brazes for solid oxide fuel cell applications, Int. J. Appl. Ceram. Technol., 4 (2007) 119-133.

[51] K.L. Lin, M. Singh, R. Asthana, Characterization of yttria-stabilized-zirconiaistainless steel joint interfaces with gold-based interlayers for solid oxide fuel cell applications, J. Eur. Ceram. Soc., 34 (2014) 355-372.

[52] K.S. Weil, J.S. Hardy, J.Y. Kim, Oxidation ceramic to metal braze seals for applications in high temperature electrochemical devices and method of making, Google Patents, 2006.

[53] Z.Q. Wang, C. Li, X.Q. Si, C.H. Wu, J.L. Qi, J.C. Feng, J. Cao, Interfacial microstructure and mechanical properties of SiC joints achieved by reactive air brazing using Ag-V2O5 filler, J. Eur. Ceram. Soc., 39 (2019) 2617-2625.

[54] H. Chen, L.J. Li, R. Kemps, B. Michielsen, M. Jacobs, F. Snijkers, V. Middelkoop, Reactive air brazing for sealing mixed ionic electronic conducting hollow fibre membranes, Acta Mater., 88 (2015) 74-82.

[55] A. Kaletsch, E.M. Pfaff, C. Broeckmann, Effect of Aging on Microstructure and Mechanical Strength of Reactive Air Brazed BSCF/AISI 314-Joints, Adv. Eng. Mater., 16 (2014) 1430-1436.

[56] M. Schulz, U. Pippardt, L. Kiesel, K. Ritter, R. Kriegel, Oxygen permeation of various archetypes of oxygen membranes based on BSCF, Aiche Journal, 58 (2012) 3195-3202.

[57] M.D. Kim, F.R.W. Muhamad, K. Raju, S. Kim, J.H. Yu, C.D. Park, D.H. Yoon, Efficacy of Ag-CuO Filler Tape for the Reactive Air Brazing of Ceramic-Metal Joints, Journal of the Korean Ceramic Society, 55 (2018) 492-497.

[58] J.S. Hardy, K.S. Weil, Development of High-Temperature Air Braze Filler Metals for Use in Two-Step Joining and Sealing Processes, Welding Journal, 87 (2008) 195S-201S.

[59] Y.W. Zhang, L.L. Zhang, W. Guo, T. Liu, C.Z. Wu, W.Z. Ding, X.G. Lu, Interfacial reaction and microstructural evolution of Ag-Cu braze on BaCo0.7Fe0.2Nb0.1O3-delta at high temperature in air, Ceram. Int., 43 (2017) 810-819.

[60] L.L. Zhang, K. Li, C.C. Yu, Y.W. Zhang, C.Z. Wu, W.Z. Ding, Wetting Properties and Interface Reaction Mechanism of Ag-Cu Brazes on Dual-phase Membrane Ceramic, Journal of Inorganic Materials, 31 (2016) 607-612.

[61] F.R.W. Muhamad, D.H. Yoon, K. Raju, S. Kim, K.S. Song, J.H. Yu, Interfacial microstructure and shear strength of reactive air brazed oxygen transport membrane ceramic-metal alloy joints, Met. Mater.-Int., 24 (2018) 157-169.

[62] R. Kiebach, K. Engelbrecht, K. Kwok, S. Molin, M. Sogaard, P. Niehoff, F. Schulze-Kuppers, R. Kriegel, J. Kluge, P.V. Hendriksen, Joining of ceramic $Ba_{0.5}Sr_{0.5}Co_{0.8}Fe_{0.2}O_3$ membranes for oxygen production to high temperature alloys, Journal of Membrane Science, 506 (2016) 11-21.

[63] K. Bobzin, T. Schlafer, N. Kopp, Thermochemistry of brazing ceramics and metals in air, International Journal of Materials Research, 102 (2011) 972-976.

[64] S.R. Le, Z.M. Shen, X.D. Zhu, X.L. Zhou, Y. Yan, K.N. Sun, N.Q. Zhang, Y.X. Yuan, Y.C. Mao, Effective Ag-CuO sealant for planar solid oxide fuel cells, Journal of Alloys and Compounds, 496 (2010) 96-99.

[65] E. Axinte, Glasses as engineering materials: A review, Mater. Des., 32 (2011) 1717-1732.

[66] B. Cela, S. Sillapawatana, S.M. Gross, T. Koppitz, R. Conradt, Influence of filler additives on the effective viscosity of glass-ceramic composite sealants, Journal of the University of Chemical Technology and Metallurgy, 47 (2012) 449-458.

[67] C.J. Hudecek, Sealing glasses, Engineered Materials Handbook,, ASMInternational, USA, 1991, pp. 493-501.

[68] P. Geasee, Development of crystallizing glass sealants for high temperature planar solid oxide fuel cells, RWTH Aachen2003.

[69] D.G.R. William D. Callister Jr., Materials Science and Engineering: An Introduction, Wiley & Sons2010.

[70] Q. Zheng, J.C. Mauro, Viscosity of glass-forming systems, J. Am. Ceram. Soc., 100 (2017) 6-25.

[71] K. Eichler, G. Solow, P. Otschik, W. Schaffrath, BAS (BaO center dot Al2O3 center dot SiO2)-glasses for high temperature applications, J. Eur. Ceram. Soc., 19 (1999) 1101-1104.

[72] A.A. Reddy, D.U. Tulyaganov, M.J. Pascual, V.V. Kharton, E.V. Tsipis, V.A. Kolotygin, J.M.F. Ferreira, Diopside-Ba disilicate glass-ceramic sealants for SOFCs: Enhanced adhesion and thermal stability by Sr for Ca substitution, Int. J. Hydrog. Energy, 38 (2013) 3073-3086.

[73] M.J. Pascual, L. Pascual, A. Duran, Determination of the viscosity-temperature curve for glasses on the basis of fixed viscosity points determined by hot stage microscopy, Phys. Chem. Glasses, 42 (2001) 61-66.

[74] M. Bano, I. Strharsky, I. Hrmo, A viscosity and density meter with a magnetically suspended rotor, Review of Scientific Instruments, 74 (2003) 4788-4793.

[75] N. Sharmin, M.S. Hasan, C.D. Rudd, D. Boyd, U. Werner-Zwanziger, I. Ahmed, A.J. Parsons, Effect of boron oxide addition on the viscosity-temperature behaviour and structure of phosphate-based glasses, Journal of Biomedical Materials Research Part B-Applied Biomaterials, 105 (2017) 764-777.

[76] N. Bose, G. Klingenberg, G. Meerlender, Viscosity measurements of glass melts - Certification of reference material, Glass Science and Technology-Glastechnische Berichte, 74 (2001) 115-126.

[77] K. Singh, T. Walia, Review on silicate and borosilicate-based glass sealants and their interaction with components of solid oxide fuel cell, Int. J. Energy Res., (2021) 1–24.

[78] S.-M. Gross, T. Koppitz, J. Remmel, U. Reisgen, Glass-Ceramic Materials of the System BaO-CaO-SiO$_2$ as Sealants for SOFC Applications, Advances in Solid Oxide Fuel Cells: Ceramic Engineering and Science Proceedings 2005, pp. 239-245.

[79] M. Kerstan, C. Russel, Barium silicates as high thermal expansion seals for solid oxide fuel cells studied by high-temperature X-ray diffraction (HT-XRD), J. Power Sources, 196 (2011) 7578-7584.

[80] C. Thieme, C. Russel, Thermal expansion behavior of SrSiO$_3$ and Sr$_2$SiO$_4$ determined by high-temperature X-ray diffraction and dilatometry, J. Mater. Sci., 50 (2015) 5533-5539.

[81] M. Kerstan, M. Wuller, C. Russel, Binary, ternary and quaternary silicates of CaO, BaO and ZnO in high thermal expansion seals for solid oxide fuel cells studied by high-temperature X-ray diffraction (HT-XRD), Materials Research Bulletin, 46 (2011) 2456-2463.

[82] B. Cela Greven, Glass-ceramic sealant reinforcement for high-temperature applications, Forschungszentrum, Zentralbibliothek, Jülich, 2015.

[83] A.I. Borhan, M. Gromada, G.G. Nedelcu, L. Leontie, Influence of (CoO, CaO, B$_2$O$_3$) additives on thermal and dielectric properties of BaO-Al$_2$O$_3$-SiO$_2$ glass-ceramic sealant for OTM applications, Ceram. Int., 42 (2016) 10459-10468.

[84] M. Ahmadrezaei, M.A. S.A, A. Muchtar, C. Tan, M. Somalu, Thermal expansion behavior of the Ba$_{0.2}$Sr$_{0.8}$Co$_{0.8}$Fe$_{0.2}$O$_{3-\delta}$ (BSCF) with Sm$_{0.2}$Ce$_{0.8}$O$_{1.9}$, Ceramics - Silikaty, 58 (2014).

[85] K.D. Meinhardt, D.S. Kim, Y.S. Chou, K.S. Weil, Synthesis and properties of a barium aluminosilicate solid oxide fuel cell glass-ceramic sealant, J. Power Sources, 182 (2008) 188-196.

[86] T. Zhang, W.G. Fahrenholtz, S.T. Reis, R.K. Brow, Borate volatility from SOFC sealing glasses, J. Am. Ceram. Soc., 91 (2008) 2564-2569.

[87] D.A. Krainova, N.S. Saetova, A.S. Farlenkov, A.V. Khodimchuk, I.G. Polyakova, A.V. Kuzmin, Long-term stability of SOFC glass sealant under oxidising and reducing atmospheres, Ceram. Int., 47 (2021) 8973-8979.

[88] A. Vivet, P.M. Geffroy, V. Coudert, J. Fouletier, N. Richet, T. Chartier, Influence of glass and gold sealants materials on oxygen permeation performances in La$_{0.8}$Sr$_{0.2}$Fe$_{0.7}$Ga$_{0.3}$O$_{3-\delta}$ perovskite membranes, Journal of Membrane Science, 366 (2011) 132-138.

[89] J. Hatcher, M.J. Pascual, D. Poulidi, I.S. Metcalfe, Development and testing of an intermediate temperature glass sealant for use in mixed ionic and electronic conducting membrane reactors, Solid State Ion., 181 (2010) 767-774.

[90] T. Horita, N. Sakai, T. Kawada, H. Yokokawa, M. Dokiya, REACTION OF SOFC COMPONENTS WITH SEALING MATERIALS, Denki Kagaku, 61 (1993) 760-762.

[91] M. Kerstan, C. Thieme, A. Kobeisy, C. Russel, Crystallizing glass seals in the system $BaO/ZnO/SiO_2$ with high coefficients of thermal expansion, J. Mater. Sci., 52 (2017) 1789-1796.

[92] A. de Pablos-Martin, S. Rodriguez-Lopez, M.J. Pascual, Processing technologies for sealing glasses and glass-ceramics, Int. J. Appl. Glass Sci., 11 (2020) 552-568.

[93] B.C. Greven, S. Gross-Barsnick, T. Koppitz, R. Conradt, F. Smeacetto, A. Ventrella, M. Ferraris, Torsional shear strength of novel glass-ceramic composite sealants for solid oxide fuel cell stacks, Int. J. Appl. Ceram. Technol., 15 (2018) 286-295.

[94] J. Brendt, S.M. Gross-Barsnick, C. Babelot, G. Natour, The influence of ZnO and V_2O_5 on the crystallization behavior of $BaO-CaO-SiO_2$ glass-ceramic sealants, J. Non-Cryst. Solids, 501 (2018) 78-84.

[95] Y.S. Chou, J.W. Stevenson, P. Singh, Effect of aluminizing of Cr-containing ferritic alloys on the seal strength of a novel high-temperature solid oxide fuel cell sealing glass, J. Power Sources, 185 (2008) 1001-1008.

[96] M.J. Da Silva, J.F. Bartolome, A.H. De Aza, S. Mello-Castanho, Glass ceramic sealants belonging to BAS ($BaO-Al_2O_3-SiO_2$) ternary system modified with B_2O_3 addition: A different approach to access the SOFC seal issue, J. Eur. Ceram. Soc., 36 (2016) 631-644.

[97] N.P. Bansal, E.A. Gamble, Crystallization kinetics of a solid oxide fuel cell seal glass by differential thermal analysis, J. Power Sources, 147 (2005) 107-115.

[98] L. Blum, Q.P. Fang, S.M. Gross-Barsnick, L.G.J. de Haart, J. Malzbender, N.H. Menzler, W.J. Quadakkers, Long-term operation of solid oxide fuel cells and preliminary findings on accelerated testing, Int. J. Hydrog. Energy, 45 (2020) 8955-8964.

[99] R.N. Singh, Sealing technology for solid oxide fuel cells (SOFC), Int. J. Appl. Ceram. Technol., 4 (2007) 134-144.

[100] S. Gross, J. Malzbender, Q. Fang, Repair Joining of Glass-Ceramic Sealants for SOC Stacks, ECS Transactions, 103 (2021) 1859-1865.

[101] L. Peng, Q.S. Zhu, Thermal cycle stability of $BaO-B_2O_3-SiO_2$ sealing glass, J. Power Sources, 194 (2009) 880-885.

[102] T. Zhang, D.A. Tang, H.W. Yang, Can crystalline phases be self-healing sealants for solid oxide fuel cells?, J. Power Sources, 196 (2011) 1321-1323.

[103] D. Faidel, W. Behrl, S. Gross, U. Reisgen, Glass sealing materials and laser joining process development for fuel cell stack manufacturing, Materialwiss. Werkstofftech., 41 (2010) 914-924.

[104] D. Faidel, W. Behr, S.-M. Groß-barsnick, G. Natour, U. Reisgen, Laser-Supported Glass Sealant Repair Process For Untight Solid Oxide Fuel Cell Stacks, (2013).

[105] S. Rodriguez-Lopez, R. Comesana, J. del Val, A. Duran, V.M. Justo, F.C. Serbena, M.J. Pascual, Laser cladding of glass-ceramic sealants for SOFC, J. Eur. Ceram. Soc., 35 (2015) 4475-4484.

[106] D. Faidel, W. Behr, S. Gross, U. Reisgen, Development of a laser-based glass sealing joining process for the fuel cell manufacturing, 6th International Conference on Laser Assisted Net Shape EngineeringErlangen, GERMANY, 2010, pp. 153-162.

[107] D. Faidel, W. Behr, S.-M. Groß-barsnick, G. Natour, U. Reisgen, Laser-Supported Glass Sealant Repair Process For Untight Solid Oxide Fuel Cell Stacks, 2013.

[108] Z. Yang, J.W. Stevenson, K.D. Meinhardt, Chemical interactions of barium–calcium–aluminosilicate-based sealing glasses with oxidation resistant alloys, Solid State Ion., 160 (2003) 213-225.

[109] T.K. Sonja M. Gross, Josef Remmel, Jean-Bernard Bouche and Uwe Reisgen, Joining properties of a composite glass-ceramic sealant, Fuel Cells Bulletin, 2006 (2006) 12-15.

[110] E. Wanko, Entwicklung eines neuen Konzepts zur Steuerung der thermischen Ausdehnung von glaskeramischen Verbundwerkstoffen mit angepasster Fliessfähigkeit am Beispiel der Hochtemperatur-Brennstoffzelle, Forschungszentrum, Zentralbibliothek, Jülich, 2011.

[111] M. Heidenreich, C. Kaps, A. Simon, F. Schulze-Kuppers, S. Baumann, Expansion behaviour of (Gd, Pr)-substituted CeO_2 in dependence on temperature and oxygen partial pressure, Solid State Ion., 283 (2015) 56-67.

[112] A. Hruby, Evaluation of glass-forming tendency by means of DTA, Czechoslovak Journal of Physics Section B, B 22 (1972) 1187-1993.

[113] A. Hrubý, L. Štourač, Glassy semiconducting As2Te3, Materials Research Bulletin, 6 (1971) 465-468.

[114] T. Sochi, High Throughput Software for Powder Diffraction and its Application to Heterogeneous Catalysis, arXiv: Data Analysis, Statistics and Probability, (2010).

[115] C.W. Bale, E. Belisle, P. Chartrand, S.A. Decterov, G. Eriksson, K. Hack, I.H. Jung, Y.B. Kang, J. Melancon, A.D. Pelton, C. Robelin, S. Petersen, FactSage thermochemical software and databases - recent developments, Calphad-Computer Coupling of Phase Diagrams and Thermochemistry, 33 (2009) 295-311.

[116] C.W. Bale, E. Belisle, P. Chartrand, S.A. Decterov, G. Eriksson, A.E. Gheribi, K. Hack, I.H. Jung, Y.B. Kang, J. Melancon, A.D. Pelton, S. Petersen, C. Robelin, J. Sangster, P. Spencer, M.A. Van Ende, FactSage thermochemical software and databases, 2010-2016, Calphad-Computer Coupling of Phase Diagrams and Thermochemistry, 54 (2016) 35-53.

[117] G.S. Back, H.S. Park, S.M. Seo, W.G. Jung, Exploring high-strength glass-ceramic materials for upcycling of industrial wastes, Met. Mater.-Int., 21 (2015) 1061-1067.

[118] L.F. Sun, J.J. Shi, Effect of Al_2O_3 Addition on the Phase Equilibria Relations of $CaO-SiO_2$-5 wt%$MgO-Al_2O_3-TiO_2$ System Relevant to Ti-bearing Blast Furnace Slag, Isij International, 59 (2019) 1184-1191.

[119] Z.J. Shen, R.X. Li, Q.F. Liang, J.L. Xu, H.F. Liu, Effect of Cooling Process on the Generation and Growth of Crystals in Coal Slag, Energy Fuels, 30 (2016) 5167-5173.

[120] W.M. Groenewoud, CHAPTER 3 - THERMODILATOMETRY, in: W.M. Groenewoud (Ed.) Characterisation of Polymers by Thermal Analysis, Elsevier Science B.V., Amsterdam, 2001, pp. 77-93.

[121] D.G. Frank Caspar, Thomas Koppitz, Verfahren und Vorrichtung zur Messung der eindimensionalen Wärmeausdehnung bzw.-schrumpfung einer Probe unter Druckbelastung, Deutschland, 2001.

[122] U.D. P.Batfalsky, T. Koppitz, Flowing and settling behaviour of high-temperature glass-ceramic brazes under joining conditions, Brazing, High Temperature Brazing and Diffusion Welding the 5th International Conference, DVS, Aachen, Germany, 1998, pp. 97-99.

[123] T. Osipova, J. Wei, G. Pećanac, J. Malzbender, Room and elevated temperature shear strength of sealants for solid oxide fuel cells, Ceram. Int., 42 (2016) 12932-12936.

[124] J. Wei, Mechanical characterization of solid oxide fuel cells and sealants, Forschungszentrum, Zentralbibliothek, Jülich, 2017.

[125] M.F. Hasanabadi, A.H. Kokabi, M.A. Faghihi-Sani, S.M. Gross-Barsnick, J. Malzbender, Room- and high-temperature torsional shear strength of solid oxide fuel/electrolysis cell sealing material, Ceram. Int., 45 (2019) 2219-2225.

[126] F.P. Ghaleb Natour, Analysis of materials and structures in scientific applications using micro focus computed tomography, Key Engineering Materials, Vol. 613 (2014) 239-243.

[127] M. Vellini, M. Gambini, CO_2 capture in advanced power plants fed by coal and equipped with OTM, Int. J. Greenh. Gas Control, 36 (2015) 144-152.

[128] Y. Liu, V. Motalov, S. Baumann, D. Sergeev, M. Muller, Y.J. Sohn, O. Guillon, Thermochemical stability of Fe- and co-functionalized perovskite-type $SrTiO_3$ oxygen transport membrane materials in syngas conditions, J. Eur. Ceram. Soc., 39 (2019) 4874-4881.

[129] V.V. Kharton, A.V. Kovalevsky, E.V. Tsipis, A.P. Viskup, E.N. Naumovich, J.R. Jurado, J.R. Frade, Mixed conductivity and stability of A-site-deficient $Sr(Fe,Ti)O_{3-\delta}$ perovskites, Journal of Solid State Electrochemistry, 7 (2002) 30-36.

[130] R.O. Silva, J. Malzbender, F. Schulze-Kuppers, S. Baumann, O. Guillon, Mechanical properties and lifetime predictions of dense $SrTi_{1-x}Fe_xO_{3-\delta}$ (x=0.25, 0.35, 0.5), J. Eur. Ceram. Soc., 37 (2017) 2629-2636.

[131] T. Zhang, Q. Zou, Tuning the thermal properties of borosilicate glass ceramic seals for solid oxide fuel cells, J. Eur. Ceram. Soc., 32 (2012) 4009-4013.

[132] S. Rodriguez-Lopez, J. Malzbender, V.M. Justo, F.C. Serbena, S.M. Gross-Barsnick, M.J. Pascual, Thermo-Mechanical Stability and Gas-Tightness of Glass-Ceramics Joints for SOFC in the System $MgO-BaO/SrO-B_2O_3-SiO_2$, Frontiers in Materials, 7 (2020).

[133] S.M. Gross-Barsnick, Q. Fang, P. Batfalsky, L. Niewolak, L. Blum, W.J. Quadakkers, Post-test Characterization of Metallic Materials and Adjacent Components in an SOFC Stack After 34,000 h Operation at 700 degrees C, Fuel Cells, 19 (2019) 84-95.

[134] A.A. Cabral, C. Fredericci, E.D. Zanotto, A test of the Hruby parameter to estimate glass-forming ability, J. Non-Cryst. Solids, 219 (1997) 182-186.

[135] T.V.R. Marques, A.A. Cabral, Influence of the heating rates on the correlation between glass-forming ability (GFA) and glass stability (GS) parameters, J. Non-Cryst. Solids, 390 (2014) 70-76.

[136] A.R. Kampf, R.C. Peterson, B.R. Joy, ITSIITE, $Ba_2Ca(BSi_2O_7)_2$, A NEW MINERAL SPECIES FROM YUKON, CANADA: DESCRIPTION AND CRYSTAL STRUCTURE, Can. Mineral., 52 (2014) 401-407.

[137] T. Zhang, Q. Zou, J. Zhang, D. Tang, H. Yang, Development of ceramic sealant for solid oxide fuel cell application: Self-healing property, mechanical stability and thermal stability, J. Power Sources, 204 (2012) 122-126.

[138] M. Kerstan, C. Rüssel, Barium silicates as high thermal expansion seals for solid oxide fuel cells studied by high-temperature X-ray diffraction (HT-XRD), J. Power Sources, 196 (2011) 7578-7584.

[139] M. Kerstan, M. Muller, C. Russel, High temperature thermal expansion of $BaAl_2Si_2O_8$, $CaAl_2Si_2O_8$, and $Ca_2Al_2SiO_7$ studied by high-temperature X-ray diffraction (HT-XRD), Solid State Sci., 38 (2014) 119-123.

[140] M. Kerstan, M. Muller, C. Russel, Thermal expansion of $Ba_2ZnSi_2O_7$, $BaZnSiO_4$ and the solid solution series $BaZn_{2-x}Mg_xSi_2O_7$ ($0 <= x <= 2$) studied by high-temperature X-ray diffraction and dilatometry, J. Solid State Chem., 188 (2012) 84-91.

[141] S.P. Srivastava, R.C. Srivastava, I.D. Singh, S.D. Pandey, P.L. Gupta, TEMPERATURE-DEPENDENCE OF THERMAL-EXPANSION AND IR LATTICE VIBRATIONAL MODE OF NICKEL-OXIDE, J. Phys. Soc. Jpn., 43 (1977) 885-890.

[142] X.L. Pang, K.W. Gao, H.S. Yang, L.J. Qiao, Y.B. Wang, A.A. Volinsky, Interfacial microstructure of chromium oxide coatings, Adv. Eng. Mater., 9 (2007) 594-599.

[143] K. Eichler, G. Solow, P. Otschik, W. Schaffrath, BAS ($BaO·Al_2O_3·SiO_2$)-glasses for high temperature applications, J. Eur. Ceram. Soc., 19 (1999) 1101-1104.

[144] I.W. Donald, PREPARATION, PROPERTIES AND CHEMISTRY OF GLASS-CERAMIC-TO-METAL AND GLASS-CERAMIC-TO-METAL SEALS AND COATINGS, J. Mater. Sci., 28 (1993) 2841-2886.

[145] M.J. Bennett, R. Newton, J.R. Nicholls, H. Al-Badairy, G.J. Tatlock, p. trans tech, The oxidation behaviour of the commercial FeCrAIRE alloys aluchrom YHf and kanthal AF foils in air at 800 °-950 °C, in: P. Steinmetz, I.G. Wright, G. Meier, A. Galerie, B. Pieraggi, R. Podor (Eds.) High Temperature Corrosion and Protection of Materials 6, Prt 1 and 2, Proceedings2004, pp. 463-472.

[146] G. Strehl, D. Naumenko, H. Al-Badairy, L.M.R. Lobo, G. Borchardt, G.J. Tatlock, W.J. Quadakkers, The effect of aluminium depletion on the oxidation behaviour of FeCrAl foils, Mater. High Temp., 17 (2000) 87-92.

[147] V. Bongiorno, R. Spotorno, D. Paravidino, P. Piccardo, On the High-Temperature Oxidation and Area Specific Resistance of New Commercial Ferritic Stainless Steels, Metals, 11 (2021).

[148] B.C. Greven, S.M. Gross-Barsnick, D. Federmann, R. Conradt, Strength Evaluation of Multilayer Glass-Ceramic Sealants, Fuel Cells, 13 (2013) 565-571.

[149] A.A. Reddy, D.U. Tulyaganov, M.J. Pascual, V.V. Kharton, E.V. Tsipis, V.A. Kolotygin, J.M.F. Ferreira, SrO-Containing Diopside Glass-Ceramic Sealants for Solid Oxide Fuel Cells: Mechanical Reliability and Thermal Shock Resistance, Fuel Cells, 13 (2013) 689-694.

[150] K. Raju, Muksin, S. Kim, K.S. Song, J.H. Yu, D.H. Yoon, Joining of metal-ceramic using reactive air brazing for oxygen transport membrane applications, Mater. Des., 109 (2016) 233-241.

[151] S. Sakuragi, Y. Funahashi, T. Suzuki, Y. Fujishiro, M. Awano, Non-alkaline glass-MgO composites for SOFC sealant, J. Power Sources, 185 (2008) 1311-1314.

[152] C. Lara, M.J. Pascual, A. Durán, Glass-forming ability, sinterability and thermal properties in the systems RO–BaO–SiO$_2$ (R=Mg, Zn), J. Non-Cryst. Solids, 348 (2004) 149-155.

[153] L. Rezazadeh, S. Baghshahi, A.N. Golikand, Z. Hamnabard, Structure, phase formation, and wetting behavior of BaO-SiO$_2$-B$_2$O$_3$ based glass-ceramics as sealants for solid oxide fuel cells, Ionics, 20 (2014) 55-64.

[154] E.A. Kim, H.W. Choi, Y.S. Yang, Effects of Al$_2$O$_3$ on (1-x) SrO-SiO$_2$-B$_2$O$_3$ -xAl$_2$O$_3$ glass sealant for intermediate temperature solid oxide fuel cell, Ceram. Int., 41 (2015) 14621-14626.

[155] K.S. Weil, J.E. Deibler, J.S. Hardy, D.S. Kim, G.G. Xia, L.A. Chick, C.A. Coyle, Rupture testing as a tool for developing planar solid oxide fuel cell seals, Journal of Materials Engineering and Performance, 13 (2004) 316-326.

[156] S.Y. Kim, J. Park, S.H. Kim, L. Kadathala, J.H. Baek, J.H. Kim, J.H. Choi, The Tuning Capability of CuO and Na$_2$CO$_3$ Dopant on Physical Properties for Laser Sealing Using Fiber Types of Sealant, Applied Sciences-Basel, 10 (2020).

[157] T.J. Rockett, W.R. Foster, The Thermal Stability of Purified Tridymite, American Mineralogist, 52 (1967) 1233-1240.

[158] X.Y. Liu, Y.P. Pu, P.K. Wang, Z.J. Dong, Z.X. Sun, Y. Hu, Morphological evolution of tridymite crystal in SrO-BaO-Nb$_2$O$_5$-CaO-SiO$_2$-B$_2$O$_3$ ferroelectric glass-ceramic, Mater. Lett., 128 (2014) 263-266.

[159] M. Sellami, M. Barre, M. Toumi, Synthesis, thermal properties and electrical conductivity of phosphoric acid-based geopolymer with metakaolin, Applied Clay Science, 180 (2019) 105192.

[160] J.A. Kosinski, J.G. Gualtieri, A. Ballato, Ieee, THERMAL-EXPANSION OF ALPHA-QUARTZ, 45th Annual Symp on Frequency ControlLos Angeles, Ca, 1991, pp. 22-28.

[161] J.B. Austin, THE COEFFICIENT OF LINEAR THERMAL EXPANSION OF TRIDYMITE, Journal of the American Chemical Society, 76 (1954) 6019-6020.

[162] E.O. Filatova, Y.V. Egorova, K.A. Galdina, T. Scherb, G. Schumacher, H.J.M. Bouwmeester, S. Baumann, Effect of Fe content on atomic and electronic structure of complex oxides Sr(Ti,Fe)O$_{3-\delta}$, Solid State Ion., 308 (2017) 27-33.

[163] G. Demazeau, B. Buffat, M. Pouchard, P. Hagenmuller, RECENT DEVELOPMENTS IN THE FIELD OF HIGH OXIDATION-STATES OF TRANSITION-ELEMENTS IN OXIDES STABILIZATION OF 6-COORDINATED IRON(V), Zeitschrift Fur Anorganische Und Allgemeine Chemie, 491 (1982) 60-66.

[164] J.M. Lee, G.M. Choi, Oxygen-permeating zirconia membrane: The effect of thickness and surface coating, J. Eur. Ceram. Soc., 27 (2007) 4219-4222.

[165] K.L. Scholl, E.A. Fletcher, Y_2O_3-doped ZrO_2 membranes for solar electrothermal and solarthermal separations .2. electron-hole conductivity of yttria-stabilized zirconia, Energy, 18 (1993) 69-74.

[166] A.Q. Pham, T.H. Lee, R.S. Glass, Oxygen permeation through short-circuited yttria-stabilized-zirconia membranes, Solid-State Ionic Devices Symposium at the 195th Electrochemical-Society MeetingSeattle, Wa, 1999, pp. 172-180.

[167] S.G. Lia, W.Q. Jin, N.P. Xu, J. Shi, Mechanical strength, and oxygen and electronic transport properties of $SrCo_{0.4}Fe_{0.6}O_{3-\delta}$ -YSZ membranes, Journal of Membrane Science, 186 (2001) 195-204.

List of abbreviations and symbols

OTM	Oxygen transport membrane
CTE (α)	Thermal expansion coefficient [$\times 10^{-6}$ K^{-1}]
STF25	$SrTi_{0.75}Fe_{0.25}O_{3-\delta}$
BS	Ba-Sr-Si-B system glass
H	Ba-Ca-Si-B system glass
CT	X-ray computed tomography
DSC	Differential scanning calorimetry
TG	Thermogravimetry
HSM	Hot stage microscopy
ICP-OES	Inductively coupled plasma emission spectroscopy
SEM	Scanning electron microscopy
EDS	Energy dispersive spectoscopy
XRD	X-ray diffraction
CCD	Charge-coupled device
WDS	Wavelength-dispersive X-ray spectroscopy
APT	Atom probe tomography
RAB	Reactive air brazing
YSZ	Yttrium-stabilized zirconia
SOFC	Solid oxide fuel cell
T_g	Glass transition temperature
T_r	Glass onset crystallization temperature
T_p	Crystallization peak temperature
T_m	Onset melting temperature
T_{mp}	Endothermic melting peak temperature
T_a	Onset shrinking temperature
T_b	End shrinking temperature
T_{FS}	First shrinkage temperature
T_{MS}	Maximum shrinkage temperature
T_D	Deformation temperature
T_S	Sphere temperature

T_{HB}	Half ball temperature
T_F	Flow temperature
A_{MS}/A_0	The highest area shrinkage rate at the maximum shrinkage point
ZEA-1	Central Institute of Engineering, Electronics and Analytics – and Engineering and Technology, Jülich Forschungszentrum
IEK-1	Institute of Energy and Climate Research – Materials Synthesis and Processing, Jülich Forschungszentrum
IEK-2	Institute of Energy and Climate Research, Microstructure and Properties of Materials, Jülich Forschungszentrum
η	Viscosity [dPa·s]
τ	Shear strength [N/m^2, MPa]

Index of Figures

Index of Tables

Acknowledgments

My special acknowledgements would also give my parents, my sisters and my brother for understanding and supporting my study abroad. I literally owe you everything. I love all of you. Finally, the financial support by China Scholarship Council (CSC) is highly acknowledged.

Publications and conference contribution

(1) Li, X.; Groß-Barsnick, S. M.; Koppitz, T.; Baumann, S.; Meulenberg, W. A.; Natour, G., Sealing behaviour of glass-based composites for oxygen transport membranes. *J. Eur. Ceram. Soc.* 2022**,** 42 (6), 2879-2891.

(2) Li, X., Groß-Barsnick, S.M., Baumann, S., Koppitz, T., Meulenberg, W.A. and Natour, G., Thermal properties and joinability investigation of $BaO–SrO–SiO_2–B_2O_3$ glasses for oxygen transport membrane application. Adv. Eng. Mater. 2022, 202200660.

(3) Oral presentation, Joining behavior of glass composite sealant for oxygen transport membrane application at LÖT 2022 – 13th International Conference on Brazing, High Temperature Brazing and Diffusion Bonding, Aachen, Germany

Proceeding paper: Xinfang Li, Sonja M. Groß-Barsnick, Thomas Koppitz, Ghaleb Natour, Joining behavior of glass composite sealant for oxygen transport membrane application, LÖT 2022 – 13th International Conference on Brazing, High Temperature Brazing and Diffusion Bonding, ISBN: 978-3-96144-182-2

Band / Volume 587
**Effects of salt precipitation during evaporation on porosity
and permeability of porous media**
J. Piotrowski (2022), xxvii, 139 pp
ISBN: 978-3-95806-650-2

Band / Volume 588
**IEK-14 Report 2022
Forschung für die Energiewende und den Wandel im Rheinischen Revier**
B. Emonts (Hrsg.) (2022)
ISBN: 978-3-95806-652-6

Band / Volume 589
Oxidation of monoterpenes studied in atmospheric simulation chambers
L. L. Hantschke (2022), 188 pp
ISBN: 978-3-95806-653-3

Band / Volume 590
**NiFe Layered Double Hydroxide Catalysts for Oxygen Evolution Reaction
in Alkaline Water Electrolysis**
W. Jiang (2022), 165 pp
ISBN: 978-3-95806-658-8

Band / Volume 591
Optimizing Cross-linked Infrastructure for Future Energy Systems
L. Welder (2022), xxiii, 360 pp
ISBN: 978-3-95806-659-5

Band / Volume 592
**Evaluation von Reaktorkonzepten für die CO_2-basierte Methanolsynthese
aus Wasserstoff und Kohlendioxid mithilfe von CFD-Simulationen**
S. Weiske (2022), x, 369 pp
ISBN: 978-3-95806-661-8

Band / Volume 593
Spectral Induced Polarization of Biochar in Soil
Z. Gao (2022), XXVI, 155 pp
ISBN: 978-3-95806-662-5

Band / Volume 594
**Eignung von nickelhaltigen Katalysatorsystemen in sauren Medien zur
Nutzung im Betrieb von Brennstoffzellen**
A. Karaca (2022), iv, 249 pp
ISBN: 978-3-95806-663-2

Schriften des Forschungszentrums Jülich
Reihe Energie & Umwelt / Energy & Environment

Weitere *Schriften des Verlags im Forschungszentrum Jülich* unter
http://wwwzb1.fz-juelich.de/verlagextern1/index.asp

JÜLICH
Forschungszentrum